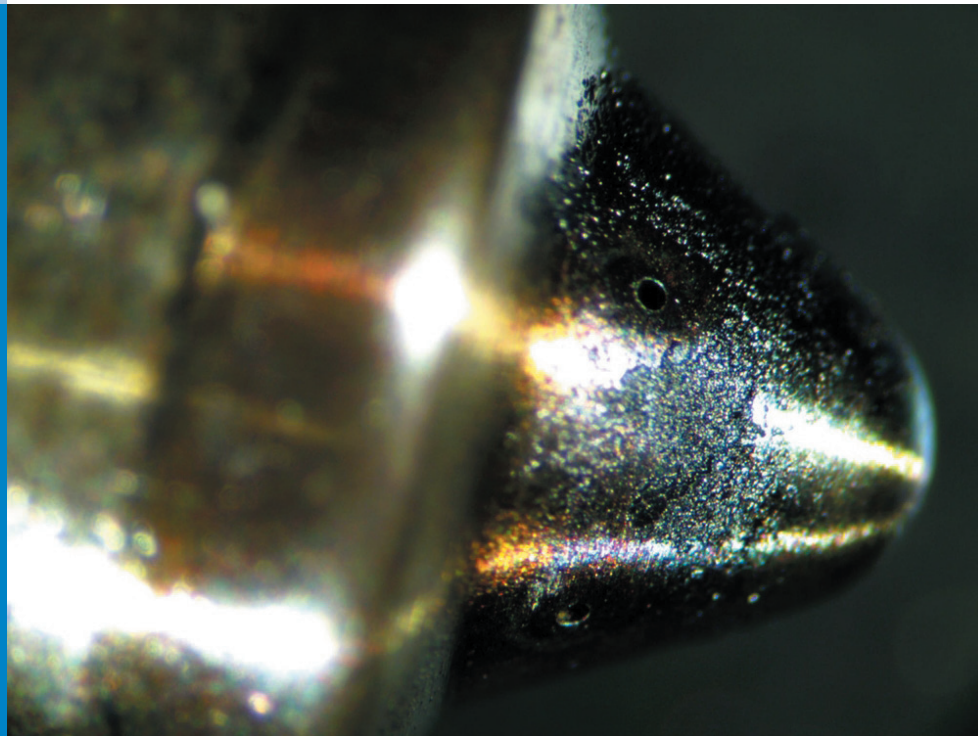




Strojniški vestnik

Journal of Mechanical Engineering



no. **2**
year **2015**
volume **61**

Strojniški vestnik – Journal of Mechanical Engineering (SV-JME)

Aim and Scope

The international journal publishes original and (mini)review articles covering the concepts of materials science, mechanics, kinematics, thermodynamics, energy and environment, mechatronics and robotics, fluid mechanics, tribology, cybernetics, industrial engineering and structural analysis.

The journal follows new trends and progress proven practice in the mechanical engineering and also in the closely related sciences as are electrical, civil and process engineering, medicine, microbiology, ecology, agriculture, transport systems, aviation, and others, thus creating a unique forum for interdisciplinary or multidisciplinary dialogue.

The international conferences selected papers are welcome for publishing as a special issue of SV-JME with invited co-editor(s).

Editor in Chief

Vincenc Butala

University of Ljubljana, Faculty of Mechanical Engineering, Slovenia

Technical Editor

Pika Škraba

University of Ljubljana, Faculty of Mechanical Engineering, Slovenia

Founding Editor

Bojan Kraut

University of Ljubljana, Faculty of Mechanical Engineering, Slovenia

Editorial Office

University of Ljubljana, Faculty of Mechanical Engineering
SV-JME, Aškerčeva 6, SI-1000 Ljubljana, Slovenia

Phone: 386 (0)1 4771 137

Fax: 386 (0)1 2518 567

info@sv-jme.eu, <http://www.sv-jme.eu>

Print: Grafex, d.o.o., printed in 380 copies

Founders and Publishers

University of Ljubljana, Faculty of Mechanical Engineering,
Slovenia

University of Maribor, Faculty of Mechanical Engineering,
Slovenia

Association of Mechanical Engineers of Slovenia
Chamber of Commerce and Industry of Slovenia,
Metal Processing Industry Association

President of Publishing Council

Branko Širok

University of Ljubljana, Faculty of Mechanical Engineering, Slovenia

Vice-President of Publishing Council

Jože Balič

University of Maribor, Faculty of Mechanical Engineering, Slovenia

International Editorial Board

Kamil Arslan, Karabuk University, Turkey

Josep M. Bergada, Politechnical University of Catalonia, Spain

Anton Bergant, Litostroj Power, Slovenia

Miha Boltežar, UL, Faculty of Mechanical Engineering, Slovenia

Franci Čuš, UM, Faculty of Mechanical Engineering, Slovenia

Anselmo Eduardo Diniz, State University of Campinas, Brazil

Igor Emri, UL, Faculty of Mechanical Engineering, Slovenia

Imre Felde, Obuda University, Faculty of Informatics, Hungary

Janez Grum, UL, Faculty of Mechanical Engineering, Slovenia

Imre Horvath, Delft University of Technology, The Netherlands

Aleš Hribernik, UM, Faculty of Mechanical Engineering, Slovenia

Soichi Ibaraki, Kyoto University, Department of Micro Eng., Japan

Julius Kaplunov, Brunel University, West London, UK

Iyas Khader, Fraunhofer Institute for Mechanics of Materials, Germany

Jernej Klemenc, UL, Faculty of Mechanical Engineering, Slovenia

Milan Kljajin, J.J. Strossmayer University of Osijek, Croatia

Janez Kušar, UL, Faculty of Mechanical Engineering, Slovenia

Gorazd Lojen, UM, Faculty of Mechanical Engineering, Slovenia

Thomas Lübben, University of Bremen, Germany

Janez Možina, UL, Faculty of Mechanical Engineering, Slovenia

George K. Nikas, KADMOS Engineering, UK

José L. Ocaña, Technical University of Madrid, Spain

Miroslav Plančak, University of Novi Sad, Serbia

Vladimir Popović, University of Belgrade, Faculty of Mech. Eng., Serbia

Franci Pušavec, UL, Faculty of Mechanical Engineering, Slovenia

Bernd Sauer, University of Kaiserslautern, Germany

Rudolph J. Scavuzzo, University of Akron, USA

Arkady Voloshin, Lehigh University, Bethlehem, USA

General information

Strojniški vestnik – Journal of Mechanical Engineering is published in 11 issues per year (July and August is a double issue).

Institutional prices include print & online access: institutional subscription price and foreign subscription €100,00 (the price of a single issue is €10,00); general public subscription and student subscription €50,00 (the price of a single issue is €5,00). Prices are exclusive of tax. Delivery is included in the price. The recipient is responsible for paying any import duties or taxes. Legal title passes to the customer on dispatch by our distributor.

Single issues from current and recent volumes are available at the current single-issue price. To order the journal, please complete the form on our website. For submissions, subscriptions and all other information please visit: <http://en.sv-jme.eu/>.

You can advertise on the inner and outer side of the back cover of the journal. The authors of the published papers are invited to send photos or pictures with short explanation for cover content.

We would like to thank the reviewers who have taken part in the peer-review process.

The journal is subsidized by Slovenian Research Agency.



Cover:

Corrosion is a factor significantly affecting the failure frequency of common rail systems. Destructive process can be concentrated locally to form a pit or crack, or it can extend across a wide area more or less uniformly corroding the surface. The consequences of its effect are accelerated wear of respective parts and assemblies, such as fuel injector nozzle tip and disc plate.

Courtesy:

The West Pomeranian University of Technology, The Department of Automotive Engineering, Poland

ISSN 0039-2480

© 2015 Strojniški vestnik - Journal of Mechanical Engineering. All rights reserved. SV-JME is indexed / abstracted in: SCI-Expanded, Compendex, Inspec, ProQuest-CSA, SCOPUS, TEMA. The list of the remaining bases, in which SV-JME is indexed, is available on the website.

Strojniški vestnik - Journal of Mechanical Engineering is available on <http://www.sv-jme.eu>, where you access also to papers' supplements, such as simulations, etc.

Contents

Strojniški vestnik - Journal of Mechanical Engineering
volume 61, (2015), number 2
Ljubljana, February 2015
ISSN 0039-2480

Published monthly

Papers

Karol Franciszek Abramek, Tomasz Stoeck, Tomasz Osipowicz: Statistical Evaluation of the Corrosive Wear of Fuel Injector Elements Used in Common Rail Systems	91
Liao Yunfei, Zhou Yi, Liu Youhai, Zuo Dong, Tan Bo: Study of Stability of Precise Tiled-grating Device	99
Diego E. Lozano, Gabriela Martinez-Cazares, Rafael D. Mercado-Solis, Rafael Colás, George E. Totten: Estimation of Transient Temperature Distribution during Quenching, via a Parabolic Model	107
Yi Jiangang: Modelling and Analysis of Step Response Test for Hydraulic Automatic Gauge Control	115
Serkan Balli, Faruk Sen: Failure Prediction of Cross-Ply Laminated Double-Serial Mechanically Fastened Composites using Fuzzy Expert System	123
Xiaoming Huang, Jie Sun, Jianfeng Li: Effect of Initial Residual Stress and Machining-Induced Residual Stress on the Deformation of Aluminium Alloy Plate	131
Sebastian Baloš, Mladimir Milutinović, Michal Potran, Jelena Vuletić, Tatjana Puškar, Tomaž Pepelnjak: The Mechanical Properties of Moulded and Thermoformed Denture Resins	138

Statistical Evaluation of the Corrosive Wear of Fuel Injector Elements Used in Common Rail Systems

Karol Franciszek Abramek – Tomasz Stoeck* – Tomasz Osipowicz

The West Pomeranian University of Technology, The Department of Automotive Engineering, Poland

This paper presents the causes and consequences of corrosion that has a destructive impact on the technical condition and operational reliability of Common Rail fuel injectors. The analysis included selected components indicating the elements and assemblies most frequently subject to destructive processes. Statistical evaluation of the corrosive wear of fuel injector elements was carried out based on experimental data obtained when verifying the fuel injector designs of different generations using the concept of corrosion density, related to our own classification of the degree of wear. The repair efficiency percentages were specified, taking into account specific operational mileages. Typical problems with the fuel injectors of leading manufacturers, with examples, are also shown.

Keywords: common rail fuel injectors, component corrosion, statistical evaluation

Highlights

- Nozzle bodies and control valve assemblies proved to be most prone to corrosion.
- The wear of electrical elements is least frequent.
- An increase in the injection pressure leads to intensification of corrosive wear.
- Repair is no longer effective with high operational mileages.
- Availability of spare parts has a fundamental impact on fuel injector repair.

0 INTRODUCTION

The process of wear can be defined as changes in the injection system as a result of use and leading to a gradual loss of functionality or permanent damage. Due to exceptionally difficult operating conditions, the elements of common rail systems being most prone to defects are fuel injectors [1]. Among other things, corrosion due to chemical or electrochemical mechanisms plays an important role in causing defects in fuel injection elements. Firstly, corrosion may affect sub-assemblies that have direct contact with the fuel and is found in the surface layers of friction pairs having different properties than the original material. Secondly, galvanic cells are formed which lead to reduction and oxidation reactions in the presence of electrolytes [2]. Accelerated wear may be defined as a situation in which the intensity of the formation of corrosion products (e.g. oxides, hydroxides) is higher than the surface destruction as a result of boundary friction.

The corrosive effects of diesel oil depends largely on acidic oxygen complexes of natural origin or on the ageing processes being taking place in the oil itself, as well as on the content of sulphur and water compounds. Thus, the quality and type of fuel that feeds an engine substantially affects the intensity of the processes being discussed. Recently, fatty acid methyl esters (FAME) have been popularised as biodiesels, mainly for ecological reasons. Many researchers

have shown, however, that fuels of this group are characterised by a high degree of oxidation [3], as well as a tendency to polymerisation [4] and deposit formation [5], and increased microbial degradation [6]. High hygroscopicity of FAMES, affecting water absorption from the surroundings and increasing corrosion aggressiveness, is also very important. In some papers [7] and [8], it has been pointed out that corrosive action on metals is increased by the presence of alcohol, glycerol and free fatty acids. However, not all of these compounds are post-production residues of esterification. For example, it has been shown that dehydrated ethanol, applied in mixtures with FAME or diesel oil to improve starting properties, may have a corroding effect on the fuel pump and injector elements and, additionally, induce seal swelling and stiffening [9] and [10].

A separate issue is light heating oils, which are used illegally to fuel engines of commercial vehicles and to which red dye is added in order to identify the use of such oil. According to Kowalski [11], the properties of light heating oils do not fundamentally depart from those of diesel oils and their use should not cause major problems from the operational point of view. However, it is noteworthy that procedures for dye removal require the application of sulphuric acid, which has an exceptionally aggressive effect on metals. Attempts to neutralise this acid lead to the development of small grains initiating accelerated abrasive wear on the injection system. It has been

*Corr. Author's Address: The West Pomeranian University of Technology, The Department of Automotive Engineering, Piastów 19 Ave., 70-310 Szczecin, Poland, tstoeck@wp.pl

emphasised in another paper [12] that one of the elementary mistakes being made by the users of agricultural vehicles is the use of such heating oil, which leads to damages in the respective assemblies of force pumps and defects in fuel injector sprayers.

Besides the quality and type of fuel, other factors having a significant impact on the intensity of corrosion occurrence are also noted in the reference literature. They include, among others, high temperature and pressure occurring in the combustion chamber [13], direct contact with fuel [14], ballistic phenomena [15], and turbulent fluid flow [16]. Researchers have also brought up the problems of accompanying processes, i.e. erosion [17] and cavitation [18]. Hence, a precision pair (needle and nozzle) affected by the phenomena mentioned above were examined. There are no data referring to other fuel injector elements and assemblies fulfilling executive and control functions. Our studies have shown that corrosion affects the parts of valve and armature assemblies almost equally.

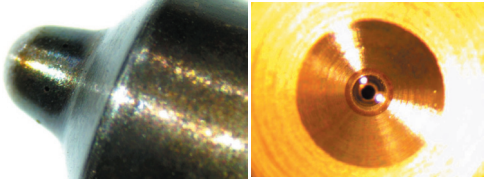
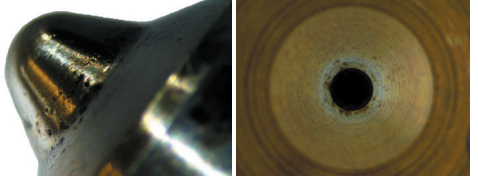
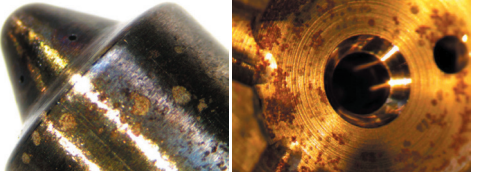
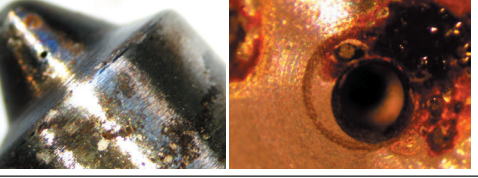
1 EXPERIMENTAL METHODS

The primary objective of this study was to statistically evaluate the corrosive wear of fuel injector elements of different types and manufacturers, taking into account the factors that have a negative effect on their operational reliability. In the analysis, the utilitarian nature of the repairs being conducted was also considered, and thus the possibility of eliminating the deficiencies being discussed, with a view to the degree of wear of respective parts and the possibility of their replacement.

1.1 Test Object

The test object was common rail fuel injectors. A total of 3200 from a number leading manufacturers of fuel injection equipment such as Bosch, Delphi, Denso and Siemens were tested. Examination and verification of respective fuel injector components were conducted at the laboratories of VASCO Co. Ltd in Mierzyn, which co-operates with the Department of Automotive Engineering of the West Pomeranian University of Technology in Szczecin. The following equipment, among others, was used in this process: test benches (EPS 200 Bosch, Diesel Bench CRU 2 Zapp, Diesel Tech DS2 Zapp), a microscope with a camera to record digital images (FL150/70), ultrasonic cleaners (Elma Elmasonic S 10 H, Carbon Tech Ultrasonic Bath S15/C2), vices and fuel injector disassembly and assembly kits and a torque wrench set.

Table 1. Graphical classification of corrosion and the criteria of adopted classification illustrated by examples (nozzle and valve seat)

Level	0
Evaluation	No corrosion
Classification criteria	No corrosion traces found
Examples	
Level	1
Evaluation	Low corrosion
Classification criteria	Corrosion covered up to 19% of the area of examined element
Examples	
Level	2
Evaluation	Moderate corrosion
Classification criteria	Corrosion covered 20 to 39% of the area of the examined element
Examples	
Level	3
Evaluation	High corrosion
Classification criteria	Corrosion covered over 40% of the area of the examined element (or was more localized nature but of high intensity)
Examples	

1.2 Scope and Criteria of Evaluation

An experimental study was conducted according to our own methods, which included three implementation stages. In the first stage, fuel injectors were disassembled into components that were subject to detailed visual inspection and verification. Evaluation of the corrosion level was performed using visual methods as well as under a high magnification

laboratory microscope. The next stage was initiated by cleaning in ultrasonic baths, excluding components sensitive to the effect of cleaning fluid, e.g. solenoid valves and injector bodies with embedded piezoelectric crystal stacks. The parts being qualified for replacement were also left out. After thorough drying and blowing off with compressed air, fuel injectors were assembled and then the test stage was conducted on test benches (last stage). Possible fuel delivery correction included only the designs for which unsatisfactory sampling results had been obtained.

In order to conduct statistical analysis, the following visual levels of corrosion evaluation were established: 0 no corrosion, 1 low corrosion, 2 moderate corrosion, and 3 high corrosion. Examples of the graphical representation of adopted corrosion classification and its criteria are presented in Table 1. These fuel injector elements, which were eliminated due to pitting corrosion, most often of a local nature but of high intensity, are an exception. Although the size of the area affected by the changes was small, it was classified as level 3 (Fig. 1).

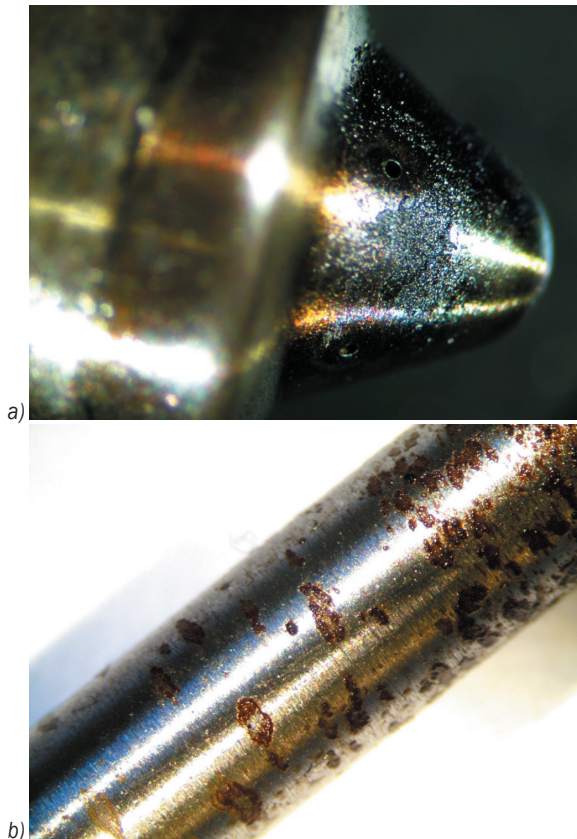


Fig. 1. Examples of pitting corrosion; a) Bosch fuel injector nozzle tip, and b) Denso needle

The results of the experiment were processed using the concept of corrosion density, the mathematical notation of which can be presented by the following equation [13]:

$$D_c = \frac{\sum_{i=1}^e L_i}{e}, \tag{1}$$

where D_c is corrosion density, L_i level of corrosion classification for the i th element and e is the number of elements.

For example, when examining Bosch fuel injectors, corrosion density was determined as an algebraic sum of the verified corrosion levels which referred to the total number of examined elements $e = 2368$:

$$D_{c(Bosch, neddes)} = \frac{(1+0+3+...)}{2368}. \tag{2}$$

2 RESULTS AND DISCUSSION

In Fig. 2 a histogram of the fuel injectors accepted for repair in VASCO over one year (11.2012-11.2013) is presented.

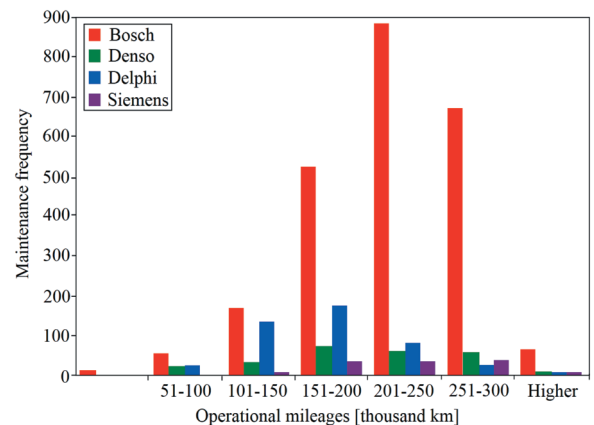


Fig. 2. Histogram of the fuel injectors accepted for repair in the test period

Fuel injectors by Bosch constituted nearly 75%, which results from the dominance of this manufacturer in the segment of the automotive market under consideration. However, it is worth noting that 2/3 of them were from vehicle engines with mileage over 201,000 km. A similar correlation occurred only in Siemens products but these were solely piezoelectric fuel injectors, the maintenance of which was limited to cleaning and tests on test benches. Results for other fuel injector manufacturers constitute unimodal distributions, being characterised by moderate left- or

right-sided asymmetry. In this respect, fuel injectors of the Delphi design performed least favourably, showing increased failure frequency after mileage of 101,000 km. On the other hand, few problems are observed in the first and the last sections of the diagram. This is due to the fact that new vehicles are covered by the manufacturer's guarantee, while the questions of possible failures are usually examined at a service station. At the other end, few fuel injectors with high operational mileages were accepted because the efficiency of their repair was low.

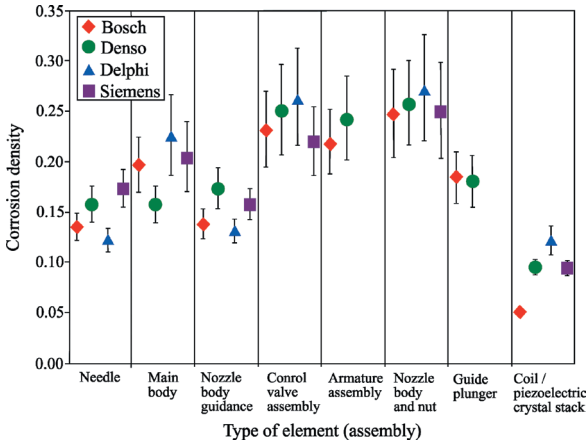


Fig. 3. Comparison of corrosion density for selected elements (assemblies) of the examined fuel injectors

Fuel injector nozzle bodies together with nuts and control valve assemblies proved to be the most prone to corrosion (Fig. 3). In the first case, a primary cause can be seen in the effect of high temperatures which induce accelerated degradation of the surface of metal, with an interaction of chemical and electrochemical reactions in the combustion chamber. However, it is worth noticing that corrosive processes affect the precision pair less, which has been confirmed by the results presented in paper [13]. For example, Delphi needles, being characterised by indents on the guide face made to preserve stable operation at higher pressures and under increased flow turbulence, performed most favourably in the given aspect. Corrosion mainly occurred in these depressions (Fig. 4a), while its traces were observed only in 42 elements from among 448 examined ones. Causes for increased failure frequency at relatively low mileages may be explained by the wear of fuel pumps, particularly of the drive areas of force assemblies, which generates metal fillings that get inside the fuel injector. The sharp edges of the needle indents induce jamming of hard impurities and accelerated seizing of the precision pair. Accelerated destruction of the control

assembly, which is also exposed to corrosion (first of all in the head seat and flange), erosion and cavitation processes, occurs similarly [17]. The solenoid coil, having frequent contact with fuel compared to that of other manufacturers, should also be mentioned. The seating of the element through almost the whole length of the body causes problems with O-ring seals, which may occur even with low operational mileages. Losses in material and corrosion were observed in the fuel injectors of the Ford Transit, Focus and Mondeo vehicle models.

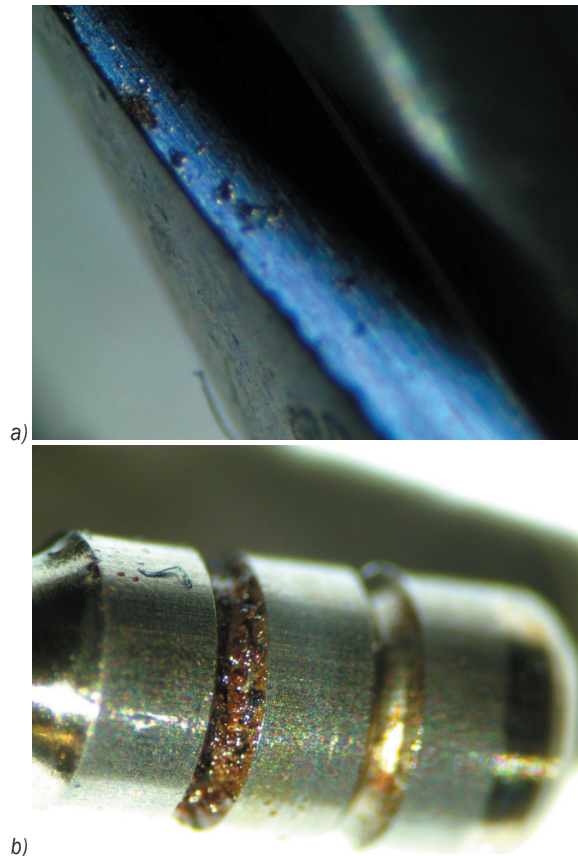


Fig. 4. Local corrosion of example parts of Delphi fuel injectors; a) needle and b) head

The verification being carried out showed that the wear of armature assembly found solely in the fuel injector designs of two manufacturers proceeds similarly to that of the valve arrangements. Changes are usually seen on the surface of the disc (much less often on that of the insert) and elements co-operating with it (Fig. 5). With a similar construction and principle of operation, a comparable value for the parameter under discussion was obtained, i.e.

$$D_{c(\text{Bosch, armature assembly})} = 0.22 \text{ and}$$

$$D_{c(\text{Denso, armature assembly})} = 0.24.$$



Fig. 5. Corrosion of Bosch fuel injector armature unit; a) disc plate and b) insert spring

From among all elements being affected by corrosion, nearly 58% were classified at level 1. As a result, it was possible to remove corrosion traces after half-hour baths in ultrasonic cleaners. This is extremely important in the case of Denso products because availability of respective parts from this manufacturer, e.g. armature springs, locking rings and calibration washers, etc., is limited.

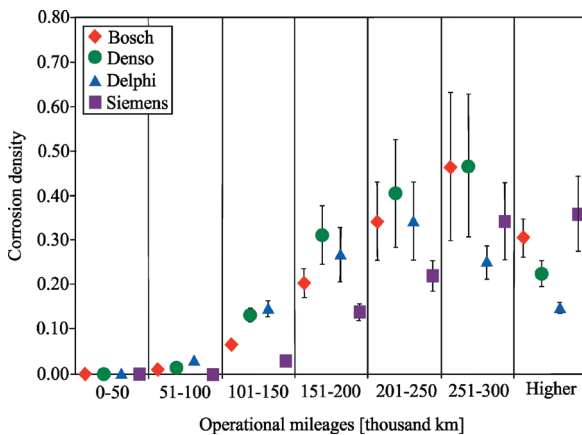


Fig. 6. Corrosion density according to operational mileages

Interesting results were obtained when comparing the corrosion density to operational mileages (Fig. 6). Over almost the whole range, the values of the corrosion density parameter show an upward tendency, which results from an increasing number of degraded elements being included at higher and higher levels of corrosion. A crucial change can be seen in the last interval. The trend here is disturbed due to a rapid decrease in the number of fuel injectors being accepted for repair because they are effectively irreparable. Nevertheless, the corrosion density there is definitely higher than with mileages of 0 to 150 thousand km. When analysing the presented data, one can conclude that the fuel injector designs using piezoelectric plate stacks by Siemens performed most favourably: wear traces on respective elements were observed less often and usually after a longer operation time. Unfortunately, both Siemens and Denso have a similar policy with respect to spare parts, i.e. there aren't any, which practically eliminates possibility of replacing these parts.

The statistics for the elements of Bosch fuel injectors looks completely different. Within the mileage range of 201 to 300 thousand km, nearly 65% of all fuel injector designs of this manufacturer were accepted for repair, obtaining as follows:

$$D_{c(Bosch, \text{ mileage: } 201 \text{ to } 150)} = 0.34 \text{ and}$$

$$D_{c(Bosch, \text{ mileage: } 251 \text{ to } 300)} = 0.47.$$

These results are, at best, comparable with the others (except the Siemens products) but the market of available parts allows repairs over almost the full range, with the technology of this process being developed in detail and provided as needed. Relatively low values of corrosion density for the Delphi elements, particularly with moderate and high mileages, are also noteworthy. This means that increased failure frequency for these fuel injector designs depends largely on other factors. In this respect, improper co-operation of the control assembly (valve head and housing) and the precision pair (needle and nozzle) was the most frequently detected defect, resulting from accelerated abrasive wear of the co-operating surfaces.

In recent years, a tendency has been observed to increase the injection pressure, which has a significant effect on the improvement of engine operational indicators and the reduction of emission of toxic exhaust gas components. Deterioration of operating conditions forced an increase in strength requirements which are being accomplished by changes in the design and materials. Results of our own study show that, despite these measures, the parts of injectors operating at higher pressures are more

prone to corrosive wear. Due to the sample size and availability of respective fuel injector generations, an analysis was conducted solely for products made by Bosch (Fig. 7). In successive intervals, a growing number of elements in the highest level of the adopted classification can be observed. A similar situation was obtained with corrosion density, except at a pressure area of 200 MPa, in which solenoid fuel injectors of the CRI 2.5 (*Common Rail Injector*) type had been only examined. Nevertheless, the number of 3rd level parts was three times larger when compared with the initial area where such generations as CRI 1.0, CRI 2.0 and additionally CRIN 1, i.e. the fuel injector designs being applied in engines of commercial vehicles (German: *Nutzfahrzeug*), were examined. A similar correlation is being found for the elements operating at a pressure of 160 to 180 MPa. The obtained results point to the necessity of a much broader use of materials, of which mainly fuel injector nozzles have been made so far, i.e. stellite, carbide-steel cermets. These are characterised by large dimensional stability at high temperatures but also by abrasion and corrosion resistance and resistance to the ataggressive effect of fuels [19].

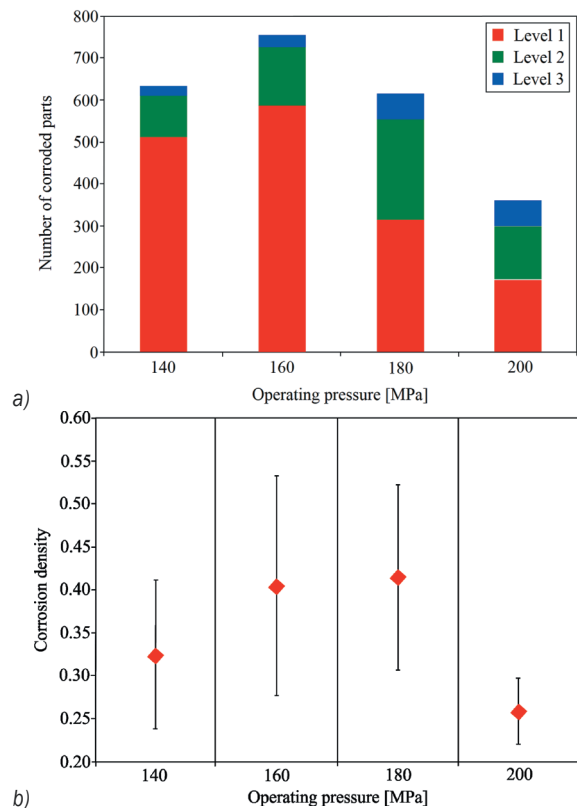


Fig. 7. Summary of results for Bosch fuel injectors working under different operating pressures; a) number of elements affected by corrosion and b) corrosion density

Table 2. Fuel injector repair efficiency in the testing period

Mileage	Number of repaired fuel injectors			
	Bosch	Denso	Delphi	Siemens
0-50	8	4	0	0
51-100	48	20	24	4
101-150	156	28	120	8
151-200	488	56	156	24
201-250	816	32	60	12
251-300	588	16	8	8
Higher	24	0	0	0
Summary	Total number of repaired fuel injectors			
	2128	156	368	56
Mileage	Repair efficiency index at specific mileage [%]			
	Bosch	Denso	Delphi	Siemens
0-50	100	100	100	100
51-100	92	100	100	100
101-150	93	88	91	100
151-200	93	74	89	75
201-250	92	53	71	33
251-300	88	29	33	22
Higher	37	0	0	0
Summary	Repair efficiency index for all manufacturer's designs [%]			
	90	61	82	44

The data presented in Table 2 suggest that repair is no longer effective at high operational mileages. In this respect, Bosch and Delphi fuel injectors, i.e. the designs of manufacturers offering the biggest product line of spare parts, performed most favourably. The fuel injectors being disqualified after main body defects (cracking, shape deformation, thread stripping) or defects in electrical elements (coil winding burnout, damages to piezoelectric crystal stack, breakage of terminal latches) had been found were an exception. The treatment was similar in the case of control solenoid valve corrosion. Attempts to remove corrosion traces using ultrasonic cleaners might result in undesirable softening of plastic housings and defects in insulation. Much lower repair efficiency indicators were obtained for fuel injectors from other manufacturers. In the case of Siemens, which specialises in piezoelectric fuel injectors, the maintenance essentially consisted of external and internal cleaning using only thermo-chemical methods and then to testing on test benches. Given the lack of availability of replacement parts by Siemens, the detection of more serious damages practically eliminated a given fuel injector. The repair of Denso products was possible over a slightly wider range. Some clients decided to use substitute parts that differ with respect to quality from the original elements, although they extend the service life of the fuel injectors. Replacement usually included the precision

pair (deformation of needle taper, contact zone overheating, external and internal corrosion, guide face scratching or seizure) as well as control valve assembly (seat erosive changes, stem scratching, body surface and valve seating corrosion).

3 CONCLUSIONS

The results of the above analysis show that corrosion is a factor significantly affecting the failure frequency of common rail systems. The consequences of its effect are accelerated wear of respective parts and assemblies, while products contaminate the interior of fuel injector and interfere with operating processes. The following conclusions have been drawn from this study:

1. The control valve and armature assemblies, which have direct contact with the fuel being supplied under high pressure, are equally affected by destructive processes of corrosion as nozzles.
2. The wear of electrical elements is least frequent but fuel injector is disqualified from further work (no cleaning or replacement possible).
3. As operational mileages continues to increase, corrosion density increases because corrosion traces are being observed in a larger number of parts, which are then classified as having higher and higher levels of wear.
4. An increase in the injection pressure leads to intensification of corrosive wear, despite design and material modifications in successive fuel injector generations.
5. Availability of spare parts has a fundamental impact on fuel injector repair efficiency because when they are missing (or limited) the elements or assemblies being affected by corrosion at higher levels cannot be replaced.
6. Limitation in the acceptance for repair of fuel injectors from engines with very high mileages results from their poor technical condition, most often precluding the recovery of nominal parameters.

4 NOMENCLATURE

CRI	common rail injector
CRIN	common rail injector (commercial vehicles)
D_c	corrosion density
e	number of elements
FAME	fatty acid methyl esters
L_i	level of corrosion classification for the i^{th} element

5 REFERENCES

- [1] Knefel, T. (2012). Technical assessment of Common Rail injectors on the ground of overflow bench tests. *Maintenance and Reliability*, vol. 14, no. 1, p. 42-53.
- [2] Perez, N. (2004). *Electrochemistry and Corrosion Science*, 1st ed. Kluwer Academic Publishers, Boston, DOI:10.1007/b118420.
- [3] Sharafutdinov, I., Stratiev, D., Shishkova, I., Dinkov, R., Batchvarov, A., Petkov, P., Rudnev, N. (2012). Cold flow properties and oxidation stability of blends of near zero sulfur diesel from Ural crude oil and FAME from different origin. *Fuel*, vol. 96, p. 556-567, DOI:10.1016/j.fuel.2011.12.062.
- [4] Shiwei, L., Lu, L., Shitao, Y., Congxia, X., Fusheng, L., Zhanqian, S. (2010). Polymerization of Fatty Acid Methyl Ester Using Acidic Ionic Liquid as Catalyst. *Chinese Journal of Catalysis*, vol. 31, no. 11-12, p. 1433-1438, DOI:10.1016/S1872-2067(10)60128-3.
- [5] Galle, J., Verhelst, S., Sierens, R., Goyos, L., Castaneda, R., Verhaege, M., Vervaeke, L., Bastiaen, M. (2012). Failure of fuel injectors in a medium speed diesel engine operating on bio-oil. *Biomass and Bioenergy*, vol. 40, p. 27-35, DOI:10.1016/j.biombioe.2012.01.041.
- [6] Schleicher, T., Werkmeister, R., Russ, W., Meyer-Pittroff, R. (2009). Microbiological stability of biodiesel - diesel - mixtures. *Bioresource Technology*, vol. 100, no. 2, p. 724-730, DOI:10.1016/j.biortech.2008.07.029.
- [7] Aquino, I.P., Hernandez, R.P.B., Chicoma, D.L., Pinto, H.P.F., Aoki, I.V. (2012). Influence of light, temperature and metallic ions on biodiesel degradation and corrosiveness to copper and brass. *Fuel*, vol. 102, p. 795-807, DOI:10.1016/j.fuel.2012.06.011.
- [8] Norouzi, S., Eslami, F., Wyszynski, M.L., Tsolakis, A. (2012). Corrosion effect of RME in blends with ULSD on aluminium and copper. *Fuel Processing Technology*, vol. 104, p. 204-210, DOI:10.1016/j.fuproc.2012.05.016.
- [9] Chauhan, B.S., Kumar, N., Pal, S.S., Jun, Y.D. (2011). Experimental studies on fumigation of ethanol in a small capacity diesel engine. *Energy*, vol. 36, no. 2, p. 1030-1038, DOI:10.1016/j.energy.2010.12.005.
- [10] Hansen, A.C., Zhang, Q., Lyne, P.W.L. (2005). Ethanol - diesel fuel blends - a review. *Bioresource Technology*, vol. 96, no. 2, p. 277-285, DOI:10.1016/j.biortech.2004.04.007.
- [11] Kowalski, K. (2006). Utilization of military vehicles under shortage of basic fuels. *Maintenance and Reliability*, vol. 4, p. 16-21.
- [12] Jósko, M., Kołodziejcki, M. (2008). Selected exploitation problems of agricultural vehicles in the scope of their servicing. *Journal of Research and Applications in Agricultural Engineering*, vol. 53, no. 2, p. 5-7.
- [13] Taflan, R.A., Karamangil, M.I. (2012). Statistical corrosion evaluation of nozzles used in diesel CRI systems. *Fuel*, vol. 102, p. 41-48, DOI:10.1016/j.fuel.2012.06.037.
- [14] Günther, H. (2012). *Common - Rail - Systeme in der Werkstattpraxis*. Technik, Prüfung, Diagnose, 4th ed., Kraftland Verlag Walter Schultz GmbH, Bad Wörlhofen.
- [15] Postrioti, L., Malaguti, S., Bosi, M., Buitoni, G., Piccinini, S., Bagli, G. (2014). Experimental and numerical characterization

- of a direct solenoid actuation injector for Diesel engine applications. *Fuel*, vol. 118, p. 316-328, **DOI:10.1016/j.fuel.2013.11.001**.
- [16] Boudy, F., Seers, P. (2009). Impact of physical properties of biodiesel on the injection process in a common-rail direct injection system. *Energy Conversion and Management*, vol. 50, no. 12, p. 2905-2912, **DOI:10.1016/j.enconman.2009.07.005**.
- [17] Olszowski, S. (2010). Examination of permeating oil causes in new generation diesel engines. *Transcomp - XIV international conference, Computer systems aide science, industry and transport*, vol. 6, p. 2581-2588.
- [18] Payri, F., Bermu´dez, V., Payri, R., Salvador, F.J. (2004). The influence of cavitation on the internal flow and the spray characteristics in diesel injection nozzles. *Fuel*, vol. 83, no. 4-5, p. 419-431, **DOI:10.1016/j.fuel.2003.09.010**.
- [19] Idzior, M. (2006). Tendencias of the construction changes in self-ignition engines injectors. *Motrol - Motorization and Power Industry in Agriculture*, vol. 8, p. 81-91.

Study of Stability of Precise Tiled-grating Device

Liao Yunfei – Zhou Yi* – Liu Youhai – Zuo Dong – Tan Bo
College of Mechanical Engineering, Chongqing University, China

To satisfy the high-stability requirement of a tiled grating, we have analyzed and optimized the stability of a newly designed precise tiled-grating device considering three aspects: structure design, transmission chain, and control algorithms. The main structure of the device is changed from a parallel-board structure to a new tetrahedral brace design, enhancing the overall vibration stability; during the analysis of the transmission chain, the adjustment accuracy and stability of the device were ensured by slowing the growth of the error transmission factor; and for the optimization analysis of the PID control algorithms, we adopted a latch compensation method to avoid the saturated loss and a four-point central difference method to avoid the disturbances, thus enhancing the stability control of the device. To test the stability of the device, an optical experiment with a reference spot was designed. The experimental results showed that over 380 s, the ambient excitation response was always within an acceptable range. The average deflections about the X axis and Y axis are 0.243 and 0.00146 μm , respectively, which satisfy the stability requirement.

Keywords: tiled-grating compressor, stability, dynamic response, tetrahedral, transmission chain, control algorithms

Highlights

- Showed a novel precise tiled-grating device.
- Compared the vibration stability of two types of tiled-grating device.
- Upgraded the transmission chain to decreased the error transmission factors.
- Improved the incremental PID algorithm.

0 INTRODUCTION

Chirped-pulse amplification (CPA) is an important technique for realizing amplification of ultra-short pulse lasers [1]. However, damage thresholds and the aperture of the compressor inside the CPA system limit the energy of the output laser pulse [2] and [3]. Currently, the grating with the best performance is the multilayer dielectric (MLD) diffraction grating, but it is very difficult to fabricate such gratings with sizes on the meter scale. Thus, most researchers around the world have adopted tiled gratings to obtain large gratings so as to enhance the energy of pulses output by lasers [4] and [5]. Because the quality of the laser beam depends upon stable tiled gratings as a key component [6], stability research on precise tiled gratings is important.

In 2009, Zhong-xi et al. [7] devised a macro-micro dual-drive parallel mechanism with a few degrees of freedom for a tiled-grating device, and provided an error-correction method and control algorithms. In 2011, Zhou et al. [8] designed a tiled-grating structure with a large aperture and high precision in the form of a 2×2 array; the design is based on modularization and a frame-style structure to ensure the stability of the device. The experiment showed that the device can adjust rapidly in a timely manner and also that the stability time is greater than one hour. In 2011, Junwei et al. [9] suggested using a material with a high degree

of damping to improve the connection status of the motion junction surface of the frame so as to lessen the dynamic response of the tiled brace and enhance the stability time. Here we describe and analyze a tiled-grating brace that is based on a newly designed tetrahedral structure and is designed to further enhance the stability of the tiled grating.

To further improve the stability of the tiled grating, a novel tiling-grating device has been developed. A tetrahedral brace is used as the main body of the device to increase the natural mechanical frequency of the device. Additionally, a virtual tripod is built to fix the grating in place, and the transmission chain is improved to reduce the influence of transmission errors. In terms of the control techniques, because the four-point central difference method and latch compensation method have been used to improve the PID algorithm of the actuator, the short-term fluctuations in the control variable are smoothed out, and the influence of environmental disturbances is reduced.

1 TILED-GRATING SYSTEM

This tiled grating consists of two sub-gratings, one of which is fixed and called the reference grating, and the other of which is an adjustable grating. The adjustable grating must take into account three degrees of freedom associated with the grating coordinates (x ,

y, z): the tilt (θ_y), tip (θ_x), and longitudinal piston (d_z) (Fig. 1).

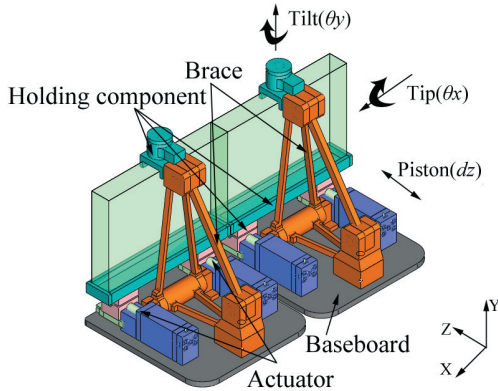


Fig. 1. Tiled-grating frame structure

The stabilization of a precise tiled grating relies on the structural stability of the vibration resistance of the device itself, the transmission precision and control stability of the device, and the ability of the control mechanism to compensate for environmental disturbances (Fig. 2). Therefore, we designed a tiled-grating device based on a tetrahedral structure; the tetrahedral structure enhanced the vibration stability of the device. We adopted an optimized transmission chain to increase the transmission precision and decrease the effect of errors; we also improved the control algorithm driving the actuator. As shown in Fig. 1, the device mainly consists of three parts: an adjusting component with three degrees of freedom, a grating brace, and a mount to hold the grating. Three piezoelectric actuators were used to adjust the three degrees of freedom.

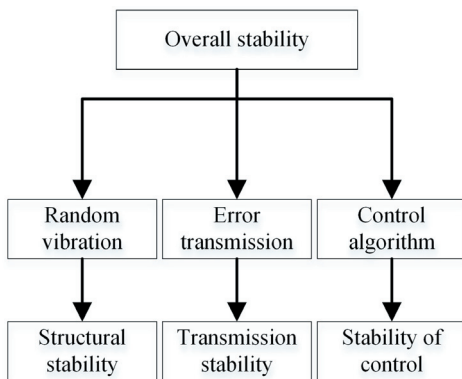


Fig. 2. Schematic of the stability-control mechanism for the tiled-grating device

2 STABILITY ANALYSIS OF TILED-GRATING DEVICE

2.1 Vibration Stability of Tiled-Grating Device

The mount that holds the whole precision tiled-grating device is composed of a baseboard and a tetrahedral brace. We modified the 2×2 parallel-board structure holding component of the tiled-grating brace to form a 2×1 brace. The finite-element random vibration analysis and Lanczos modal analysis of both of the tiled-grating frames are carried out using ANSYS software. In these analyses, the grating is defined to be formed from C9 glass; the other elements are defined to be formed from structural steel, and the bottom of the grating is assumed to be fixed. The analyses show that the vibrations of these points (marked by the points with teal labels in Fig. 3 along the top edge of each grating) have amplitudes that are as large as 5.2 and 9.1 μm , respectively. Both of these amplitudes are less than 12.9 μm ; therefore, the two devices meet the requirement given in [10]. Additionally, the tetrahedral mount has an important characteristic: the tetrahedral brace is a trussed structure; it helps in effectively decreasing the weight and enhancing the natural frequency of the structure. As shown in Table 1, the Phase 1 natural frequency of the tetrahedral brace was improved to 393.62 Hz; such a Phase 1 natural frequency can effectively avoid the risk of resonance.

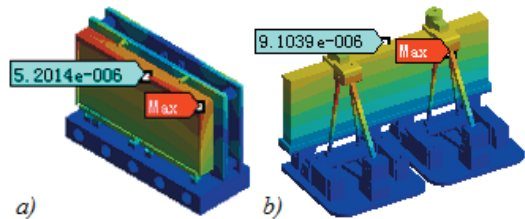


Fig. 3. Result of simulating the random vibration of two tiled-grating device designs; a) the parallel-board structure and b) the tetrahedral-brace structure

Table 1. Natural frequency of two different tiled-grating frames

Modes	1	2	3	4	5	6
Parallel board	124.25	224.01	372.73	407.85	516.82	570.1
Tetrahedral brace	393.62	510.08	529.46	572.2	878.08	1013.4

2.2 Vibration Stability of Tiled-Grating Device

In the device, the adjustment of the grating relies on the collective effect of the three drivers. Actuators 1 and 2 directly act on grating drivers 1 and 2, while

actuator 3 transmits the driving force to grating driver 3 through the connection rod. When only actuator 3 is operating, the grating will rotate around the X axis. This movement is shown in Fig. 5a; in this situation, there is only one degree of freedom. Slider A represents the piezoelectric actuator, Y represents the position of the piezoelectric actuator, the connection rod AB represents the rear connection rod, and the grating is along BC. Thus, the position of slider A is described by the equations:

$$\begin{cases} Y = r \sin \alpha - L \sin \beta \\ L \cos \beta + r \cos \alpha = b \end{cases} \quad (1)$$

The partial derivatives of Eq. (1) are:

$$\frac{\partial Y}{\partial r} = \frac{\cos(\alpha + \beta)}{\sin \beta}, \quad \frac{\partial Y}{\partial L} = \frac{1}{\sin \beta}, \quad \frac{\partial Y}{\partial b} = -\cot \beta. \quad (2)$$

Thus, we can see that the error transmission factors of each component, $\partial Y/\partial r$, $\partial Y/\partial L$, and $\partial Y/\partial b$, change with α , which is the angle between the grating surface and the horizontal plane. A plot of the values of the three error transmission factors against the angle α is shown in Fig. 4.

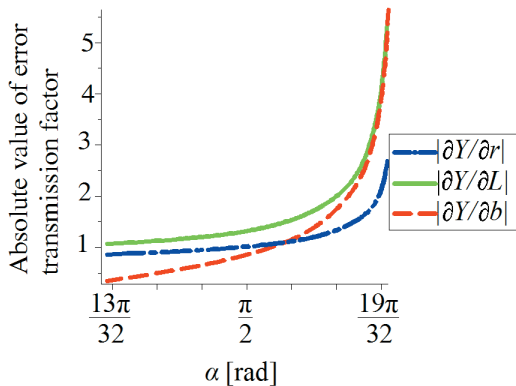


Fig. 4. Plot of the transmission error of each component against the angle α

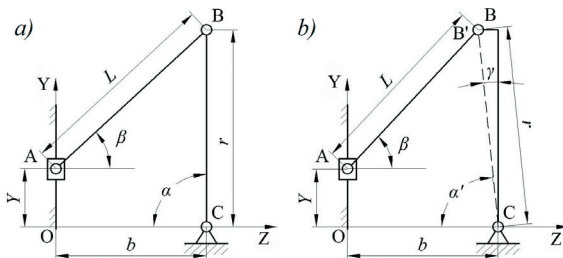


Fig. 5. Improvement of the mechanism for rotating about the X axis

As shown in Fig. 4, within the considered value range, the three error transmission factors increase with α . For each error transmission factor, when it reaches a certain point, its value begins to increase rapidly. This means that the adjustment precision and stability of the grating are greatly affected. In order to decrease the impact of the growing error transmission factor, as shown in Fig. 5b, we moved the previous grating's adjustment point from the point B to the point B'; the grating itself remained in the same position, along the segment BC. Moving the grating's adjustment point decreases the angle α to $\alpha' = \alpha - \gamma$, as shown in Fig. 5b. Decreasing this angle effectively shifts the operating point on each of the curves, as shown in Fig. 6. Therefore, the region of rapid increase is effectively avoided and the error transmission factors are lower in the new scheme.

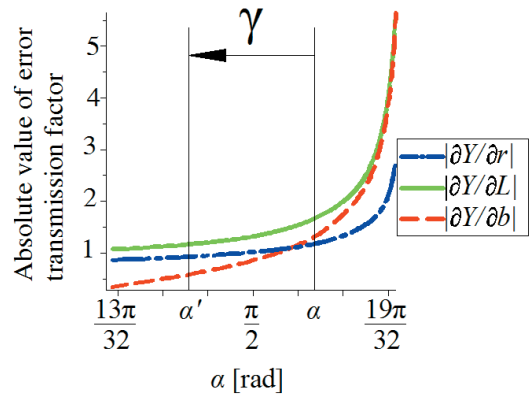


Fig. 6. The impact of the improvement about the error of each component against the angle α

This result is equivalent to that obtained by adding a virtual tripod ($\Delta BCB'$) to support the grating and fixing this tripod to the original unmodified tiled device. However, the current tiled device has avoided the region with rapidly increasing error transmission factors, ensuring good adjustment precision and stability values.

After the improvement, an experiment is carried out to test the vibration stability. The measuring points are the points labeled "Max" in Fig. 3, and the test time is 60 s. The experimental environment is different from the idealized simulation environment, so there are some acceptable differences between the two results. As shown in Fig. 7, the range of the vibration is narrower than before the improvement, which we regard as evidence that the vibration stability is improved under this new scheme. Statistical measures of the vibration in the two designs are given in Table 2.

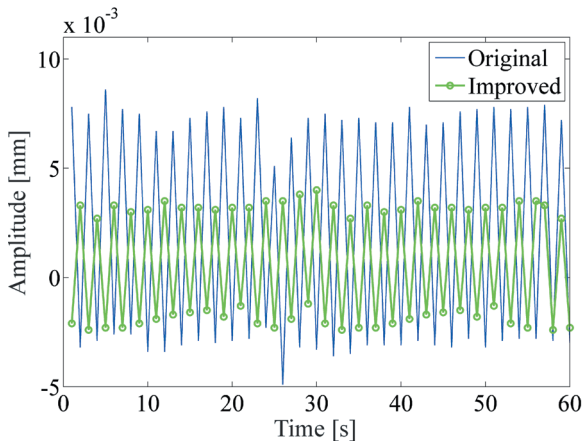


Fig. 7. Z-directional vibration comparison between the two tiled-grating devices

Table 2. Statistical measures of the vibration of the two tiled-grating devices

	Max [mm]	Average [mm]	Variance
Original	0.015	0.006	3.20×10^{-5}
Improved	0.0057	0.002	6.80×10^{-6}

2.3 Control Stability

2.3.1 Actuator Placement

As shown in Fig. 8, the component for adjusting the three degrees of freedom employed three actuators, numbered 1, 2, and 3, which respectively act on drivers 1, 2, and 3. Actuator 3 acts on the vertical central line of the rectangular grating’s geometric center O. Actuators 1 and 2 act on the two sides of the vertical central line J.

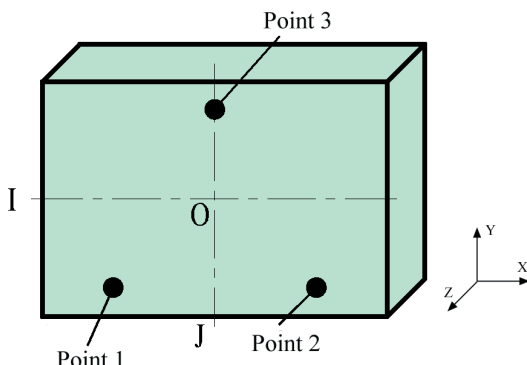


Fig. 8. Schematic showing the locations of the drivers

The grating adjustment action is chosen based on Table 3. When actuators 1, 2, and 3 translate the grating in the same direction at the same time with the same displacement, the grating is translated along

the Z axis by an amount Δz . When actuator 3 stops and actuators 1 and 2 translate their respective points in opposite directions at the same time and with the same displacement, a rotation about the Y axis by an amount $\Delta\theta_y$ is realized, and the central axis of this rotational adjustment is J. The spin degree of freedom around the X axis is realized when actuators 1 and 2 translate their respective points in the same direction at the same time with the same displacement while actuator 3 is translating in the opposite direction, and all three actuators impart the same displacement. A displacement can be added to this pure rotation by changing the amount of displacement associated with actuator 3. The central axis of this rotational adjustment is the horizontal central line I. Thus the adjustment of the three degrees of freedom of the grating is realized.

Table 3. Relationship between the actions of the piezoelectric actuators and the DOF adjustments

Actuator	Adjusted direction	$+\theta_x$	$-\theta_x$	$+\theta_y$	$-\theta_y$	+Z	-Z
	1	0	0	+Z	-Z	+Z	-Z
2	0	0	-Z	+Z	+Z	-Z	
3	+Z	-Z	0	0	+Z	-Z	

2.3.2 Actuator Control Algorithm

The scheme for controlling the actuator in this work is based on using 1) an incremental PID control algorithm, 2) a latch compensation method to avoid the saturated loss caused by the integrated saturation, and 3) the four-point central difference method to obtain differential parameters for anti-disturbance processing.

As shown in Fig. 9, the theory of the latch compensation method is based on comparing the controlled quantity u with the controlled quantity of the actuator u_{max} : if $u < u_{max}$, then we use u ; if $u > u_{max}$, then we use u_{max} . In addition, the difference $\Delta u = u - u_{max}$ is stored in a latch and added to the next u value. There is an obvious advantage to doing so, which is that although the last saturated loss is discarded, all the other controlled quantities are used, and the result is predictable and can be controlled within u_{max} .

In the digital PID algorithm, the disturbance corresponding to differential terms has a considerable effect on the control results. In PID control, it is generally necessary to adjust the differential terms although they cannot be eliminated easily. While

the tiled-grating environment is standardized, there are many parameters that can change. The working environment of precise tiled gratings is subject to various disturbances [10] to [12]. All disturbances will impact the stability to a certain extent. In order to keep the grating stable over a long period of time and constrain most disturbances, we adopted the four-point central difference method [13] to modify the differential terms so as to control the disturbances. The basic theory is as shown in Fig. 10; the improved algorithm, when constructing a differential term, uses not only the current deviation but also the average deviations of the four-sample spot in the past and the present and then weights the sum to get a differential function similar to the form of Eq. (4), shown below. From signal processing theory, we know that by using the differential version of this method instead of the difference method, we can double the SNR (signal-to-noise ratio) [14].

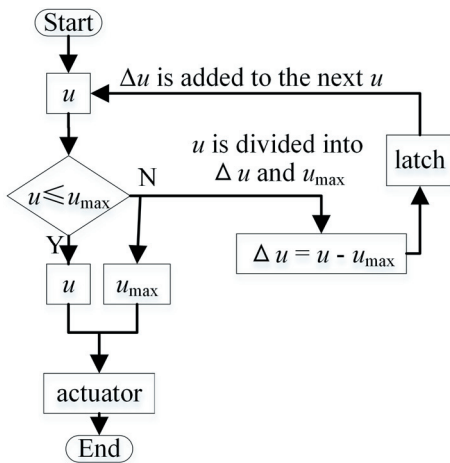


Fig. 9. Diagram of the latch compensation method

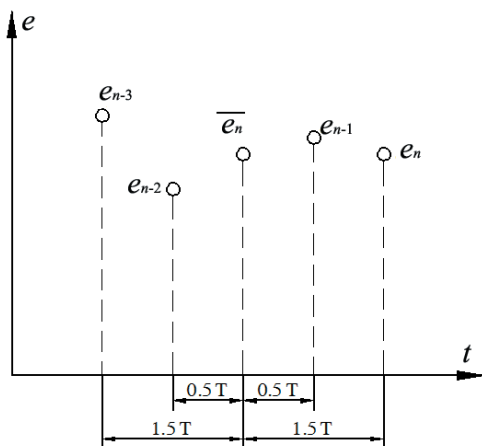


Fig. 10. Four-point central difference method

The general format of an incremental PID algorithm is:

$$\Delta u_n = K_p(e_n - e_{n-1}) + K_i e_n + K_d(e_n - 2e_{n-1} + e_{n-2}), \quad (3)$$

where K_p is the proportionality factor, K_i is the integration factor, K_d is the differential factor, and n indexes the samples.

Using the four-point central difference method to process the differential factor, we get:

$$\Delta e_n^- = \frac{1}{6}(e_n + 3e_{n-1} - 3e_{n-2} - e_{n-3}). \quad (4)$$

Using Δe_n^- as a substitute for $e_n - 2e_{n-1} + e_{n-2}$ in Eq. (3), we can obtain the improved incremental PID algorithm:

$$\Delta u_n = K_p(e_n - e_{n-1}) + K_i e_n + \frac{1}{6} K_d(e_n + 2e_{n-1} - 6e_{n-2} + 2e_{n-3} + e_{n-4}). \quad (5)$$

We can see from the previous equation that the control increment in the incremental PID algorithm was improved using the four-point central difference method, because the short-term fluctuation is flattened to some extent. This mitigates the short-term fluctuation to a certain extent and reduces the impact caused by environmental disturbances. Furthermore, based on the step response shown in Fig. 11, the response speed of the improved PID algorithm is enhanced.

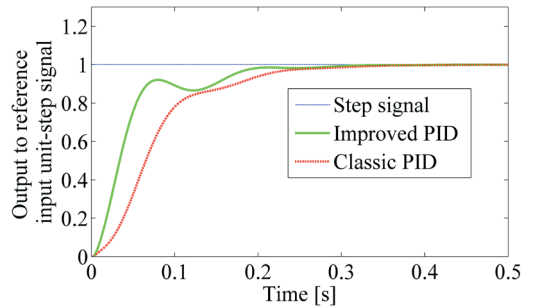


Fig. 11. Unit-step responses of the improved and classical incremental PID algorithms

3 EXPERIMENTAL VERIFICATION OF STABILITY OF TILED-GRATING DEVICE

3.1 Experimental Test

To test and verify the stability of the prototype (Fig. 12) of the tiled-grating device, with existing resources, we designed a testing scheme, shown in Fig. 13.

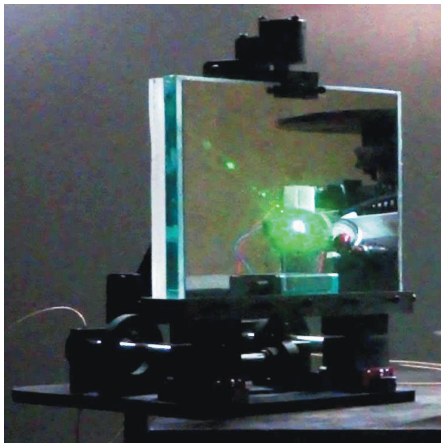


Fig. 12. Prototype of the tiled-grating device

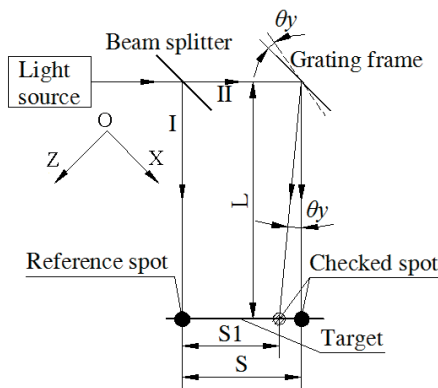


Fig. 13. Schematic of the stability-testing scheme

There are four chief components: a 532 nm laser (which serves as the optical source), a 1:1 beam splitter, the tiled-grating device, and a target. The beam splitter and the tiled-grating device are parallel to each other, at a 45° angle with respect to the laser, 5 meters from the target. The laser beam emitted by the laser source is divided into two beams with equal energies, which we refer to as beams I and II. Beam I is projected onto the target after being reflected by the beam splitter; beam II is transmitted to the beam splitter and then projected onto the target after being reflected by a mirror on the tiled-grating device. Then, there are two spots on the target, as shown in Fig. 15. We use a camera to capture a photo of the spots on the target and obtain the relative position of the checked spot after image processing. In the process, the center of the spot is found to be the brightest position and it is used in calculations. In the tiled-grating device, the actuators are PSt 150/4/100 VS20 piezoelectric actuators, which include mechanical packaging, and the controller is a XE-500/501 PZT controller. Both the actuator and controller are manufactured by

Harbin Core Tomorrow Science & Technology Co., Ltd. The resolution of the camera is 2 megapixels, and its frame rate is 5 FPS.

In this stability experiment on the tiled-grating device, the general method for checking the far-field focal spot is not applied. If we used that method, whether the spot is focused would be checked qualitatively but not quantitatively; this is because the sharpness of the spots would change with changes to the displacement when the two spots are very close together (Fig. 14). When the computer program would analyze such images, the central point would be different in each image, and different measurement errors would be produced. It would therefore be difficult to obtain an accurate calculation. In our experiment, the spot's sharpness will remain unchanged, as shown in Fig. 15. Thus, all of the data produced by the image recognition program has the same measurement error in all of the images.

The displacement between the two spots is defined as ΔS , which is used to characterize the vibration of the tiled grating device. The position of the reference spot in No.n image is defined as S_{rn} and its measuring error is E_{rn} . Correspondingly, the position of the checked spot in No. n image is defined as S_{cn} and its measuring error is E_{cn} . Therefore, the distance between the two spots is $S_n = (S_{rn} + E_{rn}) - (S_{cn} + E_{cn})$. The relative displacement between the two spots is the distance difference between the two spots among neighboring images, that is, $\Delta S = S_{n+1} - S_n$. Because the measuring error remained unchanged, $E_{sn} = E_{s0}$ and $E_{cn} = E_{c0}$ always exist. Therefore,

$$\begin{aligned} \Delta S_n &= S_{n+1} - S_n = \\ &= [(S_{r(n+1)} + E_{r(n+1)}) - (S_{c(n+1)} + E_{c(n+1)})] - \\ &\quad - [(S_{rn} + E_{rn}) - (S_{cn} + E_{cn})] = \\ &= (S_{r(n+1)} - S_{rn}) - (S_{c(n+1)} - S_{cn}). \end{aligned} \quad (2)$$

The measuring error is removed. Here, the subscript 0 is the initial.

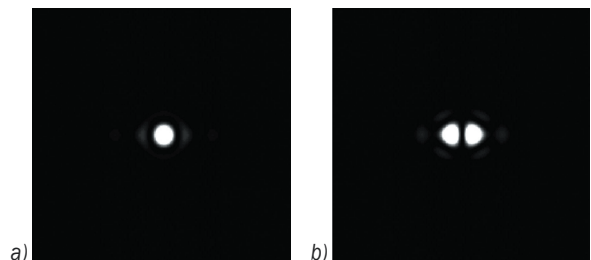


Fig. 14. Photographs of spots that are close together; a) focal spot and b) split spot [15]

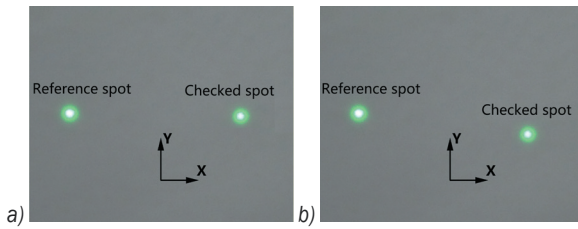


Fig. 15. Photographs of spots that are far apart; a) original configuration and b) after shifting

The angular deflection response of the grating around the Y axis is:

$$\theta_y = \arctan(\Delta S_x / L). \quad (6)$$

The angular deflection response of the grating around the X axis is:

$$\theta_x = \arctan(\Delta S_y / L). \quad (7)$$

3.2 Analysis of Experimental Results

In the process of the dynamic response testing, the total time over which the photographs of the spots are collected is 380 s, and the collection time interval is 4 s, resulting in a total of 96 photos. We use MATLAB to apply image processing to the photos collected by the camera and to find the relation between the time and the displacement response of the checked spot in the X and Y directions.

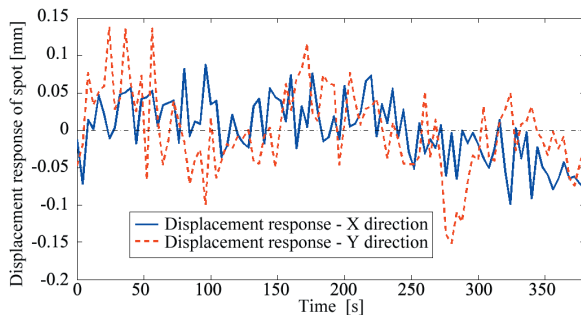


Fig. 16. Displacement response curves of the checked spot in the X and Y directions

From Fig. 16, we can see that the displacement response amplitude of the precision tiled-grating device in the Y direction is significantly greater than that in the X direction. With increasing time, the displacement response of the device shows no obvious increasing or decreasing trend, instead staying around the zero-displacement line.

The statistics in Table 4 show that the variance yields of the displacement responses in the X and Y directions reached a level of 10^{-4} , which shows

that the amplitude of the average deviation of the displacement response is low. Therefore, it is practical to use the average value of the displacement response to represent the average value of the entire displacement response.

Table 4. Statistical characteristics of the checked-spot displacement in the X and Y directions

Direction	Max. amplitude	Average value	Variance yields
X [mm]	9.84×10^{-2}	-7.03×10^{-6}	1.77×10^{-4}
Y [mm]	1.51×10^{-1}	-1.17×10^{-3}	3.06×10^{-4}

We substitute the average values of the displacement responses in the X and Y directions into the angle formulas, Eqs. (6) and (7), and find that the angular deflection response around the X axis of the precision tiled-grating device is:

$$\theta_x = \arctan(1.17 \times 10^{-3} / 5000) = 0.234 \mu\text{rad}.$$

The corresponding value around the Y axis is:

$$\theta_y = \arctan(7.30 \times 10^{-6} / 5000) = 1.46 \times 10^{-3} \mu\text{rad}.$$

This result shows that the angular deflection responses around the X and Y axes are $0.243 \mu\text{rad}$ and $1.46 \times 10^{-3} \mu\text{rad}$ respectively, which satisfy the design requirement [10] of the SG-III system that the single-angle drift be less than $0.48 \mu\text{rad}$.

4 CONCLUSION

High stability is one of the critical requirements for a tiled grating. To determine how to realize a tiled grating with high stability, we analyzed the stabilities of newly designed tiled-grating devices.

1. The analysis results show that after the tiled-grating device is modified from the parallel-board structure to the tetrahedral structure, the natural frequency in Phase I is enhanced, and the maximum displacement of the device is transferred from the grating surface to the brace so that the vibration stability of the tiled grating is obviously improved.
2. Through investigation of the transmission errors of the device and the addition of a virtual tripod to avoid the region where the error transmission factor rapidly increases, we decreased the growth speed of the error transmission factor, and the impact on the control error was reduced.
3. To enhance the control stability of the device, a) we adopted a latch compensation method and the four-point central difference method to improve the PID control algorithm used by the device; b)

we avoided the saturated loss, and the impact of environment disturbances was reduced; and c) the response speed was increased.

4. Our experiment showed that the stability of the sample device satisfied the target requirements of Ref. 10: over 380 s, the grating-angle drifts in the X and Y directions were $0.243 \mu\text{rad}$ and $1.46 \times 10^{-3} \mu\text{rad}$ respectively.

5 ACKNOWLEDGEMENT

This work was supported by the Research Fund for the Doctoral Program of Higher Education (20110191110006).

6 REFERENCES

- [1] Sharma, A., Kourakis, I. (2009). Laser pulse compression and amplification via Raman backscattering in plasma. *Laser Part Beams*, vol. 27, no. 04, p. 579-585, DOI:10.1017/S0263034609990292.
- [2] Hornung, M., Bödefeld, R., Siebold, M., Kessler, A., Schnepf, M., Wachs, R., Sävert, A., Podleska, S., Keppler, S., Hein, J., Kaluza, M.C. (2010). Temporal pulse control of a multi-10 TW diode-pumped Yb: glass laser. *Applied Physics B*, vol. 101, no.1-2, p. 93-102, DOI:10.1007/s00340-010-3952-7.
- [3] Kessler, T.J., Bunkenburg, J., Huang, H., Kozlov, A., Meyerhofer, D.D. (2004). Demonstration of coherent addition of multiple gratings for high-energy chirped-pulse-amplified lasers. *Optics Letters*, vol. 29, no. 6, p. 635-637, DOI:10.1364/OL.29.000635.
- [4] Blanchot, N., Bar, E., Behar, G., Bellet, C., Bigourd, D., Boubault, F., Chappuis, C., Coïc, H., Damiens-Dupont, C., Flour, O., Hartmann, O., Hilsz, L., Hugonnot, E., Lavastre, E., Luce, J., Mazataud, E., Neauport, J., Noailles, S., Remy, B., Sautarel, F., Sautet, M., Rouyer, C. (2010). Experimental demonstration of a synthetic aperture compression scheme for multi-Petawatt high-energy lasers. *Optics Express*, vol. 18, no. 10, p. 10088-10097, DOI:10.1364/OE.18.010088.
- [5] Guo-lin, Q., Jian-hong, W., Chao-ming, L. (2011). Laser pulse pattern influenced by mosaic grating gap. *High Power Laser and Particle Beams*, vol. 23, no. 12, p. 3177-3182, DOI:10.3788/HPLPB20112312.3177. (in Chinese)
- [6] Yan-lei, Z., Xiao-feng, W., Qi-hua, Z., Xiao, W., Yi, G., Zheng, H., Hong-jie, L., Chun-tong, L. (2006). Design of an arrayed grating compressor based on far-field. *High Power Laser and Particle Beams*, vol. 18, no. 10, p. 1619-1624. (in Chinese)
- [7] Zhong-xi, S., Qing-chun, Z., Qing-shun, B., Hong-ya, F. (2009). Design method of controlling device for tiling high precision and large aperture grating. *Optics and Precision Engineering*, vol. 17, no. 1, p. 158-165. (in Chinese)
- [8] Zhou, Y., Shen, C., Zhang, J., Wang, X., Zhou, H. (2011). Structure design of high accuracy 2×2 array grating. *High Power Laser and Particle Beams*, vol. 23, no. 7, p. 1741-1745, DOI:10.3788/HPLPB20112307.1741. (in Chinese)
- [9] Jun-wei, Z., Xiao, W., Dong-hui, L., Hai, Z., Liang-ming, C., Xiao-min, Z., Feng, J. (2011). Dynamic Response Control and Analysis of Large Aperture Tiled Grating Mount. *Acta Optica Sinica*, vol. 31, no. 1, p. 158-162, DOI:10.3788/aos201131.0112010. (in Chinese)
- [10] Mei-cong, W., Gang, C., Zhan, H., Xiao-juan, C., Wen-kai, W., Jun, W., Ming-zhi, Z. (2011). Stability design of switchyard in SGIII facility. *Optics and Precision Engineering*, vol. 19, no. 11, p. 2664-2670, DOI:10.3788/OPE.20111911.2664. (in Chinese)
- [11] Burkhart, S.C., Bliss, E., Di Nicola, P., Kalantar, D., Lowe-Webb, R., McCarville, T., Nelson, D., Salmon, T. (2011). National Ignition Facility system alignment. *Applied Optics*, vol. 50, no. 8, p. 1136-1157, DOI:10.1364/AO.50.001136.
- [12] Bernardin, J., Parietti, L., Martin, R. (1998). Thermal Issues Associated with the HVAC and Lighting Systems Influences on the Performance of the National Ignition Facility Beam Transport Tubes. Los Alamos National Lab., Los Alamos, DOI:10.2172/567499.
- [13] Jinbiao, W. (2004). *Computer Control System*. Tsinghua University Press, Beijing. (in Chinese)
- [14] Wen-bao, L., Li-xin, X., Xian-yi, Z. (1996). Research on Digital Control of Scanning Mirror Precise Servo System. *Electrical Drive Automation*, vol. 18, no. 04, p. 18-23. (in Chinese)
- [15] Jun-wei, Z., Wei, C., Na, X., Yi, Z., Hai, Z., Xiao, W., Feng, J., Xiao-min, Z. (2012). Design and demonstration of a tiled-grating frame. *Optical Engineering*, vol. 51, no. 1, p. 013007-1-013007-5, DOI:10.1117/1.OE.51.1.013007.

Estimation of Transient Temperature Distribution during Quenching, via a Parabolic Model

Diego E. Lozano^{1,*} – Gabriela Martinez-Cazares² – Rafael D. Mercado-Solis² – Rafael Colás² – George E. Totten³

¹ FRISA, México

² Autonomous University of Nuevo Leon, México

³Portland State University, USA

A material-independent model to estimate the transient temperature distribution in a test probe quenched by immersion is presented in this study. This model is based on the assumption that, under one-dimensional unsteady heat conduction, the radial temperature distribution at the end of an interval belongs to the equation of a parabola. The model was validated using AISI 304 stainless steel test probes ($\Phi 8 \times 40$ mm and $\Phi 12 \times 60$ mm) quenched from 850 to 900 °C in water and in water-based NaNO_2 solutions at 25 °C and in canola oil at 50 °C. Additionally, square test probes ($20 \times 20 \times 100$ mm) were quenched from 550 °C in water. The test probes were equipped with embedded thermocouples for temperature-versus-time data logging at the core, one-quarter thickness and 1 mm below the surface. In each experiment, the data recordings from the core and near-surface thermocouples were employed for the temperature calculations while the data from the one-quarter thickness thermocouple were employed for model validity verifications. In all cases, the calculated temperature distributions showed good correlations with the experimentally obtained values. Based on the results of this work, it is concluded that this approach constitutes a simple, quick and efficient tool for estimating transient surface and radial temperature distributions and represents a useful resource for quenchant cooling rate calculations and heat transfer characterizations.

Keywords: temperature distribution, quenching, parabola, heat transfer coefficient, cooling rate, cooling curve analysis

Highlights

- Parabolic model to calculate transient temperatures during the quenching.
- Only the temperature histories of two points in the radial direction are needed.
- The direct usage of simple algebraic equations minimizes calculation times with good accuracy.
- The solutions are independent of material thermo-physical properties.
- Heat transfer coefficient is directly solved via Fourier's law of heat conduction.
- The model is an alternative to the Inverse Heat Conduction Problem (IHCP).

0 INTRODUCTION

In heat treatment technology, quenchant with improved heat transfer properties and enhanced hardening capacities are under continuous development. In order to test such attributes, a common practice is to equip test probes with one or more thermocouples for temperature-versus-time data logging during a quenching cycle. By doing so, the speed at which heat is extracted from within the test probe (i.e. the cooling rate) can be calculated by means of cooling curve analyses, as per ISO 9950 [1], ASTM D6200 [2], ASTM D6482 [3] and ASTM D6549 [4], etc. From the metallurgical point of view, the knowledge of the cooling kinematics at the various heat transfer stages during the quenching of steel is an aspect of key practical importance. In this sense, a martensitic as-quenched microstructure would result from a sufficiently high cooling rate in order to avoid the pearlitic and bainitic transformations in the higher temperature range while cracking and distortion could be minimized by slower cooling kinematics

in the martensitic transformation range at lower temperatures [5].

The cooling curves extracted from instrumented test probes may also be employed in the estimation of the surface temperature during quenching [6] and [7]. This may be further extended to calculate the heat transfer coefficient (HTC) and the heat flux densities (HFD) [8] to [11]. These two parameters adequately describe the overall heat transfer characteristics of a quenching system. The most popular technique for performing these calculations is the so-called inverse heat conduction problem (IHCP). In principle, the IHCP relies on the numerical solution of Fourier's well-known partial differential equation [12]. To solve the IHCP, the local temperature history (cooling curve) of one point inside the test probe should be known. Based on an initial "guess" of the HTC, an iterative calculation process is started to match the calculated temperature history with the measured one. In this way, the surface temperature may be estimated from the HTC values and from the thermo-physical properties of the test probe material (i.e. density,

*Corr. Author's Address: FRISA S.A. de C.V., Santa Catarina, Nuevo Leon, Mexico, diego.lozano@frisa.com

thermal conductivity and specific heat capacity, etc.) within the quenching temperature range.

Although the effectiveness of the IHCP has been extensively verified [13], the correct solution to the problem always remains largely dependent upon inputting the right thermo-physical properties, which are not easily measured. This is perhaps the main downside of the IHCP.

In this paper, a relatively simple and straightforward approach for estimating transient temperature distributions and the surface temperature of a quenched part is presented. This model is based on the assumption that the temperature distribution inside the body follows a parabolic-type behaviour [14]. Thus, it may be regarded as an alternative to the IHCP, with the advantage that no thermo-physical properties are needed in the calculations, and that the direct usage of simple algebraic equations minimizes calculation times with acceptable accuracy.

1 DESCRIPTION OF THE PARABOLIC MODEL

During the cooling of symmetric bodies under one-dimensional heat conduction, the assumption is made that the radial temperature distribution at the end of an interval belongs to an upside down parabola that is symmetric about the y axis defined as $y = -ax^2 + c$ and whose origin is at the center of the body at an arbitrary temperature [14]. Thus, by making the y axis the temperature and the x axis the radial distance from the center, the temperature T_c at the core of the bar ($x_c = 0$) then corresponds to the vertex of the parabola, i.e. $y = c = T_c$ (Fig. 1). Similarly, the temperature T_2 at a radial distance from the centre x_2 also belongs to the aforementioned parabola, and is, therefore, defined as:

$$T_2 = -ax_2^2 + T_c. \tag{1}$$

Therefore, by solving Eq. (1) for a , we obtain:

$$a = \frac{T_c - T_2}{x_2^2}. \tag{2}$$

Based on the model assumptions, the temperature T_{rth} at any given radial distance from the center x_{rth} at the end of an interval shall also belong to the parabola, and is defined in the most general form as:

$$T_{rth} = -ax_{rth}^2 + T_c. \tag{3}$$

By substituting Eq. (2) in (3), we obtain:

$$T_{rth} = (T_2 - T_c) \left(\frac{x_{rth}}{x_2} \right)^2 + T_c. \tag{4}$$

In summary, the implications of Eq. (4) are such that, during the cooling of a cylinder, the temperature of any point along the radial direction may be calculated if the temperatures of another two points along the same direction (T_2 and T_c) are simultaneously known.

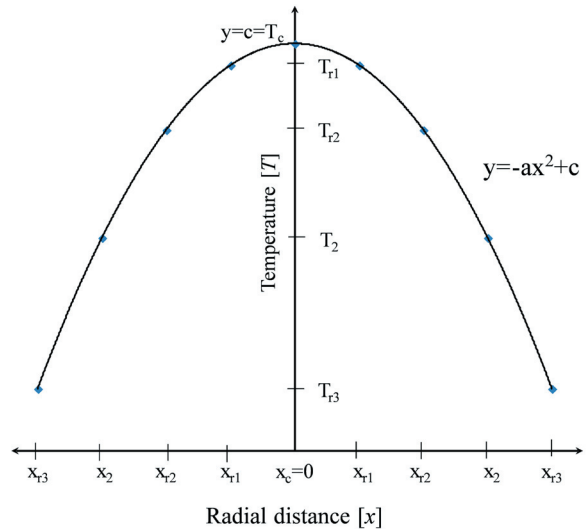


Fig. 1. Parabolic temperature as a function of radial distance at the end of a quenching interval

2 EXPERIMENTAL VALIDATIONS

In order to validate the parabolic model, a series of quenching experiments were performed using instrumented AISI 304 stainless steel test probes. In accordance with the minimum diameter-to-length ratio (1:4) practicable for one-dimensional heat conduction [15], two sizes of round cross-sectional test probes were fabricated: $\phi 8 \times 40$ mm and $\phi 12 \times 60$ mm. Additionally, square cross-sectional test probes $20 \times 20 \times 100$ mm were also quenched for comparison. Three $\phi 1$ mm blind holes were drilled in each test probe up to their mid-length at the core, one-quarter thickness and 1 mm below the quenched surface, as shown in Fig. 2. K-type thermocouples were tightly embedded in the holes for temperature-versus-time data logging during quenching. In order to prevent water from entering the thermocouple holes, zirconium oxide paint was used as a sealant. The thermocouples were differentially connected to a data acquisition card (NI USB-6211) using a 75 k Ω resistor between the negative of the thermocouple and the ground for a high electrical reference. Data was acquired at a rate of 100 samples per second and then smoothed through a cubic spline interpolation algorithm. This is an adequate method to

obtain an accurate global approximation over the time range [15].

The quenching experiments are summarized in Table 1. Quenchings were carried out inside a glass reservoir that contained 12 litres of quenchant. Tap water and sodium nitrite (NaNO₂) aqueous solutions at concentrations of 1 and 9% wt. were employed as quenchants. The initial temperature of the water and the water-based quenchants was 25 °C, while that of the oil was 50 °C. During the quenching experiments, a localized quenchant temperature increase (up to ~45 °C) was recorded with a thermocouple placed 50 mm away from the probe surface, but this increase was only limited to the regions adjacent to the test probe, while the overall temperature of the quenchant remained almost unchanged. After each experiment, the quenchant was stirred and left to cool down to 25 °C before the next experiment. The round test probes were quenched from temperatures of 850 and 900 °C, while the square test probes were quenched from 550 °C.

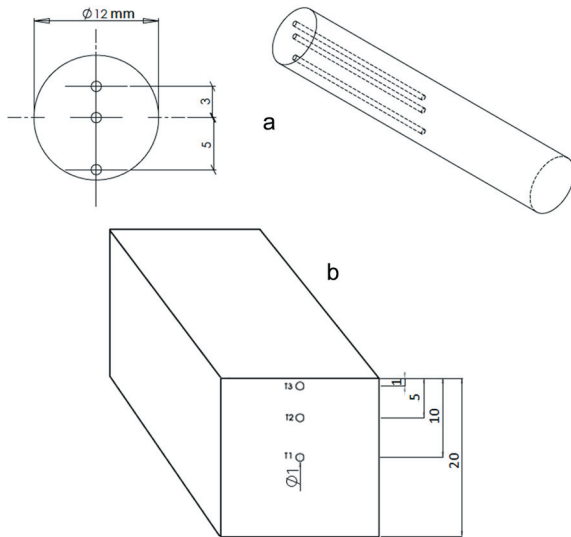


Fig. 2. Drawings of the test probes and thermocouple positions; a) $\varnothing 12$ mm round test probe; b) square test probe

For each quenching experiment, the logged temperatures at the core (T_c) and at the near-surface (T_{ns}) were input into the parabolic equation along with their radial distances. Therefore, the one-quarter thickness temperature (T'_q) and the surface temperature (T_s) were calculated. Thus, for the new experimental notation, Eq. 4 may be suitably rewritten as:

$$T'_q = (T_{ns} - T_c) \left(\frac{x_q}{x_{ns}} \right)^2 + T_c, \quad (5)$$

$$T_s = (T_{ns} - T_c) \left(\frac{x_s}{x_{ns}} \right)^2 + T_c. \quad (6)$$

The one-quarter thickness temperature readings were employed for model self-validations by comparing the experimentally obtained values (T_q) with the calculated ones (T'_q) through Eq. (5). The temperature difference T_{diff} between T'_q and T_q and their percent error were calculated for each quenching experiment as:

$$T_{diff} = |T'_q - T_q|, \quad (7)$$

$$\% \text{ error} = \frac{T_{diff}}{T_q} \times 100. \quad (8)$$

Table 1. Summary of quenching experiments

Experiment	Type	Size [mm]	Temp. [°C]	Quenchant
1	Round	$\varnothing 8 \times 40$	850	Water
2	Round	$\varnothing 8 \times 40$	850	9% NaNO ₂
3	Round	$\varnothing 8 \times 40$	900	Canola oil
4	Round	$\varnothing 12 \times 60$	900	1% NaNO ₂
5	Square	$20 \times 20 \times 100$	550	Water

3 RESULTS AND DISCUSSION

The cooling curves obtained experimentally, and the calculated temperatures at the surface and one-quarter thickness are shown in the top charts of Figs. 3 to 7. The temperature difference and the percentage of error between the experimental and the calculated values at the one-quarter thickness are presented in the bottom part of the same figures. Fig. 3 shows the results of Experiment 1, in which, although the calculated curve does not generally overlap the experimentally measured one, they do follow the same trend. The maximum temperature difference occurred at the start of cooling where its influence upon the percentage of error is less due to the higher temperature values.

The average error during the first 3 seconds was 4%, while the average temperature difference was 17 °C. This is the interval where the curves overlapped less. Thereafter, the curves showed a good fit, and the highest temperature difference between the two remained within 6 °C and the error below 6%. Notice that the calculated surface temperature curve drops to 100 °C (boiling point of water) and, except for the small reheating obtained due to the internal heat source, the temperature remained near the

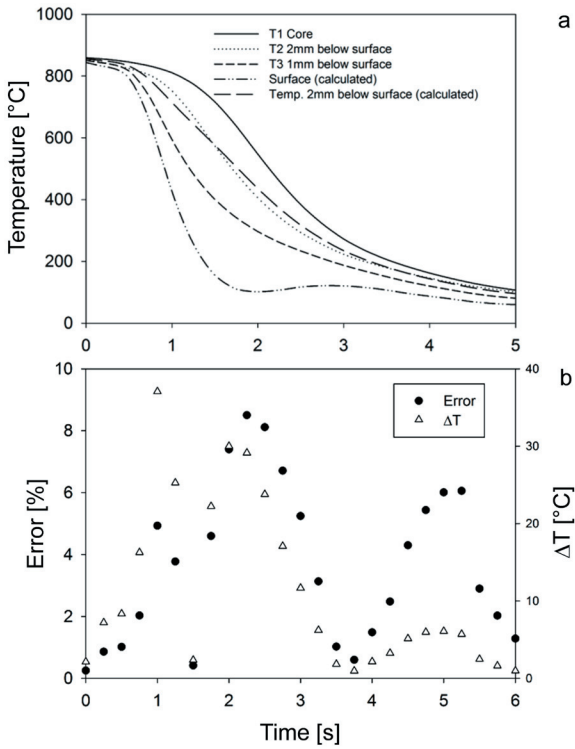


Fig. 3. Cooling curves of Experiment 1; a) temperature versus time, b) error % and temperature difference versus time

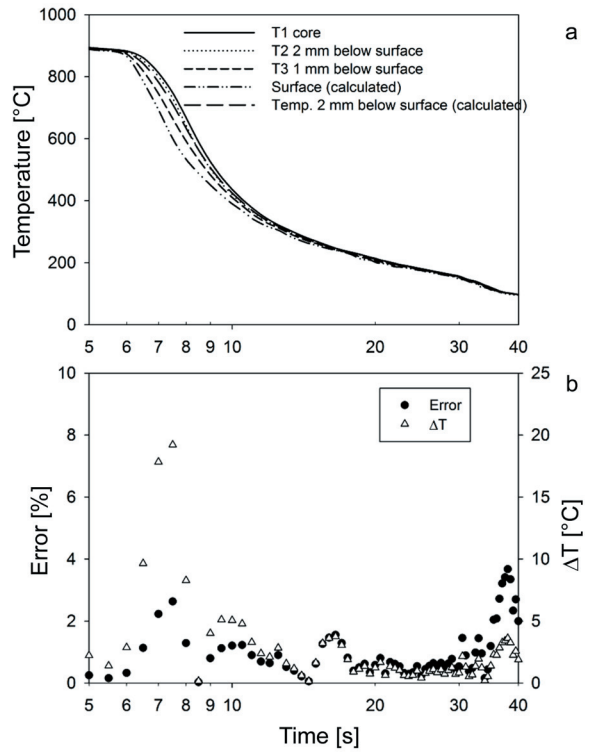


Fig. 5. Cooling curves of Experiment 3; a) temperature versus time, b) error % and temperature difference versus time

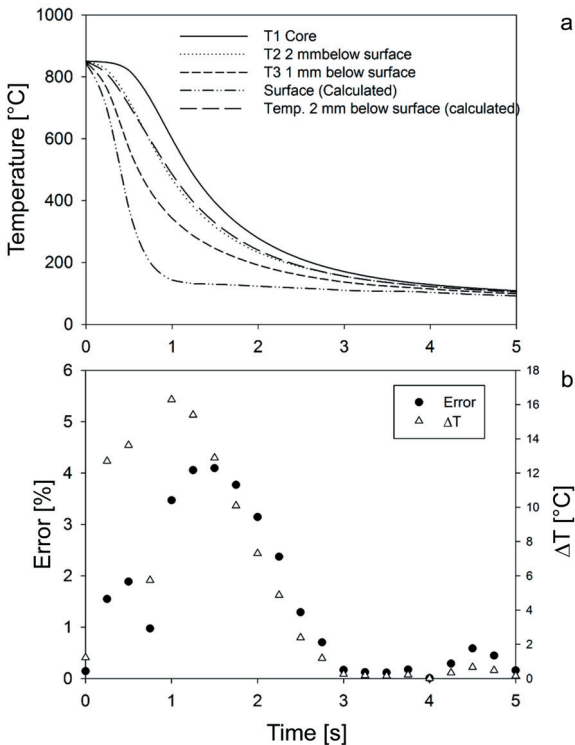


Fig. 4. Cooling curves of Experiment 2; a) temperature versus time, b) error % and temperature difference versus time

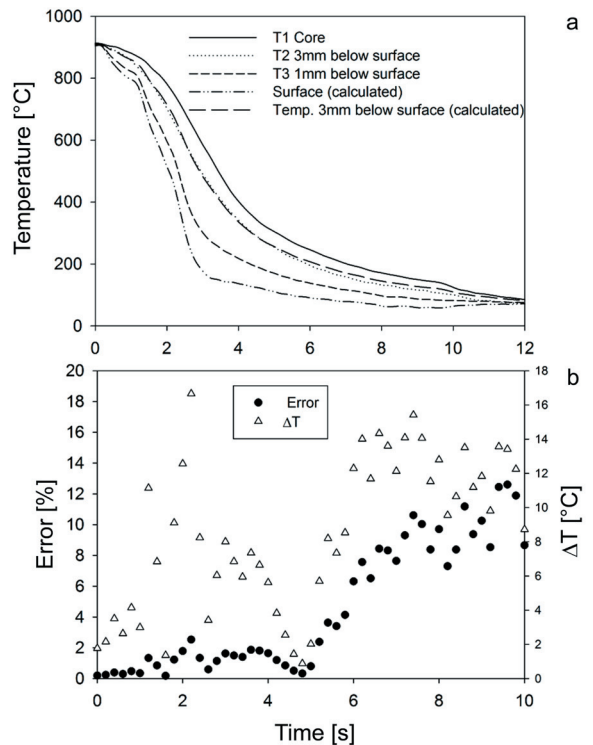


Fig. 6. Cooling curves of Experiment 4; a) temperature versus time, b) error % and temperature difference versus time

boiling point. This phenomenon is a self-regulating thermal process, in which the surface temperature does not cool below this point until sufficient heat has been extracted from the bulk of the probe [16]. Furthermore, since no agitation was used during quenching, localized heating of the quenchant up to its boiling point occurs. Thus, the surface becomes locally surrounded by the quenchant at the same temperature of the surface until the free convection of the fluid mixes it with the quenchant mass from more distant areas.

In Experiment 2 (Fig. 4), a similar quenching was performed, except that sodium nitrite (NaNO_2) was added in the water at 9% wt concentration to promote a more severe cooling. Here, the film boiling (vapour) stage at the start of quenching is effectively suppressed. The boiling point of water is increased by salt additions and, thus, the surface temperature is expected to remain above 100°C . From Fig. 4, it can be observed that, during the first three seconds, the error between the measured and the calculated temperatures reached a maximum of 4% and the maximum temperature difference was 16°C . The average error and temperature difference for the first three seconds were 2.15% and 8°C , respectively. At quenching intervals between 3 and 5 seconds, the average values were as low as 0.7% error and 0.7°C temperature difference. The calculated surface temperature decreased to 133°C due to the higher boiling temperature of the salt solution.

The cooling curves of Experiment 3 corresponding to the 8mm diameter bar quenched in canola oil are shown in Fig. 5. The heat extraction capacity of the vegetable oil is considerably lower than that of water and water-based salt solutions. Therefore, lower thermal gradients between the surface and the core of the test probe were measured. Since the temperature difference between the thermocouples was small, the error when calculating the temperature distribution was also small. The average error was only 1.8%, and the average temperature difference was 0.8°C throughout the full quenching interval. For most of the time range, the error between the experimental and the calculated temperatures was less than 5°C .

Increasing the size of the sample did not produce any changes in the parabolic temperature distribution, as shown in the results of Experiment 4 (Fig. 6). Here, a 12mm diameter bar was quenched in 1%wt NaNO_2 aqueous solution. The calculated temperature using the parabola equation overlapped the experimental curve. The temperature difference always remained below 16°C . On average, the error was 6.6% and the temperature difference 9°C .

In addition to the round bars, a bar of square cross-section was instrumented and quenched. The long square bar exhibits one-dimensional heat conduction at mid-thickness as would a slab. For Experiment 5 (Fig. 7), the square bar was heated to 550°C followed by quenching in water at 25°C . At the start of cooling, a stable vapour blanket formed around the probe. The calculated T'_q temperature does not match the experimental data initially. This may be due to the inefficient heat transfer conditions established during this quenching stage and geometric effects. After the first 3 seconds, at which point the error reached 10% and the temperature difference reached a high value of 50°C , the calculated data overlapped the experimental curve with a small difference of 4.5°C and progressed to an almost exact fit thereafter.

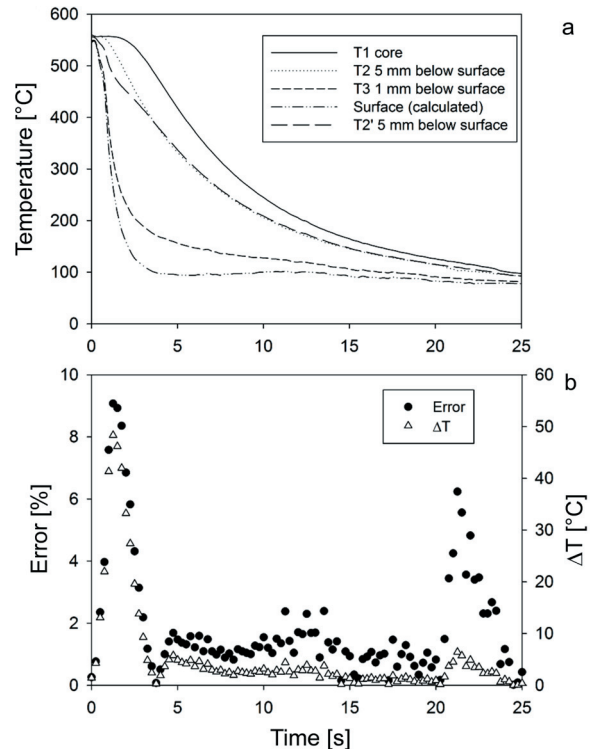


Fig. 7. Cooling curves of Experiment 5; a) temperature versus time, b) error % and temperature difference versus time

4 COOLING RATE CALCULATION EXAMPLE

The rate at which cooling of the probes proceeds at any instant during quenching is determined by Newton's Law of Cooling. Here, a practical example of the use of cooling curve analyses for cooling rate calculations is presented for Experiments 2 and 3. The procedure involves the adjustment of the best-fit mathematical expression to each temperature-versus-

time data set and its subsequent derivation; thus, dT/dt is the cooling rate, which can be conveniently plotted against temperature and/or time. Fig. 8 shows the cooling rates obtained from Experiment 2 and the corresponding (calculated) surface temperature. It can be observed that the vapour phase is entirely suppressed; hence, very high cooling rates are achieved in the early stages of quenching at high temperatures. The addition of NaNO_2 to the water result in high cooling rates reaching a maximum value of $1,300^\circ\text{C/s}$ as the surface temperature lowered to 700°C . It is noteworthy that the maximum cooling rate is around 40% higher at the surface that just 1 mm below it and 60% higher than the core.

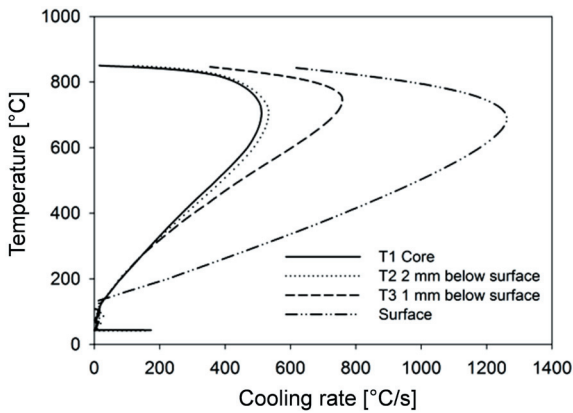


Fig. 8. Cooling rates of Experiment 2

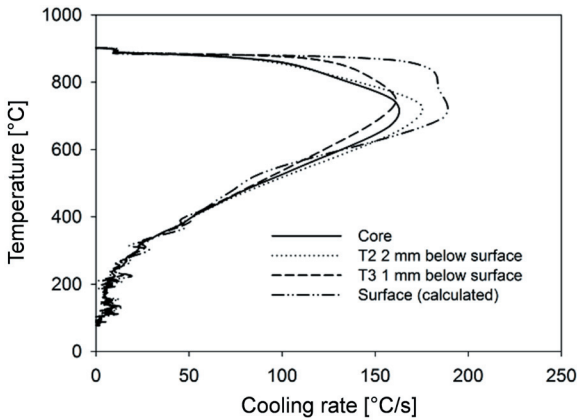


Fig. 9. Cooling rates of Experiment 3

Similarly, the calculated cooling rates from Experiment 3 are shown in Fig. 9, where the film boiling phase was noticed at the start of quenching. After the vapour blanket was destabilized, the nucleate boiling phase is present until 350°C was reached, followed by the convection stage. Due to the absence of large thermal gradients, the rate of cooling is nearly the same inside the test probe and on its surface

throughout the quenching cycle. Thus, the maximum cooling rate was 185°C/s at a surface temperature of 700°C .

5 HEAT TRANSFER COEFFICIENT CALCULATION EXAMPLE

An example is presented for the calculation of the interfacial heat transfer coefficient from the surface temperature profile obtained through the parabolic model (appendix I). In references [15] and [17], Liščić and Filetin produced the experimental cooling data of the Liščić-Petrofer probe ($\phi 50 \times 200 \text{ mm}$) quenched in low viscosity accelerated quenching oil at 50°C . These data have been reproduced in Fig. 10 and the surface temperature was calculated using the parabolic model.

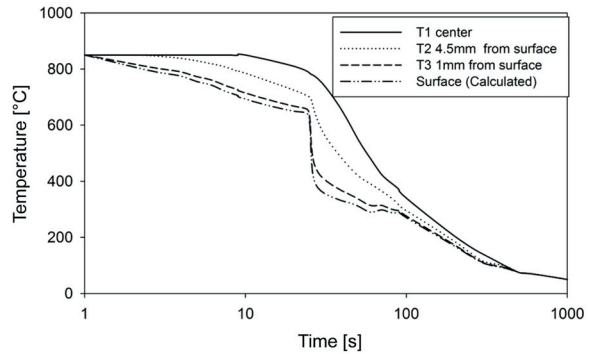


Fig. 10. Experimental cooling data from references [15] and [17] and surface temperature calculation via the parabolic model

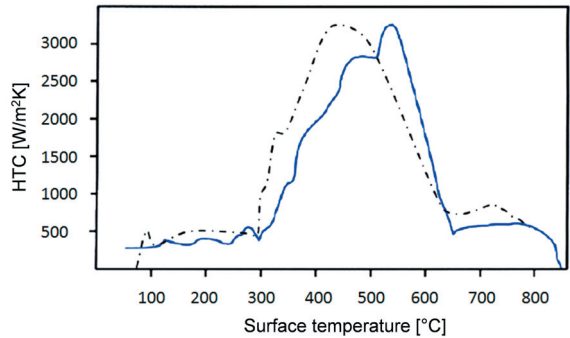


Fig. 11. Comparison of heat transfer coefficient calculation between the IHCP [15] and [17] and the parabolic model

Fig. 11 shows the comparison of the HTC results reported by Liščić and Filetin [15] and Liščić et al. [17] by solving the IHCP (solid line) and by the calculated surface temperature profile via the parabolic method in this study (dashed line). The maximum value of HTC calculated by the two methods matched $3,200 \text{ W/m}^2\text{K}$. Moreover, a good agreement in the trend of the two curves was found. However, the surface

temperature at which the maximum HTC occurs in each method differs by approximately 100 °C, i.e. the parabolic HTC curve is shifted towards the lower temperature range. In Liščić's method, the maximum value of HTC takes place when the maximum cooling rate of the surface occurs, whereas in the parabolic method, the maximum value of HTC takes place when the largest thermal gradient is set in the test probe.

6 CONCLUSIONS

The parabolic model can correctly capture the radial temperature profile of test probes of various sizes and quenching media. For the analysis, only the temperature histories of two points in the radial direction are needed. Therefore, it provides the advantage that no thermo-physical properties are required, and the direct usage of simple algebraic equations minimizes calculation times with acceptable accuracy. Based on the results, it was concluded that this method is better suited for quenching in oil for which overly strong thermal gradients are not present, although entirely acceptable results were also obtained for water and aqueous solution quenchants. Once the surface temperature has been calculated, the procedure to determine the heat transfer coefficient and the heat flux density is highly simplified through the direct solution of the heat flux via Eq. (12) of Appendix.

7 ACKNOWLEDGEMENTS

The authors wish to thank the following institutions for their support: Universidad Autonoma de Nuevo Leon, Facultad de Ingenieria Mecanica y Electrica and Consejo Nacional de Ciencia y Tecnologia (CONACYT-Mexico).

8 REFERENCES

- [1] ISO 9950:1995. *Industrial Quenching Oils— Determination of Cooling Characteristics—Nickel-Alloy Probe Test Method*. International Organization for Standardization, Geneva
- [2] ASTM Standard D6200-01 (2012). *Standard Test Method for Determination of Cooling Characteristics of Quench Oils by Cooling Curve Analysis*. ASTM International, West Conshohocken.
- [3] ASTM Standard D6482-06 (2011). *Standard Test Method for Determination of Cooling Characteristics of Aqueous Polymer Quenchants by Cooling Curve Analysis with Agitation (Tensi Method)*. ASTM International, West Conshohocken.
- [4] ASTM Standard D6549-06 (2011). *Standard Test Method for Determination of Cooling Characteristics of Quenchants by Cooling Curve Analysis with Agitation (Drayton Unit)*. ASTM International, West Conshohocken.
- [5] Luty, W. (2010). *Cooling media and their properties. Quenching Theory and Technology 2nd ed.* Liscic, B., Tensi, H.M., Canale, L.C.F., Totten, G.E. (eds.). CRC Press, Boca Raton, DOI:10.1201/9781420009163-c12.
- [6] Meekisho, L., Hernandez-Morales, B., Tellez-Martinez, J.S., Chen, X. (2005). Computer-aided cooling curve analysis using WinProbe. *International Journal of Materials and Product Technology*, vol. 24, p. 155-169, DOI:10.1504/IJMP.2005.007946.
- [7] Hernandez-Morales, B., Lopez-Sosa, F., Cabrera-Herrera, L. (2012). A new methodology for estimating heat transfer boundary conditions during quenching of steel probes. *Proceedings of 6th International Quenching and Control of Distortion Conference*, p. 81-92.
- [8] Hasan, H.S. (2009). *Evaluation of Heat Transfer Coefficients during Quenching of Steels*. PhD. thesis, University of Cambridge, Cambridge.
- [9] Felde, I. (2012). Estimation of heat transfer coefficient obtained during immersion quenching. *Proceedings of 6th International Quenching and Control of Distortion Conference*, p. 447-456
- [10] Lubben, T., Rath, J., Krause, F., Hoffman, F., Fritsching, U., Zoch, H. (2012). Determination of heat transfer coefficient during high-speed water quenching. *International Journal of Microstructure and Materials Properties*, vol. 7, no. 2-3, p. 106-124, DOI:10.1504/IJMMP.2012.047494.
- [11] Felde, I. (2012). Determination of thermal boundary conditions during immersion quenching by optimization algorithms. *Materials Performance and Characterization*, vol. 1, no. 1, p. 1-11, DOI:10.1520/MPC104417.
- [12] Beck, J.V. (1970). Nonlinear estimation applied to the nonlinear inverse heat conduction problem. *International Journal of Heat and Mass Transfer*, vol. 13, p. 703-716, DOI:10.1016/0017-9310(70)90044-X.
- [13] Landek, D., Župan, J., Filetin, T. (2014). A prediction of quenching parameters using inverse analysis. *Materials Performance and Characterization*, vol. 3, no. 2, p. 229-241, DOI:10.1520/MPC20130109.
- [14] Harding, R.A. (1976). *Temperature and Structural Changes during Hot Rolling*. PhD thesis, University of Sheffield, Sheffield.
- [15] Liščić, B., Filetin, T. (2012). Measurement of quenching intensity, calculation of heat transfer coefficient and global database of liquid quenchants. *Materials Engineering - Materiálové inžinierstvo*, vol. 19, no. 2, p. 52-63.
- [16] Kobasko, N.I. (2012). Effect of accuracy of temperature measurements on determination of heat transfer coefficient during quenching in liquid media. *Journal of the ASTM International*, vol. 9, no. 2, p. 126-141 DOI:10.1520/JA1104173.
- [17] Liščić, B., Filetin, T., Landek, D., Župan, J. (2014). Current investigations at quenching research centre. *Materials Performance and Characterization*, vol. 3, no.2, p. 3-18, DOI:10.1520/MPC20130102.
- [18] Holman, J.P., (1997). *Heat Transfer. 8th ed.* McGraw-Hill, New York.

9 APPENDIX:
HEAT TRANSFER COEFFICIENT CALCULATION

If a semi-infinite hot cylinder is suddenly quenched, then the heat flux will occur in one dimension according to Fourier's law of heat conduction. The energy balance for convection is therefore expressed as [18]:

$$-kA \left. \frac{\partial T}{\partial x} \right|_{\text{surface}} = hA(T_{\text{surface}} - T_{\infty}) \quad (9)$$

The finite-different numerical solution of unsteady-state conduction with convection boundary condition:

$$-k \frac{\Delta y}{\Delta x} (T_{m+1} - T_m) = h \Delta y (T_{m+1} - T_{\infty}), \quad (10)$$

or:

$$T_{m+1} = \frac{T_m + (h\Delta x/k)T_{\infty}}{1 + (h\Delta x/k)}, \quad (11)$$

where T_{m+1} is the surface temperature, T_m is the near-surface temperature, Δx is the distance between the two positions, T_{∞} is the quenchant temperature, h is the heat transfer coefficient and k is the thermal conductivity.

If the surface and near-surface temperatures are known, then the heat transfer coefficient may be calculated as:

$$h = -\frac{k}{\Delta x} \frac{(T_{m+1} - T_m)}{(T_{m+1} - T_{\infty})}. \quad (12)$$

Modelling and Analysis of Step Response Test for Hydraulic Automatic Gauge Control

Yi Jiangang*

¹ Jiangnan University, Hubei Key Laboratory of Industrial Fume & Dust Pollution Control, China

The step response for hydraulic automatic gauge control (HAGC) determines the steel rolling speed and the steel sheet thickness in the process of rolling production. In this paper, the step response test process of HAGC was analysed, and a test approach was proposed for it. Based on that, the transfer function model of the step response test was established and simulated by using Matlab. In order to reduce the settling time and the overshoot, an adaptive proportional-integral-derivative (APID) link was presented in order to compensate for the input signal by using back propagation neural networks (BPNN). The experimental results show that the improved step response test model reaches the process requirements of HAGC, eliminates the jitter of the HAGC system at the start-up phase, and has better stability as well as faster response for steel sheet rolling.

Keywords: step response, hydraulic automatic gauge control, proportional-integral-derived controller, artificial neural networks

Highlights

- Proposed the step response test model of HAGC system.
- The working parameters study of the model.
- Presented an APID link for signal compensation.
- Representation of the stability and the flexibility on step response of the HAGC system.

0 INTRODUCTION

Sheet gauge is one of the main quality indicators for steel sheet in the process of rolling production. To improve the control precision of sheet gauge, hydraulic automatic gauge control (HAGC) is currently widely used. In the process of HAGC, the step response plays the most important role, because it determines the steel rolling speed and the steel sheet thickness, and accordingly influences steel sheet surface quality. The step response test is a time-domain test method for system dynamic characteristics. It is used to describe the dynamic response process of the control system when the input is a step signal. To achieve uniform thickness of a steel sheet, the step response parameters of the HAGC should be adjusted according to the real-time thickness of steel sheet. However, during the step response process of HAGC, the step response parameters are influenced by the interactions of hydraulic cylinders, servo valves, and various sensors of the system, and the working time is extremely short (no more than 1 second). Consequently, it is of vital importance to model, test, and analyse the step response of HAGC.

In terms of HAGC system design, Wang et al. and Taleb et al. developed a real-time simulator for a hot-rolling mill based on a digital signal processor, which can be used for controlling the hydraulic cylinder in an HAGC system [1] and [2]. Gao et al. proposed a simulated model of 1100 mm rolling mill HAGC

system by using position-pressure compound control method [3]. T.S. Tsay presented a command tracking error square control scheme, and designed feedback control systems [4]. To achieve good control effect, many researchers studied the control algorithm of HAGC. Ang et al. and Mitsantisuk et al. researched the general design method of control system with proportional-integral-derived controller (PID) [5] and [6]. Zhang et al., Dou et al. and Chang et al. analysed the PID parameters setting problem [7] to [9]. Their research proved that the PID controller with proper parameters was efficient, but the setting of the PID parameters is the main problem. To achieve the desired strip thickness of the HAGC system, Khosraviet al. and Song et al. proposed a novel fuzzy adaptive PID controller [10] and [11]. The simulation results showed that it was better than traditional PID controller, but sensitive to parameter variations. Wan et al. and Kasprzyczak et al. analysed the main parameters of the hydraulic system and discussed their effects on system stability [12] to [13].

To solve the problem of multivariable parameters adjustment of the PID controller, several authors proposed some intelligent algorithms, such as evolutionary algorithms, particle swarm optimization (PSO), artificial neural networks (ANN) and generalized predictive control method [14] to [18]. The results indicated the intelligent algorithms improved the adaptability of the PID controller. However, the dynamic response process of the controller under step-

input was not discussed. In the literature, the research put emphasis on the design, analysis and control of HAGC, and few papers studied the step response test of HAGC.

In this paper, the step response test of HAGC is analysed, a test approach is proposed, and a transfer function model of the step response test is established and simulated by using Matlab software. In order to reduce the settling time and the overshoot, an adaptive proportional-integral-derivative (APID) link is presented to compensate for input signal by using back propagation neural networks (BPNN). The experimental results show that the improved step response test model reaches the process requirements of HAGC, eliminates the jitter of the HAGC system at the start-up phase, and has better stability as well as a faster response for steel sheet rolling.

The structure of this paper is organized as follows. Section 1 introduces the parameters and the approach of the step response test of HAGC. Section 2 establishes the step response test model with transfer function. Section 3 simulates the proposed model by using Matlab, and presents the improved model of the step response test by adding an APID link based on BPNN. Section 4 contains the experiments and the analysis of the improved model. Section 5 is devoted to the conclusions.

1 THE STEP RESPONSE TEST OF HAGC

1.1 The Parameters of the Step Response Test

In Fig. 1, the x coordinate value of the response signal curve represents the step response time, and the y

coordinate value represents the displacement of the piston rod in the HAGC system. Next, the parameters of the step response test include the rise time t_r , the maximum overshoot M_p , and the settling time t_s . The rise time t_r is the time at which the response signal reaches the first steady-state output, as described in Eq. (1):

$$t_r = t_{0.9} - t_{0.1}, \tag{1}$$

where $t_{0.9}$ is the time at which the response signal is 90% of the first steady-state output, and $t_{0.1}$ is the time at which the response signal is 10% of the first steady-state output.

The difference between the response signal and steady-state output functions as the numerator, and the steady-state output as the denominator, the overshoot as the ratio of them. Next, the maximum overshoot M_p can be calculated by Eq. (2):

$$M_p = \frac{x_o(t_p) - x_o(\infty)}{x_o(\infty)} \times 100\%, \tag{2}$$

where $x_o(t)$ is the displacement of the piston rod at the time t , and t_p is the time at which the response signal reaches the peak.

In the step response process, the settling time t_s is also called the transition time, which represents the time at which the HAGC system reaches the steady-state. It is defined as the time at which the value of $x_o(t)$ satisfies Eq. (3):

$$|x_o(t) - x_o(\infty)| \leq 0.05x_o(\infty). \tag{3}$$

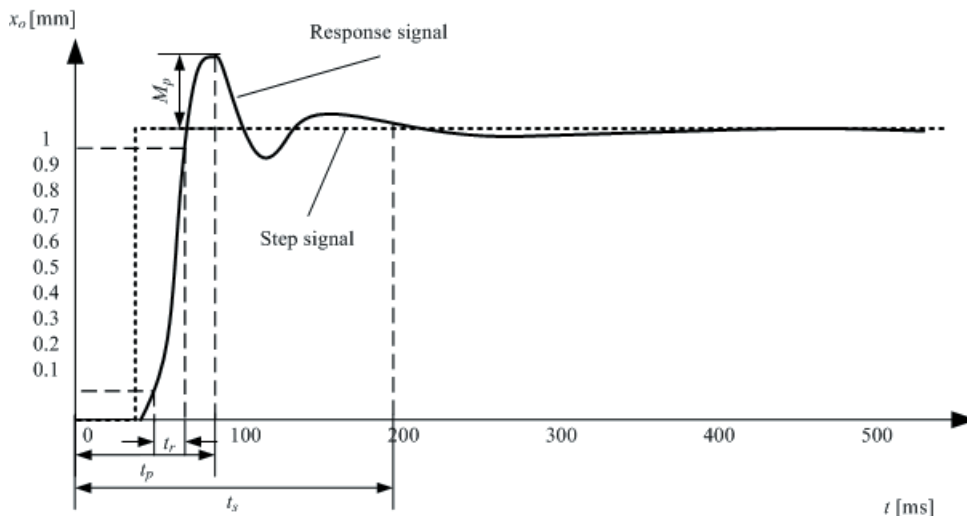


Fig. 1. The parameters of the step response test

In the parameters of the step response, the settling time t_s reflects the flexibility of the HAGC system, and the maximum overshoot M_p reflects the stability of HAGC system. In an HAGC system, it is always considered that the shorter of t_s and M_p , the better of the control effect.

1.2 The Approach of the Step Response Test

The main components in the step response process of HAGC are the servo valve, mill cylinder, current sensors, and displacement sensors. In order to simplify the test process, the influence of the hydraulic pipe and hydraulic power components is neglected. Next the approach of the step response test is shown in Fig. 2, and the main test steps are as follows:

Step 1: The displacement of step signal is given to the computer test software. It is converted to a voltage signal by the data acquisition card and is sent to the current sensor (6).

Step 2: The output signal of the data acquisition card is converted to current by the current sensor (6), and then is sent to the servo valve (5) to control the output flow in valve port A.

Step 3: According to the output flow in the valve port A, the piston rod (3) of mill cylinder 2 moves up-down to control the rolling thickness of steel sheet.

Step 4: The real-time displacement of the rolling thickness is measured by the displacement sensor (4), and then is converted to digital signal by the data acquisition card.

Step 5: The acquired digital signal is sent to the computer test software, which will be compared with the input displacement in Step 1 to determine the next input value.

2 MODELLING OF THE STEP RESPONSE TEST

2.1 The Parameters of the Step Response Test

According to Fig. 2, the step response test scheme is established, as shown in Fig. 3. The input signal U_v is the step signal of the expected displacement. The output signal Y_p is the real-time displacement of the mill cylinder, which is converted to the voltage signal U_p by the displacement sensor and fed back to the input port of the servo valve. The difference between U_v and U_p , U_e , is converted to the current signal by the current sensor and is used to drive the servo valve. The piston rod action of the mill cylinder is controlled by the output flow of the servo valve.

If the PID link is neglected and the input signals are sent to drive the servo valve directly, the transfer function of the servo valve is:

$$G_1(s) = \frac{K_{sv}}{\frac{s^2}{\omega_{sv}^2} + \frac{2\xi_{sv}}{\omega_{sv}}s + 1}, \quad (4)$$

where K_{sv} is the output flow gain of the servo valve, ω_{sv} is the natural frequency of the servo valve, and ξ_{sv} is the damping ratio of the servo valve.

The transfer function of the mill cylinder is:

$$G_2(s) = \frac{\frac{A_c}{KK_{ce}}}{\left(\frac{s}{\omega_r} + 1\right)\left(\frac{s^2}{\omega_h^2} + \frac{2\xi_h}{\omega_h}s + 1\right)}, \quad (5)$$

where ω_r is the transition frequency of the inertia, and ω_h and ξ_h are the natural frequency and the damping ratio of the mill cylinder. K_{ce} is the overall flow-pressure coefficient, K is the load stiffness, and A_c is the effective area of the piston rod of the mill cylinder.

The transfer function of the current sensor is:

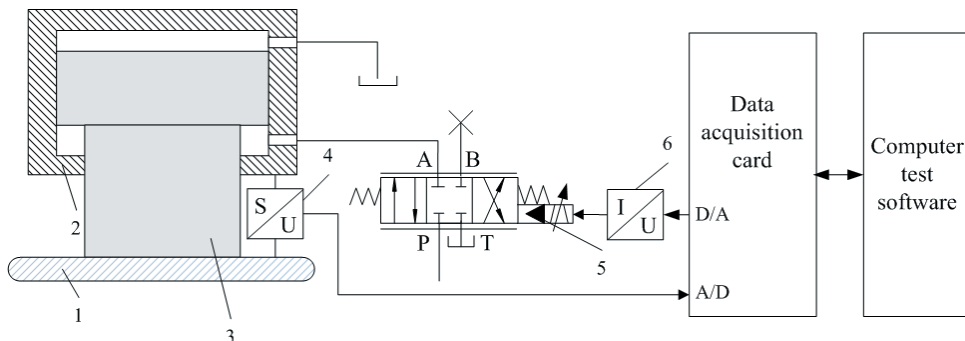


Fig. 2. The step response test of HAGC; 1-Steel sheet, 2-Mill cylinder, 3-Piston rod, 4-Displacement sensor, 5-Servo valve, 6-Current sensor

$$G_3(s) = K_i, \tag{6}$$

where K_i is the gain of current.

The transfer function of the displacement sensor is:

$$H(s) = K_s, \tag{7}$$

where K_s is the feedback coefficient of displacement.

2.2 Adding PID Link

To reduce the settling time and the maximum overshoot of HAGC, some researchers proposed compensating for the input signal by using some algorithms. The signal compensation is implemented by adding a new link to improve the system performance. Because the PID algorithm is flexible, and its parameters can be easily adjusted, it is widely used in control systems. Therefore, based on the step response test scheme, a PID link is added in the step response test scheme between the input signal U_e and the current sensor, as shown in Fig. 3.

The PID algorithm includes a proportional part, an integral part, and a differential part. Consequently, three coefficients, K_p , T_i and T_d , are used in PID controller for the system control, where K_p is the proportional coefficient, T_i is the integral coefficient, and T_d is the derivative coefficient. Therefore, the conventional PID algorithm can be described as:

$$G_4(s) = \frac{U_g}{U_e} = K_p + \frac{1}{T_i s} + T_d s. \tag{8}$$

In terms of Fig. 3 and Eqs. (4) to (8), the overall transfer function model of the step response test with conventional PID algorithm can be described as Eq. (9):

$$G(s)H(s) = \frac{K_{sv}}{\frac{s^2}{\omega_{sv}^2} + \frac{2\xi_{sv}}{\omega_{sv}}s + 1} \cdot \frac{\frac{A_c}{KK_{ce}}}{\left(\frac{s}{\omega_r} + 1\right)\left(\frac{s^2}{\omega_h^2} + \frac{2\xi_h}{\omega_h}s + 1\right)} \cdot K_i K_s \cdot \left(K_p + \frac{1}{T_i s} + T_d s\right). \tag{9}$$

3 SIMULATION AND IMPROVEMENT OF THE STEP RESPONSE TEST

3.1 Simulation of the Step Response Test

To analyse the control effect with and without a PID link in the step response test, the working parameters are loaded to the established transfer function model in the HAGC system, and the step response test is simulated by using the Simulink toolbox in Matlab software. The simulated model with the working parameters is shown in Fig. 4. In the simulated model, a step signal of 1 mm displacement is loaded at the input point, and the output result is shown as the blue dot curve in Fig. 5. In Fig. 5, it can be observed that $t_s = 140$ ms, $M_p = 25\%$. However, in the HAGC production process, it is necessary that $t_s < 100$ ms and $M_p < 10\%$ for steel sheet rolling. Therefore, the settling time and the maximum overshoot are beyond the range of the HAGC requirements, which means the step response test without a PID link cannot be used to drive the HAGC system directly.

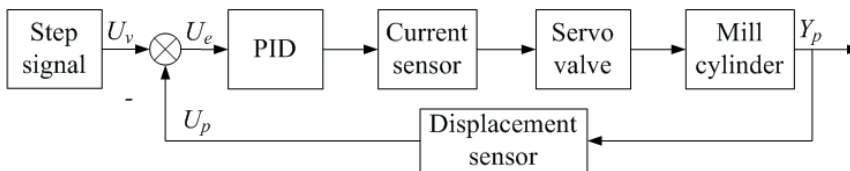


Fig. 3. The step response test scheme

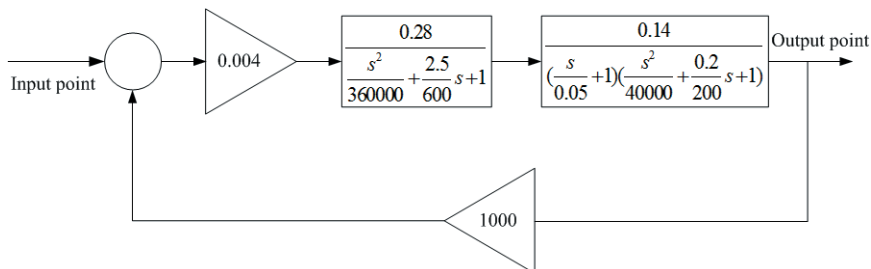


Fig. 4. The simulated model with working parameters

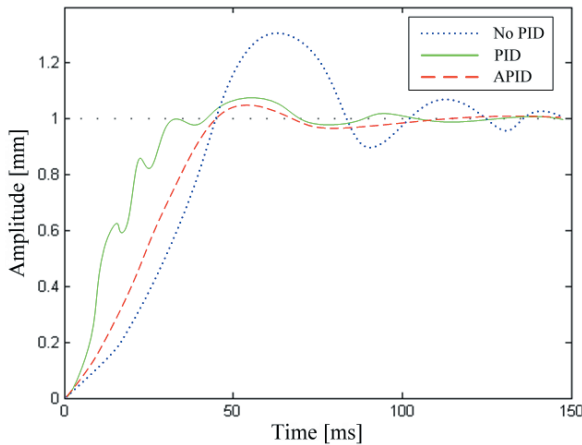


Fig. 5. The simulated results of the step response test

By adding the PID link in the established model in Fig. 4, the step response test is simulated with a conventional PID algorithm, and the output result is shown as a green solid curve in Fig. 5. It is found when $K_p = 10$, $T_i = 50$, and $T_d = 0$, the settling time $t_s = 80$ ms, and the maximum overshoot $M_p = 9\%$, which meet the process requirements of the HAGC. Moreover, testing shows that increasing K_p and T_d , and decreasing T_i can further reduce the values of t_s and M_p . However, at the same time, it leads to large jitters in the rise time of the step response test, which impairs the stability of the HAGC system.

3.2 Improvement of the Step Response Test

The simulation results of the model with a PID link indicate that the contradiction between the stability and flexibility of the HAGC system cannot be solved by the conventional PID algorithm. This is because the PID parameters of the conventional PID algorithm are constant during the process of the step response test, which cannot be adjusted according to the input and output signals adaptively. In the actual production of steel sheet, because of the interactions of the servo valve, mill cylinder, and sensors in the HAGC system, the step response is a nonlinear time-varying process.

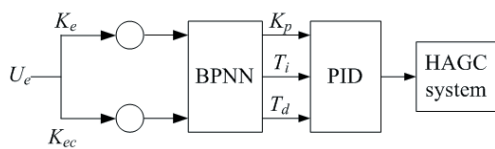


Fig. 6. The structure of the APID for HAGC system

As a result, an APID algorithm based on BPNN is proposed. The structure of the APID algorithm is shown in Fig. 6. The error K_e and the error change

rate K_{ec} of U_e as the input values of the ANN, and K_p , T_i and T_d as the output values, the BPNN is used to calculate the proper PID parameters by training it with acquired samples.

3.3 Implementation of APID

In recent years, many ANN algorithms have become widely used in both academic research and industrial development. In all ANN algorithms, BPNN is a multi-layer forward-spread network with a minimum mean square deviation learning method. It has been proved that BPNN can map all nonlinear functions with single layers. Therefore, a BPNN is created by using the Neural Networks toolbox in Matlab to implement the APID link of HAGC system. The BPNN is composed of an input layer with 2 neurons (K_e and K_{ec}), a hidden layer with 4 neurons (set in the neural networks toolbox) and an output layer with 3 neurons (K_p , T_i and T_d). The training function is TRAINLM, the adaption learning function is LEARNIGDM, and the transfer function is LOGSIG. The samples are collected from the steel sheet production of HAGC system. Table 1 lists 10 sets of the normalized data which are used as the training samples for the built BPNN.

Table 1. The training samples of the BPNN

Number	K_e	K_{ec}	K_p	T_i	T_d
1	0.442	0.193	0.056	0.071	0.010
2	0.095	0.794	0.150	0.076	0.093
3	0.119	0.101	0.097	0.070	0.105
4	0.094	0.099	0.620	0.588	0.197
5	0.893	0.545	0.212	0.092	0.081
6	0.792	0.152	0.078	0.063	0.098
7	0.541	0.085	0.038	0.041	0.033
8	0.113	0.125	0.255	0.119	0.100
9	0.867	0.048	0.243	0.008	0.025
10	0.133	0.020	0.135	0.009	0.011

The ability of ANN is generally measured by its mean-squared error (MSE). With the collected data in Table 1, the built BPNN is trained, and the change of the MSE is shown in Fig. 7. It can be seen when the training MSE goal is 0.01; the training times are no more than 500, which indicates that the proposed BPNN is convergent for APID control.

After the BPNN is trained, it can be used to calculate the APID parameters with current values of K_e and K_{ec} . The step response test of HAGC with the APID controller is simulated again by inputting the same values in the conventional PID controller ($K_e = 0.326$, $K_{ec} = 0.247$), and the result is shown as the red dashed curve in Fig. 5. In comparing the green

solid curve (PID) and the red dash curve (APID), it is obvious that by using the APID algorithm, the step response can not only reach the process requirements of the HAGC, but also eliminate the jitter at the start-up phase, which means the HAGC system has better stability and flexibility with the improved model.

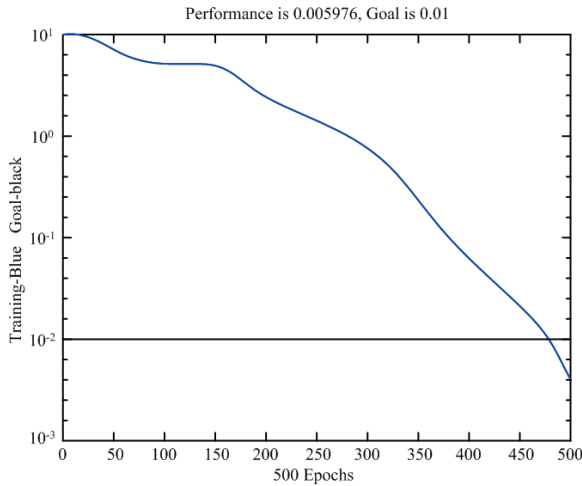


Fig. 7. The training result of the BPNN

4 EXPERIMENTAL RESULTS

In order to verify the established step response test model in Section 2 and Section 3, experiments were done with the designed HAGC system of the mill servo cylinder, as shown in Fig. 8. The type of the mill cylinder is C1450-P20N000, the piston rod diameter is 1450 mm, and the stroke length is 10 mm. The embedded computer servo controller receives the acquired signals from the sensors and the servo valves, and sends the calculated results to the HAGC system. The APID algorithm is programmed with Visual C++ and loaded into the HAGC controller. To test step response ability of the HAGC system, the standard step input signals were sent through the HAGC controller, as shown in Fig. 9a. The step response models without PID link, with conventional PID link and with APID link were tested, and the experimental results were shown on the HAGC controller screen, as shown in Fig. 9b. By comparing Fig. 5 and Fig. 9b, it can be determined that there is good agreement between the simulated and the experimental results.

By using the APID algorithm and conventional PID algorithm, the change of the steel sheet thickness within 100 ms is measured, as shown in Fig. 10. It can be seen that the thickness change in the step response test of HAGC with APID is no more than 0.06 mm, and the surface irregularity has a decreased trend as



Fig. 8. The HAGC system

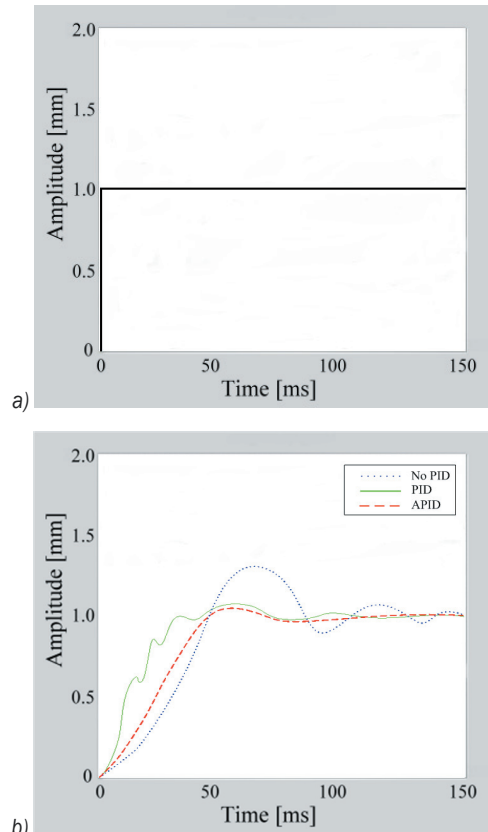


Fig. 9. The experimental results;
a) Input signal, b) Step response signals

time passed. The thickness change with conventional PID is about 0.30 mm, far above the value of APID. Consequently, the improved step response test model by using APID link can reduce the settling time and the overshoot, and thus enhance the surface quality of steel sheet in the HAGC system. This indicates

the improved step response model is valid, and the experimental results are consistent with the simulated results.

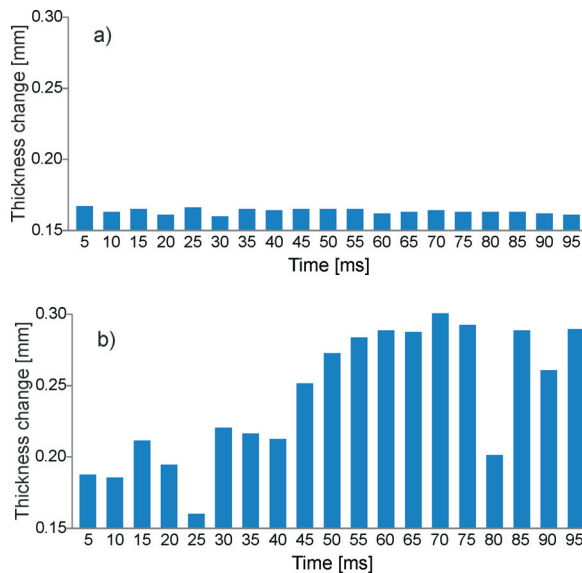


Fig. 10. The measured thickness change of steel sheet; a) with APID, b) with conventional PID

5 CONCLUSIONS

In the process of the step response test of HAGC, it is difficult to balance the stability and the flexibility of the system. To improve the control performance of the system, the approach of adding proper link to compensate for the input signal is valid. By adding a PID link, the settling time, and the overshoot can be reduced. However, the conventional PID algorithm also leads to jitters of HAGC at start-up phase. In this paper, based on the established step response test model, the APID link by using BPNN is proposed to improve steel sheet quality. The simulated and experimental results show that the designed step response model with the APID link is useful for overcoming jitters, reducing overshoot and settling time, and accelerating the dynamic response of the HAGC system. Further research to analyse the step response influence of the other components in HAGC systems, such as hydraulic pipes and hydraulic pumps, should be carried out.

6 ACKNOWLEDGMENT

This work is supported by the National Natural Science Foundation (Granted No: 51071077), China. The author also gratefully acknowledges the helpful

comments and suggestions of the reviewers, which have improved the presentation.

7 REFERENCES

- [1] Wang, Z., Sun, Y., Peng, K. (2006). Real-time simulator of an AGC system for hot-rolling mill. *Journal of University of Science and Technology Beijing*, vol. 28, no. 2, p. 171-174, DOI:10.3321/j.issn:1001-053X.2006.02.016. (in Chinese)
- [2] Taleb, R., Meroufel, A., Massoum, A. (2014). Control of a uniform step asymmetrical 13-level inverter using particle swarm optimization. *Automatika*, vol. 55, no. 1, p. 79-89, DOI:10.7305/automatika.2014.01.117.
- [3] Gao, Q.M., Li, J.F., Zhao, G.Q. (2010). Modeling and simulation of hydraulic AGC system for 1100mm cold rolling mill. *Applied Mechanics and Materials*, vol. 34-35, p. 523-526, DOI:10.4028/www.scientific.net/AMM.34-35.523.
- [4] Tsay T.S. (2007). Analysis and design of feedback control systems with tracking errors square. *Asian Journal of Control*, vol. 9, no. 3, p.333-339, DOI:10.1111/j.1934-6093.2007.tb00419.x.
- [5] Ang, K.H., Chong, G., Li, Y. (2005). PID control system analysis, design, and technology. *IEEE Transactions on Control Systems Technology*, vol.13, no.4, p. 559-576, DOI:10.1109/TCST.2005.847331.
- [6] Mitsantisuk, C., Nandayapa, M., Ohishi, K., Katsura, S. (2013). Design for sensorless force control of flexible robot by using resonance ratio control based on coefficient diagram method. *Automatika*, vol. 54, no. 1, p. 62-73, DOI:10.7305/automatika.54-1.311.
- [7] Zhang, Y., Shieh, L.-S., Liu, C.R., Guo, S.M. (2004). Digital PID controller design for multivariable analogue systems with computational input-delay. *IMA Journal of Mathematical Control and Information*, vol. 21, no. 4, p. 433-456, DOI:10.1093/imamci/21.4.433.
- [8] Dou, X., Guo, Q. (2008). Precise digital control system of a moving mirror's reciprocating move at even speed. *Journal of Control Theory and Applications*, vol. 6, no. 4, p. 431-434, DOI:10.1007/s11768-008-6159-2.
- [9] Chang, P.H., Jung, J.H. (2009). A systematic method for gain selection of robust PID control for nonlinear plants of second-order controller canonical form. *IEEE Transactions on Control Systems Technology*, vol. 17, no. 2, p. 473-483, DOI:10.1109/TCST.2008.2000989.
- [10] Khosravi, S., Afshar, A., Barazandeh, F. (2011). Design of a novel fuzzy adaptive PI controller for monitor hydraulic AGC system of cold rolling mill. *2nd International Conference on Instrumentation Control and Automation*, p. 53-58, DOI:10.1109/ICA.2011.6130129.
- [11] Song, X.Y., Yang, Q.J., Zhang, X.M., Feng, Q.G. (2009). Application of compound PID control in the DC servo motor. *Applied Mechanics and Materials*, vol. 16-19, p. 145-149, DOI:10.4028/www.scientific.net/AMM.16-19.145.
- [12] Wan, Y., Wu, C. (2012). Research on open-loop control dynamic characteristics of EHP controlled system based on compound model. *Advanced Science Letters*, vol. 6, no. 1, p. 257-260, DOI:10.1166/asl.2012.2269.

- [13] Kasprzyczak, L., Macha, E. (2008). Selection of settings of the PID controller by automatic tuning at the control system of the hydraulic fatigue stand. *Mechanical Systems and Signal Processing*, vol. 22, no. 6, p. 1274-1288, DOI:10.1016/j.ymssp.2007.08.014.
- [14] Iruthayarajan, M.W., Baskar, S. (2009). Evolutionary algorithms based design of multivariable PID controller. *Expert Systems with Applications*, vol. 36, no. 5, p. 9159-9167, DOI:10.1016/j.eswa.2008.12.033.
- [15] Ren, X, Du, F., Huang, H., , Yan, H. (2009). Application of fuzzy immune PID control based on PSO in hydraulic AGC press system. *International Conference on Intelligent Human-Machine Systems and Cybernetics*, p. 427-430, DOI:10.1109/IHMSC.2009.229.
- [16] Sabura Banu, U., Uma, G. (2008). Fuzzy gain scheduled continuous stirred tank reactor with particle swarm optimization based PID control minimizing integral square error. *Instrumentation Science and Technology*, vol. 36, no. 4, p. 394-409, DOI:10.1080/10739140802151499.
- [17] Wang, H., Rong, Y., Liu, S., Cui, J. (2010). Identification for hydraulic AGC system of strip mill based on neural networks. *International Conference on Computer Design and Applications*, (vol. 2), p. V2-377-V2-380, DOI:10.1109/ICCDA.2010.5541406.
- [18] Sun, M. (2010). Research on generalized predictive control in hydraulic AGC system of cold rolling mill. *2nd International Conference on Intelligent Human-Machine Systems and Cybernetics*, p. 159-162, DOI:10.1109/IHMSC.2010.139.

Failure Prediction of Cross-Ply Laminated Double-Serial Mechanically Fastened Composites using Fuzzy Expert System

Serkan Ballı^{1,*} – Faruk Sen²

¹ Muğla Sıtkı Koçman University, Faculty of Technology, Department of Information Systems Engineering, Turkey

² Muğla Sıtkı Koçman University, Faculty of Technology, Department of Energy Systems Engineering, Turkey

The scope of this study is to create a model that predicts failure loads for mechanically fastened composite plates using a fuzzy expert system. The composite material used in the study was manufactured in both a fibre reinforced manner and with glass fibres. The results of a previous experimental study for cross-ply laminated composite plates that were mechanically fastened with two serial pins or bolts were used to model and predict of failure loads. Furthermore, experimental data of a preceding study were obtained with different geometrical parameters for various applied preload moments (pinned/bolted) as 2, 3, 4 and 5 Nm. In this study, a fuzzy expert system and regression analysis methods were applied by using these geometrical parameters and pinned/bolted joint configurations. Therefore, 5 geometrical parameters and 300 test data were used. According to obtained results, it was determined that the fuzzy expert system was more appropriate than the regression analysis method for modelling and prediction. Performances of the fuzzy expert system and regression analysis method were discussed in terms of error ratios and mean absolute deviations.

Keywords: fuzzy expert system, bolted joint, pinned joint, fastened joint, laminated composites, fuzzy logic

Highlights

- Predicting failure loads for mechanically fastened composite plates using fuzzy expert system and regression analysis.
- Using composite material manufactured in both a fibre reinforced manner and with glass fibres.
- Creating a expert system model for prediction by applying fuzzy rules and fuzzy membership functions.
- Determination of more appropriate method for modelling and predicting of failure loads.

0 INTRODUCTION

Composite materials have been in existence for many centuries; no record exists as to when people first started using them. There are numerous other examples of both natural and man-made composite materials [1]. The improvement of advanced composite materials has in materials applications has been revolutionary in recent years. They are being increasingly utilized in numerous fields, including both military and commercial aerospace applications, as well as the sporting goods and chemical industries [2]. Fiber-reinforced composite materials consist of fibres of high strength and modulus embedded in or bonded to a matrix with distinct interfaces between them. Generally, fibres are the principal load-carrying members, whereas the surrounding matrix keeps them in the preferred position and orientation, acts as a load transfer medium between them and protects them from environmental damage owing to elevated temperatures and humidity [3]. Laminated composite materials consist of layers of at least two different materials that are bonded together. Lamination is used to combine the best aspects of the constituent layers and bonding material in order to achieve a more useful material [4].

Laminates, like many structures, must have holes to serve various purposes. An obvious purpose is to

accommodate a bolt [4]. Cutting the fastener holes causes local damage and stress concentrations, and leads to a loss of structural strength. For the design of composite joints with fastener holes, therefore, failure analyses around the fastener holes are critical [5]. A structural joint represents a critical element in the step of the design. In all cases, a significant weight penalty is incurred by the presence of joints in composite structures; furthermore, premature failures have been experienced too frequently [6]. A large part of the research that has been done on mechanically fastened joints has been concerned with the experimental determination of the influence of geometric factors on the joint strength [7].

Wu and Hahn [8] examined the bearing properties of mechanically fastened glass-fibre/vinyl-ester composite joints. Two glass composites of different fabrics and lay-ups were fabricated using vacuum-assisted resin-transfer molding (VARTM) and tested using a double-lap joint arrangement. Pakdil et al. [9] determined the influence of preload moments on the failure of glass-epoxy laminated composite single bolted-joints with bolt/hole clearance. In order to observe the effects of bolted-joint geometry and the stacking sequence of laminated plates on the bearing strength and failure mode, parametric analysis was applied, experimentally. Ataş et al. [10] attempted

*Corr. Author's Address: Muğla Sıtkı Koçman University, Faculty of Technology, Dept. of Information Systems Engineering, 48170, Muğla, Turkey. serkan@mu.edu.tr

to achieve failure load and modes of laminated glass-polyester composite plates using two parallel circular holes, which were exposed to traction forces by two rigid pins. The behaviours of pin-loaded composite plates were observed both experimentally and numerically with different geometries and fibre orientations. Sen and Sayman [11] performed an experimental failure analysis with two serial bolted composite plates. The composite plates were produced from eighth laminas and glass fibres were used as reinforcement material with an epoxy matrix. The effects of the material parameters and design parameters were considered.

Sen et al. [12] investigated the improvement of an artificial neural network (ANN) method for the prediction of bearing strength of two serial pinned/bolted E-glass reinforced epoxy composite joints. Comparisons of ANN results with desired values showed that there is a good agreement between input and output variables of the experimental data. Chakraborty [13] performed an ANN model-based delamination prediction in laminated composites. It was determined that neural networks were capable of learning the information regarding embedded delamination in a fibre-reinforced plastic laminate. Li et al. [14] used two-dimensional FEM analysis for deterministic progressive failure analysis. Three groups of failure criteria, three sets of degradation rules and two kinds of shear relationship are employed for progressive damage analysis to predict the mean, the coefficient of variation (COV), and the cumulative distribution function (CDF) of its bearing strength.

In this study, a new approach was performed to predict failure loads of cross-ply laminated double-serial mechanically fastened composites via a fuzzy expert system. Computational experiments were carried out to predict the behaviour of cross-ply laminated two serial mechanically fastened composites by using both a fuzzy expert system and regression analysis methods. The performance of both methods was discussed in terms of coefficients of determination, mean absolute deviations, and mean absolute percent deviations.

1 MECHANICALLY FASTENED COMPOSITE JOINT

All specifics of the analysed cross-ply composite materials used for this study and the experimental technique were presented in the preceding study by Sen [15]. In brief, rectangular laminated composite specimens manufactured with epoxy and glass fibres with two serial circular holes, and two rigid pins/bolts were used during experiments. The diameter

of each hole (D) was set as 5 mm. The outer hole was positioned along the centerline of the plate at a distance E from one end of the specimen. The inner hole was placed at a distance K from the centre point of the outer hole. As a result, the edge distance-to-hole diameter ratio (E/D) was as 1, 2, 3, 4 and 5. The plate width-to-hole diameter ratio (W/D) was set as 2, 3, 4 and 5. The distance between two serial holes-to-hole diameter ratio (K/D) was as 3, 4 and 5. The total size ($L+K+E$) of each specimen was 135 mm. The dimension of a specimen is plotted in Fig. 1. Laminated composite specimens were produced from eight unidirectional laminas for arranged stacking sequences as $[0/0/90/90]_s$. A uniform tensile load P was applied to the specimens via rigid pins/bolts.

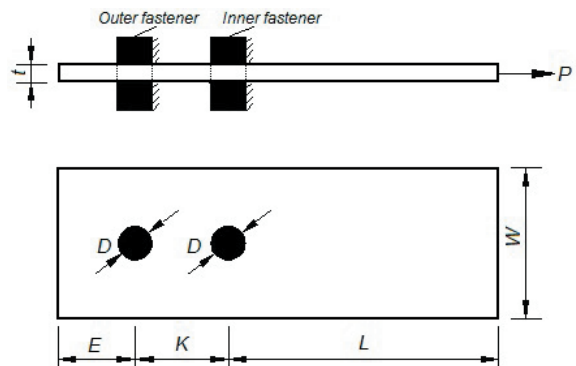


Fig. 1. Dimensions of a laminated composite plate with two serial fasteners

2 FUZZY LOGIC AND FUZZY EXPERT SYSTEM

In daily life, people rely on their common sense and use many ambiguous and unclear linguistic terms. The fuzzy set approach can be utilized to represent linguistic terms in the form of numbers [16]. In general, fuzzy sets used to show uncertain information or the structure of a preference were developed by Zadeh [17]. Fuzzy data enable more flexible presentation; with the use of fuzzy data, more sensitive results can be obtained [18]. For each criterion and alternative, the decision maker can use linguistic descriptors such as good, better or small, very small, etc. depending on his/her preferences [19]. Fuzzy presentation of these linguistic terms is determined according to membership functions. Though there are different types of membership functions used, the most commonly used ones are sigmoid and triangular types, which are presented in Figs. 2 and 3, respectively [20]. For individuals analysed according to determined membership functions, membership values for the

given criterion are obtained between the ranges of [0, 1].

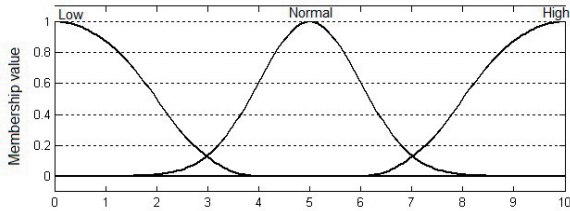


Fig. 2. Sigmoid membership function

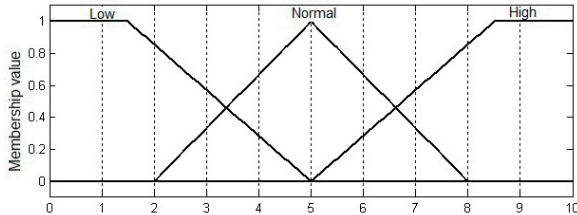


Fig. 3. Triangular membership function

Fuzzy expert systems developed based on fuzzy logic perform reasoning by using numerical operations rather than symbolic reasoning, so they are differentiated from traditional expert systems [21]. With the use of fuzzy logic in expert systems, effectiveness is increased, and response time is decreased [22].

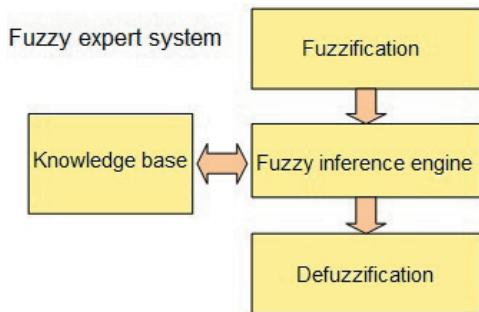


Fig. 4. Structure of fuzzy expert system

As shown in Fig. 4, a fuzzy expert system consists of fuzzification, a knowledge base, a fuzzy inference engine and defuzzification components [23]. The functioning of these components is summarized below:

Fuzzification: Input values are converted into fuzzy values depending on the determined membership function.

Knowledge Base: This is constructed with expert knowledge in application field. The relationships and rules between the input and output values are determined.

Fuzzy inference engine: In light of expert knowledge-based rules, inferences are made from the available information. One of the most widely used methods of inference is Mamdani-style inference [24] because it is more intuitive and closer to human behaviour. In Mamdani-style inference, the existing rules are combined by exposing them to Max-Min operation.

Defuzzification: The operation performed to convert fuzzy information into a particular value is called defuzzification [25]. There are many defuzzification methods, e.g. centroid method, weighted mean method, etc. [20]. In cases in which the membership function is single, the weighted mean method is preferred as it is less complex and easier to calculate in comparison to other methods [26]. It is calculated according to the following equation:

$$u_c = \frac{\sum_i \mu_F(u_i) \times u_i}{\sum_i \mu_F(u_i)}, \quad (1)$$

where u_i represents membership value of the i^{th} element and u_c represents outcome value.

3 RESULTS

In this study, the results of previous experimental study [15] that were obtained for cross-ply laminated composite plates mechanically fastened with two serial pins or bolts were used. For the 5 parameters mentioned in Section 2 and concerning the 300 data points, descriptive statistics are presented in Table 1.

Table 1. Descriptive statistics

	Mean	Standard deviation	Min	Max	Range
M [Nm]	2.80	1.72	0	5	5
W/D [mm/mm]	3.50	1.12	2	5	3
E/D [mm/mm]	3	1.42	1	5	4
K/D [mm/mm]	4	0.82	3	5	2
F [N]	5447	1794	2108	9471	7364

The parameters are linear dependent [27] and the data were analysed according to traditional linear regression analysis and fuzzy expert system methods.

Calculated regression function:

$$F = -810 + 481M + 995W/D + 340E/D + 103K/D$$

Error distribution graph for regression estimate is presented in Fig. 5. The performance of the regression analysis is given in Fig. 6.

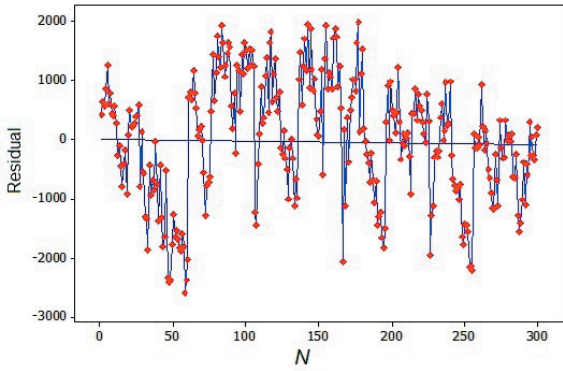


Fig. 5. Error distribution of regression estimate

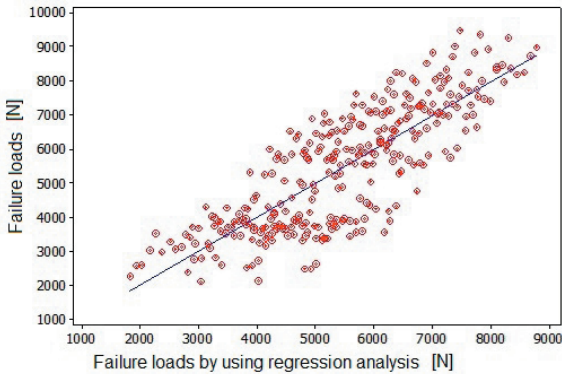


Fig. 6. Performance of regression estimate

Fuzzification of the data for the fuzzy expert system was performed in line with the membership function shown in Fig. 7. Membership values are in the range of [0,1]. There are three different fuzzy sets: low, medium and high. For the output value F , the membership function is given in Fig. 8. There are five different fuzzy sets for F .

The values for parameters were determined by considering membership functions. These values were expressed in linguistic terms and then entered into the knowledge database, and 10 sample values selected out of 300 values are presented in Table 2.

In line with the data collected thus far, an evaluation model in Matlab environment was constructed as shown in Fig. 9 by using expertise and information for reasoning and inference.

As the fuzzy inference engine consists of four criteria and three fuzzy sets belonging to each criterion, it consists of 34 rules. The rules are constructed in line with expert knowledge and experience. In general, the weights of all rules are equal but particular weight can be attached to specific F rules determined according to the expert.

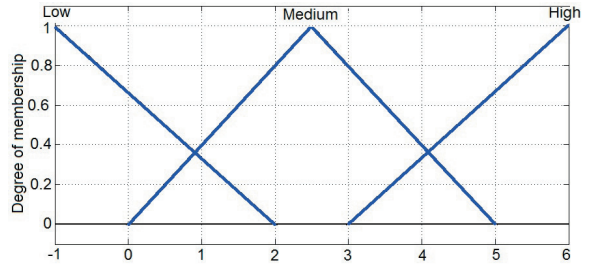


Fig. 7. Membership function for $M, W/D, E/D$

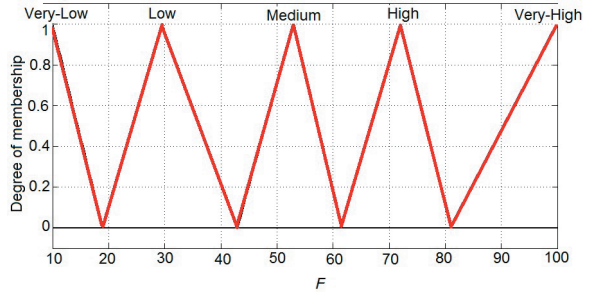
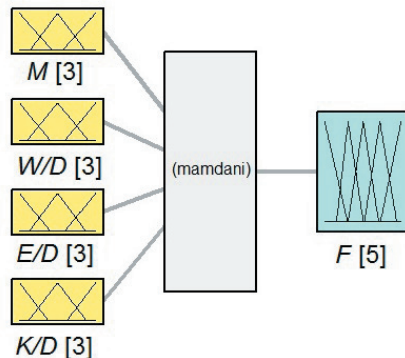


Fig. 8. Membership function for F

Table 2. Linguistic fuzzy values for the parameters

M	W/D	E/D	K/D
Low	High	Medium	Low
Medium	Low	High	Medium
High	Medium	Low	High
Low	Low	High	Medium
High	High	Medium	Low
High	Low	Low	Medium
Medium	Low	Medium	Medium
Medium	Medium	Medium	Medium
Low	Medium	Medium	Medium
Medium	High	High	High



System model: 4 inputs, 1 output, 81 rules

Fig. 9. Fuzzy expert system

Some of these rules are:

IF (M is Low) and (W/D is Low) and (E/D is Low) and (K/D is Low) then (F is Very-Low),

IF (M is Low) and (W/D is Medium) and (E/D is Low) and (K/D is Medium) then (F is Low),

IF (M is Low) and (W/D is High) and (E/D is Low) and (K/D is High) then (F is Medium),

IF (M is High) and (W/D is Medium) and (E/D is High) and (K/D is Medium) then (F is High),

IF (M is High) and (W/D is High) and (E/D is High) and (K/D is High) then (F is Very-High).

The rules are constituted by linguistic values. The F value changes depending on other parameter's status when they are examined. In Figs. 10 to 21, rule surfaces showing three-dimensional input-output relationship for F corresponding to the parameters according to all the rules are presented.

In Fig. 22, the error distribution graph for predictions made according to fuzzy expert system is given. In Fig. 23, the performance graph of fuzzy expert system is seen.

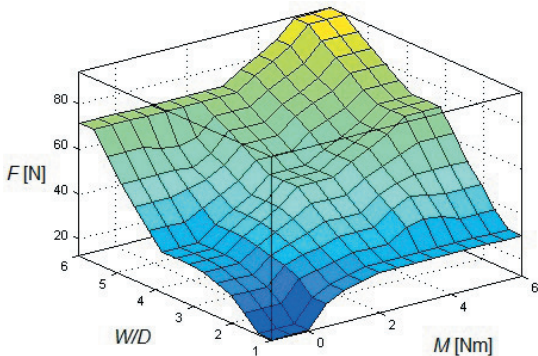


Fig. 10. Surface plot of F and M ; W/D

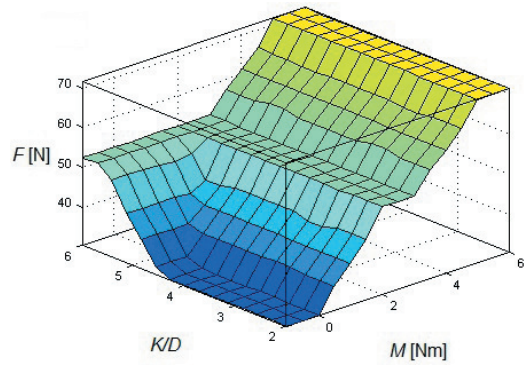


Fig. 12. Surface plot of F and M ; K/D

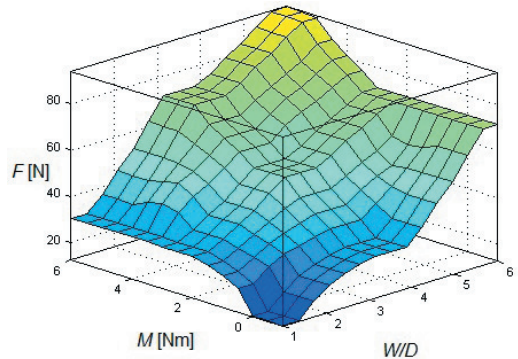


Fig. 13. Surface plot of F and W/D ; M

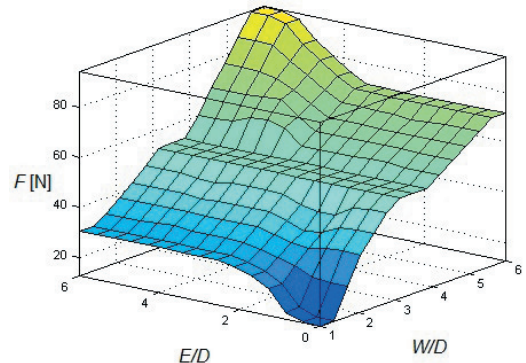


Fig. 14. Surface plot of F and W/D ; E/D

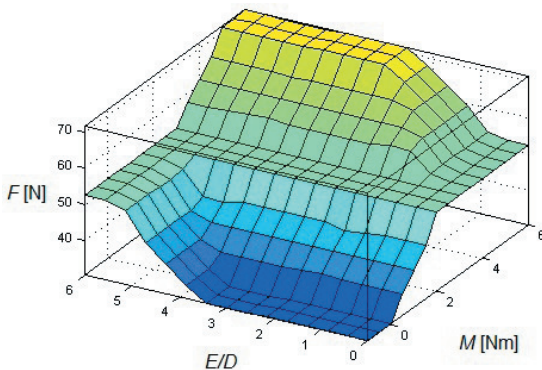


Fig. 11. Surface Plot of F and M ; E/D

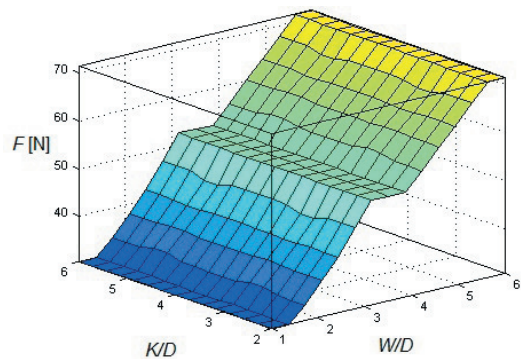


Fig. 15. Surface plot of F and W/D ; K/D

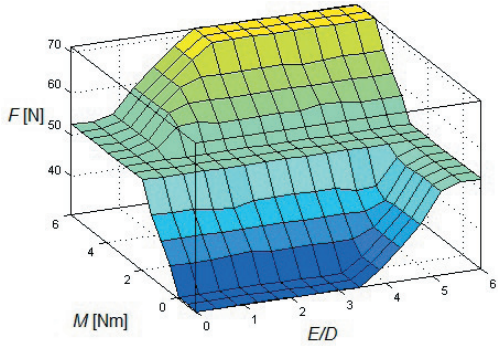


Fig. 16. Surface plot of F and $E/D;M$

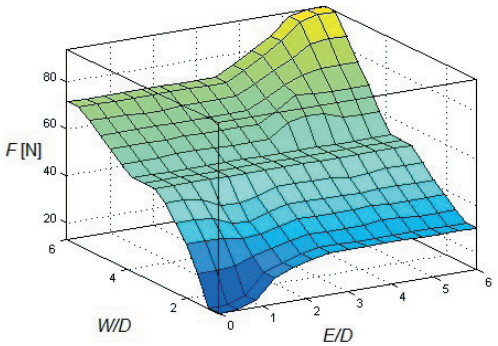


Fig. 17. Surface plot of F and $E/D;W/D$

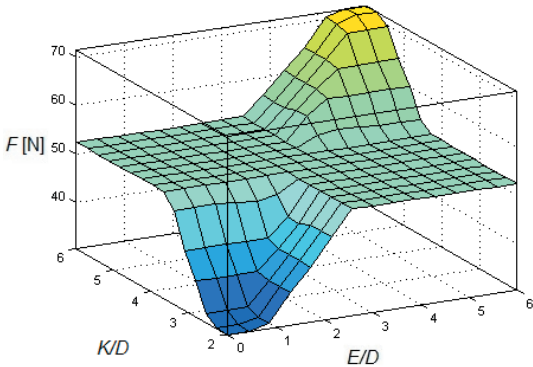


Fig. 18. Surface plot of F and $E/D;K/D$

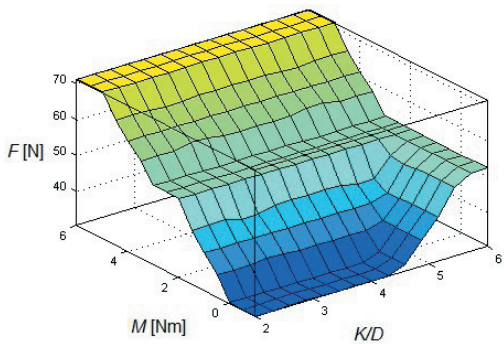


Fig. 19. Surface plot of F and $K/D;M$

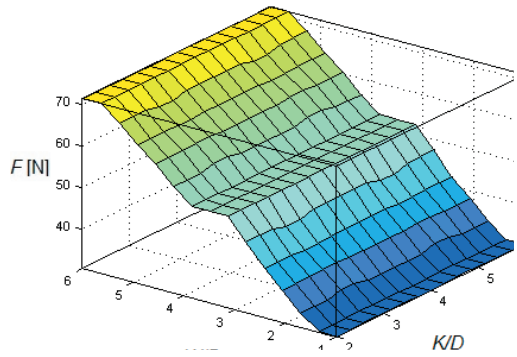


Fig. 20. Surface Plot of F and $K/D;W/D$

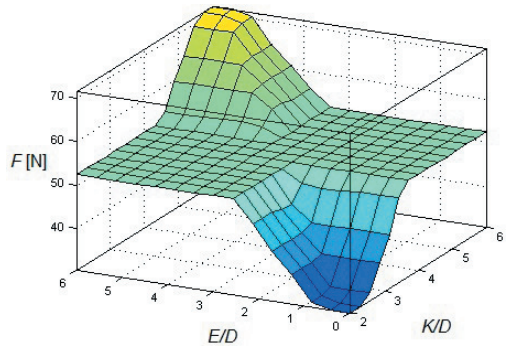


Fig. 21. Surface plot of F and $K/D;E/D$

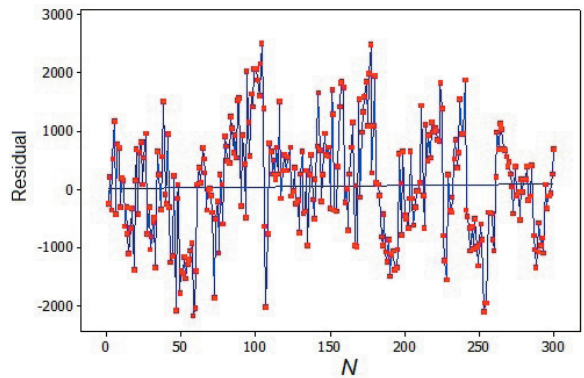


Fig. 22. Error distribution for fuzzy expert system prediction

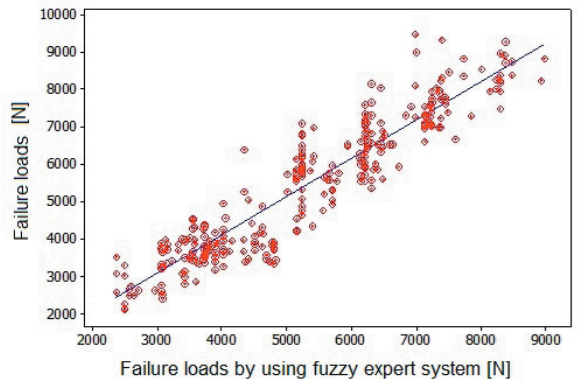


Fig. 23. Fuzzy expert system performance

For the evaluation of the performance of both methods, the statistical parameters are presented in Table 3. These parameters are the coefficient of determination (R^2), mean absolute deviation (MAD) and mean absolute percent deviation (MAPD) .

Table 3. Regression analysis and fuzzy expert system comparison

	MAD	MAPD [%]	R^2
Regression analysis	827.89	15.19	0.67
Fuzzy expert system	525.25	9.64	0.87

MAD and MAPD values of the fuzzy expert system are lower than that of the regression analysis. This means that fuzzy expert system can model the problem well, and that its error of prediction is small. The coefficient of determination for fuzzy expert system is 0.87. It is higher than that of the regression analysis and shows the closeness of predictions to the expected values is good.

4 CONCLUSIONS

In this study, a model was developed for prediction of failure loads for cross-ply laminated composite plates by using fuzzy expert system and regression analysis methods. Computational experiments were carried out to evaluate the performance of both methods. It was seen that the fuzzy expert system clearly made more efficient predictions than the regression analysis method for failure loads. The regression analysis method needs additional parameters to make better predictions in uncertain environments. The fuzzy expert system is more appropriate for the modelling of nonlinear problems and expressing uncertainty than the regression analysis method is.

This study indicates that the prediction of failure loads using fuzzy expert system is suitable for composite materials. The advantage of the present numerical study is that there are no waste materials compared to previous experimental studies. In addition, it is known that experimental studies are more expensive and need longer times for processing than computational studies.

5 ACKNOWLEDGEMENTS

The research is supported by Muğla Sıtkı Koçman University, Turkey, BAP 2013/59.

6 REFERENCES

- [1] Staab, G.H. (1999). *Laminar Composites, 1th ed.* Butterworth-Heinemann, Woburn, Massachusetts.
- [2] Swanson, S.R. (1997). *Introduction to Design and Analysis with Advanced Composite Materials.* Prentice Hall, New Jersey.
- [3] Mallick, P.K. (1993). *Fiber-Reinforced Composites Materials, Manufacturing, and Design, 2nd ed.* Marcel Dekker, New York.
- [4] Jones, R.M. (1999). *Mechanics of Composite Materials, 2th ed.* Taylor & Francis, Philadelphia.
- [5] Ahn, H.S., Kweon, J.H., Choi, J.H. (2005). Failure of unidirectional-woven composite laminated pin-loaded joints. *Journal of Reinforced Plastics and Composites*, vol. 24, no. 7, p. 735-752, DOI:10.1177/0731684405046611.
- [6] Okutan, B. (2002). The effects of geometric parameters on the failure strength for pin-loaded multi-directional fiber-glass reinforced epoxy laminate. *Composites Part B: Engineering*, vol. 33, no. 8, p. 567-578, DOI:10.1016/S1359-8368(02)00054-9.
- [7] Camanho, P.P., Matthews, F.L. (1997). Stress analysis and strength prediction of mechanically fastened joints in FRP: a review. *Composites Part A: Applied Science and Manufacturing*, vol. 28, no. 6, p. 529-547, DOI:10.1016/S1359-835X(97)00004-3.
- [8] Wu, T.J., Hahn, H.T. (1998). The bearing strength of e-glass/vinyl-ester composites fabricated by vartm. *Composites Science and Technology*, vol. 58, no. 9, p. 1519-1529, DOI:10.1016/S0266-3538(97)00180-2.
- [9] Pakdil, M., Sen, F., Sayman, O., Benli, S. (2007). The effect of preload on failure response of glass-epoxy laminated composite bolted-joints with clearance. *Journal of Reinforced Plastics and Composites*, vol. 26, no. 12, p. 1239-1252, DOI:10.1177/0731684407079769.
- [10] Atas, A., Sen, F., Arslan, N. (2009). Failure analysis of laminated composite plates with two parallel pin-loaded holes. *Journal of Reinforced Plastics and Composites*, vol. 28, no. 10, p. 1265-1276, DOI:10.1177/0731684408089493.
- [11] Sen, F., Sayman, O. (2009). Experimental failure analysis of two serial bolted composite plates. *Journal of Applied Polymer Science*, vol. 113, no. 1, p. 502-515, DOI:10.1002/app.30118.
- [12] Sen, F., Komur, A., Sayman, O. (2010). Prediction of bearing strength of two serial pinned/bolted composite joints using artificial neural networks. *Journal of Composite Materials*, vol. 44, no. 11, p. 1365-1377, DOI:10.1177/0021998309353344.
- [13] Chakraborty, D. (2005). Artificial neural network based delamination prediction in laminated composites. *Materials and Design*, vol. 26, no. 1, p. 1-7, DOI:10.1016/j.matdes.2004.04.008.
- [14] Li, H.S., Xia, S., Luo, D.M. (2014). A probabilistic analysis for pin joint bearing strength in composite laminates using subset simulation. *Composites Part B: Engineering*, vol. 56, p. 780-789, DOI:10.1016/j.compositesb.2013.09.025.
- [15] Sen, F. (2007). *Failure Analysis of Composite Pin-Loaded Joints under Preload Moments*, PhD Thesis, Dokuz Eylül University, Izmir.
- [16] Radojevic, D., Petrovic, S. (1997). A fuzzy approach to preference structure in multicriteria ranking. *International Transactions in Operational Research*, vol. 4, no. 5-6, p. 419-430, DOI:10.1016/S0969-6016(97)87512-0.
- [17] Zadeh, L.A. (1965). Fuzzy Sets. *Information Control*, vol. 8, no. 3, p. 338-353.

- [18] Lin, H.Y., Hsu, P.Y., Sheen, G.J. (2007). A fuzzy-based decision-making procedure for data warehouse system selection. *Expert Systems with Applications*, vol. 32, no. 3, p. 939-953, DOI:10.1016/j.eswa.2006.01.031.
- [19] Pedrycz, W., Gomide, F. (1998). *An Introduction to Fuzzy Sets: Analysis and Design*. MIT Press, Cambridge.
- [20] Klir, G.J., Yuan, B. (1995). *Fuzzy Sets and Fuzzy Logic: Theory and Application*. Prentice Hall, New Jersey.
- [21] Zadeh, L.A. (1983). The role of fuzzy logic in the management of uncertainty in expert systems. *Fuzzy Sets and Systems*, vol. 11, no. 1-3, p. 197-198, DOI:10.1016/S0165-0114(83)80081-5.
- [22] Zimmermann, J.-H. (1996). *Fuzzy Set Theory- and Its Applications*. 3rd ed. Kluwer Academic Publishers, Norwell, Massachusetts, DOI:10.1007/978-94-015-8702-0.
- [23] Dweiri, F.T., Kablan, M.M. (2006). Using fuzzy decision making for the evaluation of the project management internal efficiency. *Decision Support Systems*, vol. 42, no. 2, p. 712-726, DOI:10.1016/j.dss.2005.04.001.
- [24] Keshwani, D.R., Jones, D.D., Meyer G.E., Brand, R.M. (2008). Rule-based mamdani-type fuzzy modeling of skin permeability. *Applied Soft Computing*, vol. 8, no. 1, p. 285-294, DOI:10.1016/j.asoc.2007.01.007.
- [25] Şen, Z. (2004). *Fuzzy logic modeling principles in engineering*, Water Foundation Press, Istanbul. (in Turkish)
- [26] Siler, W., Buckley, J.J. (2004). *Fuzzy Expert Systems and Fuzzy Reasoning*, John Wiley & Sons, Hoboken, DOI:10.1002/0471698504.
- [27] Camanho, P.P., Lambert, M. (2006). A design methodology for mechanically fastened joints in laminated composite materials. *Composites Science and Technology*, vol. 66, no. 15, p. 3004-3020, DOI:10.1016/j.compscitech.2006.02.017.

Effect of Initial Residual Stress and Machining-Induced Residual Stress on the Deformation of Aluminium Alloy Plate

Xiaoming Huang¹ – Jie Sun^{1,2,*} – Jianfeng Li^{1,2}

¹ Shandong University, School of Mechanical Engineering, China

² Ministry of Education, Key Laboratory of High Efficiency and Clean Mechanical Manufacture, China

During the machining of aerospace thin-walled components, a large amount material is removed, and machining-induced residual stress is induced in the boundary layer of the work piece, which results in deformation of the components. In this study, the effects of material initial residual stress and machining-induced residual stress on the deformation of aluminium alloy plate are studied. A theoretical model of the plate is analysed first, and the experiments of the milling deformation under different initial residual stress conditions are performed. The results show that the machining-induced residual stress is the primary factor of distortion. The coupling action of compressive initial residual stress and machining-induced residual stress increase the plate deformation, and the coupling action of tensile initial residual stress and machining-induced residual stress decrease the plate deformation. The finite element simulation results are compared with experimental results and found to be in good agreement.

Keywords: thin walls, machining distortion, residual stress, chemical milling

Highlights

- Machining deformation mechanism of plate was studied.
- Analysis of deformation factors weights.
- The effect of the plate initial residual stress on the magnitude of the deformation.
- Studied the relationships between the maximum deflection and the thickness of the specimens.

0 INTRODUCTION

With increasing demand for the improvement of airplane performance, large monolithic components are widely used in order to reduce airplane weight in the aviation industry [1]. During the machining process of structural components, up to 90% of the material is removed from the blank. For those components, it is easy to cause substantial distortion because of the initial residual stress and machining-induced residual stress.

Aircraft parts are typically machined from pre-stretched 7050-T7451 aluminium alloys. In order to reduce the initial residual stresses and increase mechanical strength, pre-treatments are performed in producing blank plates, i.e. quenching, extrusions, stretching, etc. [2] and [3]. However, it is difficult to eliminate the initial stress. Machining-induced residual stress is produced on the machined surface of the work piece due to the action of machining.

In order to control the thin-walled component deformation, some investigations have been done. Rai and Xirouchakis studied the milling thin-walled component distortion based on an FEM machining environment [4]. An FEM method called “house-building frame modelling” was used to predict the milling distortion of monolithic aero-component

under different milling conditions [5]. For this study, machining loads were used to replace the machining-induced residual stresses, and initial residual stresses were ignored. This assumption is inappropriate for the actual situation.

Assuming that stresses induced by the machining process were negligible, Sun and Ke studied the influence of initial residual stress on the machining distortion of large unitization airframes [6]. Huang et al. investigated the effects of the milling process sequence on the deformation of frame monolithic components by establishing cutting force fields and temperature fields [7]. Moreover, some studies on monolithic component deformation were focussed on surface dimensional error caused by machining load and clamping force [8] and [9].

Although some studies have been done to analyse the machining distortion, there is a lack of comprehensive studies on the cause and primary effect element of machining distortion of thin-walled components. The joint action of initial residual stress and machining-induced residual stresses on thin-walled component deformation has not been fully explored, and fundamental research is required to understand how machining distortion develops.

In this paper, machining residual stress is induced by the high-speed milling thin-walled plates of

*Corr. Author's Address: Shandong University, School of Mechanical Engineering, No.17923 Jingshi Road, China, hxm2552@163.com

different locations in 60 mm thick 7050-T7451 plates, which are used to explore the effect of machining-induced residual stress and blank initial residual stress for deformation. In order to avoid introducing additional stress, chemical milling experiments are conducted to thin the specimens gradually.

1 THEORETICAL ANALYSIS MODEL

For a simple rectangular block, there are only longitudinal residual stresses in the transverse directions along the thickness, as shown in Fig. 1. It is assumed that the material is removed without creating residual stresses at the exposed material surface [10]. Because there are no external forces acting on the plate, all forces and bending moment acting over any cross-section of the plate must be in equilibrium before and after the materials were removed:

$$\int \sigma dA = 0, \quad \int dM = 0. \quad (1)$$

The relationship between the moment and curvature change is given by [6]:

$$\frac{1}{\rho_m} - \frac{1}{\rho_{m+1}} = \frac{6\delta\delta_m\sigma_{j1}}{E(\delta_{m+1})^3}, \quad (2)$$

where, ρ_m/ρ_{m+1} are radii of curvatures of the mid-section of the remaining body, before and after removal of the m th layer; δ is the thickness of the removed layer; δ_m and δ_{m+1} are the height of the body before and after the removal of the m th layer; E is Young's modulus, and σ_{j1} is the residual stress of the m th layer before it is removed.

Since the distribution of the residual stress in the remaining body is changed due to the removal of the m th layer, the curvature change resulting from the removal of the $(m+1)$ th layer will be a function of the new state of residual stress as opposed to the original state of residual stress.

The shaded triangle shown in Fig. 1 represents the stress state in the block that is created by bringing the remaining body back to its equilibrium state.

$$\sigma_{j1}\delta + \frac{h_{um}S_m}{2} + \frac{h_{lm}S'_m}{2} = 0, \quad j = m - 1, \quad (3)$$

where, h_{um} and h_{lm} are the height from the neutral axis to the upper and bottom surface of the remaining body, S_m and S'_m are stresses that are produced at the upper and bottom surfaces of the remaining body.

The relationship between the stress S_m and the curvature change caused by the removal of the m th layer can be expressed as:

$$S_m = h_{um}E\left(\frac{1}{\rho_m} - \frac{1}{\rho_{m+1}}\right). \quad (4)$$

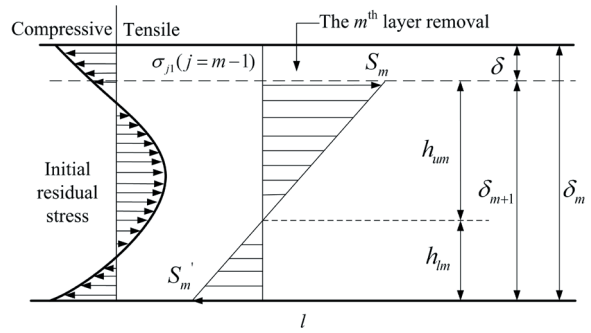


Fig. 1. Initial residual stress and additional stresses after the removal of materials

Referring to Fig. 1,

$$h_{um} + h_{lm} = \delta_{m+1}, \quad (5)$$

$$S'_m = (h_{lm} / h_{um}) S_m, \quad (6)$$

Utilizing Eqs. (2) through (6),

$$h_{um} = \frac{\delta_{m+1}(3\delta_m + \delta_{m+1})}{6\delta_m}. \quad (7)$$

In order to compute the stress σ_{j1} , the correction terms accounting for the removals of the first layer through the m th layer should be calculated. For computing the correction terms, the stress, S_k for $1 < k < j$, which would be produced by bringing back the remaining body after the removal of the k th layer, should be first determined.

$$\begin{aligned} \sigma_{11} &= \sigma_2 - S_{11}, \\ \sigma_{21} &= \sigma_3 - (S_{12} + S_{22}), \\ \sigma_{31} &= \sigma_4 - (S_{13} + S_{23} + S_{33}), \\ &\vdots \end{aligned} \quad (8)$$

In general, Eq. (8) can be written as:

$$\sigma_{j1} = \sigma_{j+1} - \sum_{m=1}^j S_{mj}. \quad (9)$$

In the actual milling process, machining-induced residual stresses are brought to the new surface of the work piece, which affect the deformation of the thin-walled plate coupling with the initial residual stress. The closed-form solutions developed in this section for computing the curvature of the known original residual stress can be solved with Matlab software.

2 EXPERIMENTS

2.1 Experiment Specimens

The investigation is performed on 7050-T7451 alloy. The mechanical properties of the material are shown in Table 1.

Table 1. Mechanical properties of 7050-T7451

Modulus of Elasticity	Tensile Yield Strength	Shear Strength	Density
71.7 GPa	469 MPa	303 MPa	2.83 g/mm ³

Four specimens of altered position in the 60 mm thickness 7050-T7451 aluminium sheet are studied. Specimen position is shown in the Fig. 2a, and specimen IV is in the middle of the thickness direction. The interval distance is 7 mm, and the plate thickness is 2 mm. The initial residual stress of Specimens I and III are tensile, Specimen II is compressive, and Specimen IV lies in the centre of the blank. The size of the specimen is 140×50×2 mm; the length, width, and height directions are parallel, perpendicular pre-stretched direction and thickness direction.

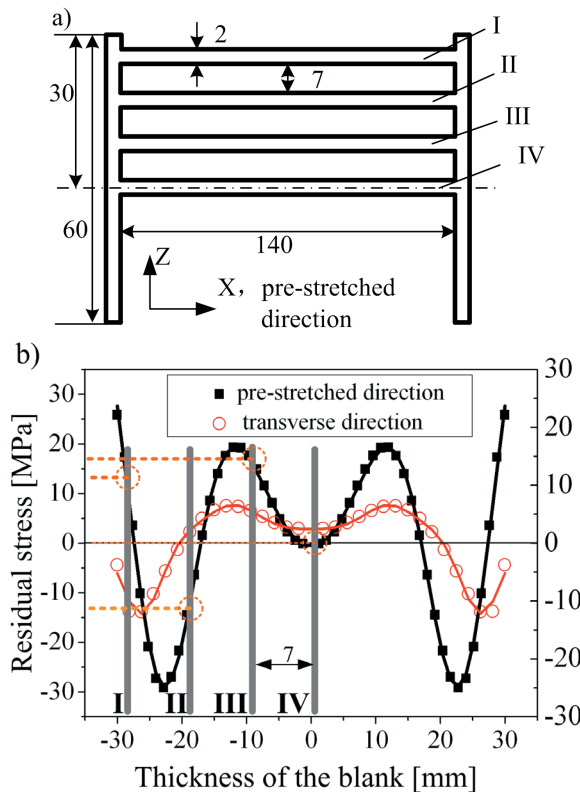


Fig. 2. Specimen position and the initial residual stress profile of 7050-T7451 plate

In order to obtain the initial residual stress profile, a crack-compliance method was used to measure the original residual stress [11]. Fig. 2b shows the initial residual stress distribution profile along thickness direction in the blank.

2.2 Milling Induced Residual Stress

Machining residual stresses are introduced by high-speed milling; the milling test is performed on a DECKEL MAHO DMU 70V five-axis universal machining centre, and the tool used is an end mill without coating. The detailed values of the experimental conditions are presented in Table 2.

Table 2. The experimental conditions

CNC	DECKEL MAHO DMU 70V 5-axis universal machining centre	
Tool	Material	Solid cemented carbide
Machining state	Dry, Down milling	
Machining parameters	v	628 m/min
	f_z	0.06 mm
	a_p	5 mm
	a_e	12 mm

Specimen IV is shown in Fig. 3a; x denotes the perpendicular feed direction.

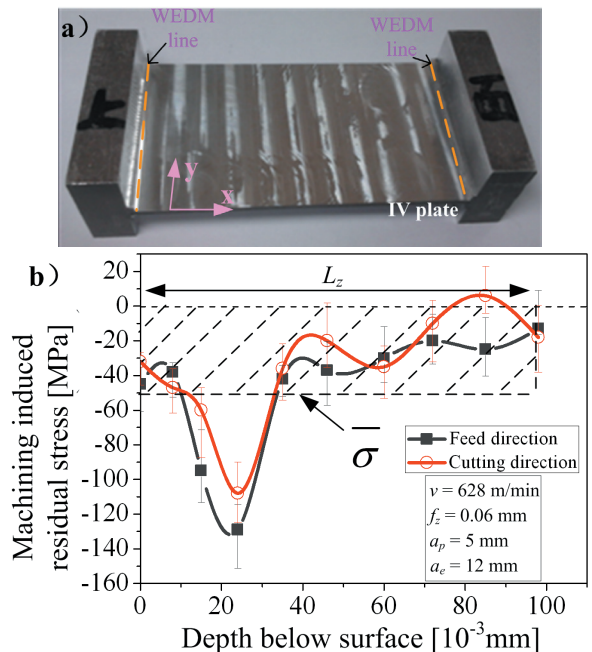


Fig. 3. Specimen and machining-induced residual stresses profiles of 7050-T7451 thin-walled plate

The plates are cut down by wire electrical discharge machining (WEDM), which leaves a heat affected zone (HAZ). The research shows that the HAZ has a thickness of the order of microns [12] and [13], which is much less than the specimen size (140×50 mm). It is assumed that the WEDM induced the residual stress but did not influence the initial residual stress distribution and plate deformation.

The machining-induced residual stress on the surface of the work piece is measured using X-ray diffraction technique and electro-polishing technology [14], which is shown in Fig. 3b.

2.3 Chemical Milling

In order to reduce the introduction of additional stresses, chemical milling is used to remove materials gradually from one side of the plate. The composition and ratio of the chemical milling fluid are shown in Table 3. A chemical milling protective coating (HH968-2) is used to ensure that the machining-induced residual stress is unbroken on one side of the surface.

Table 3. The primary composition and ratio of chemical milling fluid

NaOH(g)	Na ₂ S(g)	TEA(g)	H ₂ O(g)	NaOH(g/L)
175	18	33	678	180

An increasing amount of material is chemically removed from the surface of the four specimens. Specific thicknesses of the plate can be seen in Table 4. Before and after the chemical milling of each specimen, the thicknesses of the thin-walled plates are measured using a micrometer.

Table 4. Incremental chemical milling and plate thickness

Initial thickness [mm]	2	1.75	1.5	1.25	1
Thickness after chemical milling [mm]	1.75	1.5	1.25	1	0.75

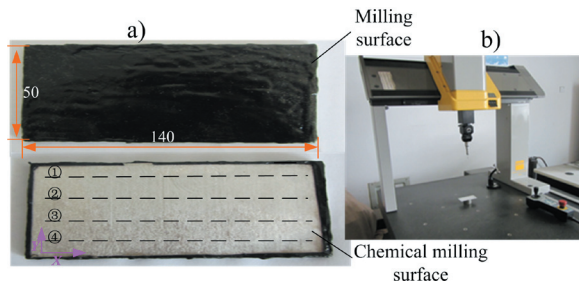


Fig. 4. Chemical milled sample and deformation measurement

The distortion values of characteristic points of machined thin-walled plate are measured using a

MISTRAL 775 3D coordinate-measure-machine, as shown in Fig. 4. Four characteristic lines are setup along the X direction on the chemical milling surface as shown in Fig. 4a, and some characteristic points along the characteristic lines are picked up at intervals.

The distortion values of characteristic points of machined thin-walled plate are measured using a MISTRAL 775 3D coordinate-measure-machine, as shown in Fig. 4. Four characteristic lines are setup along the x direction on the chemical milling surface as shown in Fig. 4a, and some characteristic points along the characteristic lines are picked up at intervals.

3 RESULTS AND DISCUSSION

The deformations are graphed by the average value of the four characteristic lines. The measurements results for a 0.75 mm thickness plate are presented in Fig. 5. It can be seen that the specimens exhibit significant bowing. The thin-walled plates present convex and bending distortions, with the law of symmetric distribution from the middle to two sides. The convex directions of specimens with initial compressive and tensile stress are the same. Machining-induced residual stress results in the machined side facing up.

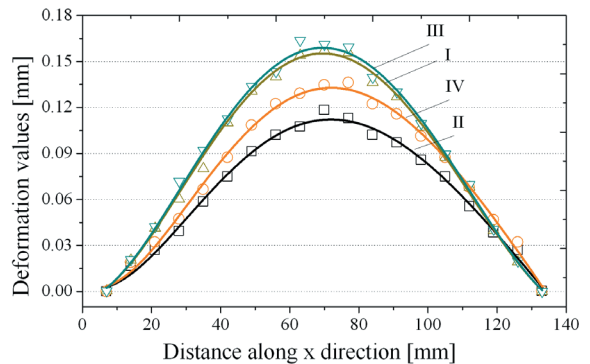


Fig. 5. Specimen deformation of 0.75 mm thickness plate

The deformation degree of the four specimens is shown as: III>I>IV>II. Specimen IV's deformation is considered to be caused by machining-induced residual stress, mostly because of its location and the initial residual stress profile. For Plates I and III, the coupling effect of tensile initial residual stress and machining-induced residual stress increases the deformation compared with Plate IV. For Plate II, the coupling effect of the compressive initial residual stress and the machining-induced residual stress decrease the deformation, in comparison with Plate IV.

The relationships of the maximum deflection and the thickness of the four specimens are shown in Fig. 6. As can be seen, the non-linear deformation increases gradually when the materials are removed from one side. The residual stress has a significant impact on the deformation of plates of different thicknesses. This 1.75 mm plate is 2.3 times the thickness of that 0.75 mm one, and the 0.75 mm plate deformation is approximately 9.8 times that of the 1.75 mm plate deformation. According to the curve of Fig. 6, the curve slopes at different thickness are calculated and listed in Table 5. Deformation differentiation of the four plates is not significant when the thickness is more than 1.5 mm. When the thickness is less than 1.25 mm, the machining-induced residual stress has a greater effect on the plate deformation.

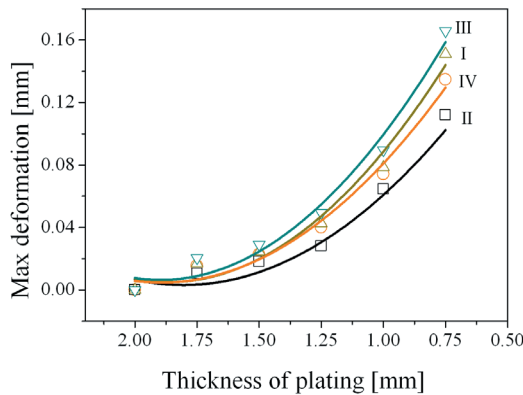


Fig. 6. The relationship of max deformation and thin-walled plate thickness

The max displacements of the four specimens are 0.151, 0.112, 0.165 and 0.134 mm when the thickness is 0.75 mm. The influence of the initial stress on deformation is (0.165–0.112) mm = 0.053 mm, which accounts for about one third of the total deformation. Machining-induced residual stress is the primary effect element of machining distortion for the 0.75 mm thick aluminium alloy plate.

Table 5. Deformation slope at different thicknesses

Plate thickness [mm]	1.75	1.5	1.25	1.0	0.75
I	0.048	0.051	0.010	0.247	0.350
II	0.041	0.045	0.107	0.154	0.213
III	0.057	0.057	0.121	0.277	0.393
IV	0.045	0.048	0.103	0.175	0.218

4 FEM SIMULATION

Finite element simulation of machining distortion is performed using the ABAQUS commercial finite

element software. The size of the thin-walled plate is the same as that of the experimental specimen (140×50×2 mm). The model was meshed with the C3D8R element, with a total of 1120 elements and 1512 nodes.

The residual stress curve from Fig. 2b is dispersed, and the corresponding value of the residual stress at each position was assumed to act uniformly through the thickness of the thin-wall plate, as shown in Fig. 2b. The initial residual stress of every plate is applied to the finite element model using the corresponding node command in FEM.

The arithmetic mean stress ($\bar{\sigma}$) in the machining affected zone (0.1 mm) is obtained in order to characterize the machining-induced residual stress according to the following calculation:

$$\bar{\sigma} = \frac{\int_0^z \sigma dz}{L_z}, \quad (10)$$

where, L_z is the upper limit of integration, which is shown in Fig 3b. The results are computed using Origin 8.0 commercial software.

The machining-induced residual stress data is applied to the milling affected zone. Via the superposition of initial residual stresses and machining-induced stress, combined deformation effects can be determined. The task is to define the complete stress tensor (pre-stretched direction and transverse direction) at each node, and to have it for the complete model in mechanical equilibrium.

The technology of “element birth and death” was used to simulate the chemical milling process in the software, in which the stiffness matrix multiplied by a very small coefficient to deactivate the element (usually it is set to zero); simultaneously, the quality, damp, and specific heat were all set to zero.

For finite element simulation, the thickness was divided into 8 equal layers of 0.25 mm each, with the simulation of the machining process (one removal at a time) representing a 0.25 mm reduction in thickness of the plate.

The 3-2-1 constraint principle was adopted as the boundary conditions, where the rigid motion of the work piece was constrained, but the work piece can be free to distort to reach a new stress equilibrium state.

The deformation nephogram of Plate I at 0.75 mm thickness is shown in Fig. 7a, and the Mises stress redistribution along the thickness direction is shown in Fig. 7b. The distortion law from the finite element simulation accords with the experimental result, which reveals a bending distortion in the middle and warped

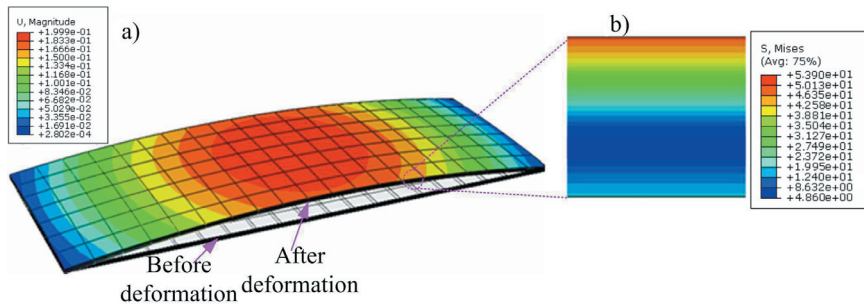


Fig. 7. Deflection and residual stress redistribution of thin-walled plate I (0.75 mm)

at both ends. As can be seen, the max deflection is in the plate central part. The machining-induced residual stress is on the convex surface. The max displacement and Mises stress are 0.199 mm and 53.9 MPa in machining surface.

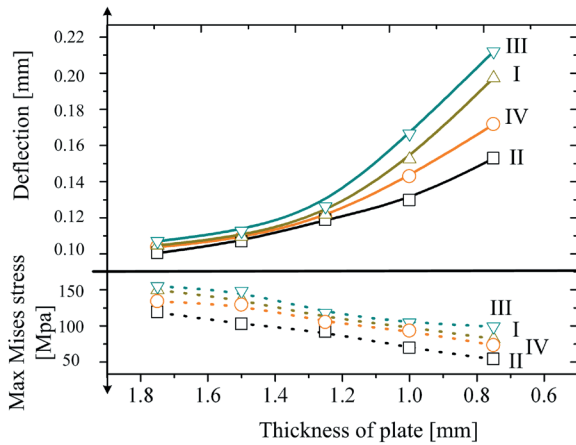


Fig. 8. The maximum deformation and Mises stress of thin-walled plate thickness

The FEM simulation results of maximum Mises stress and the corresponding deformations are shown in Fig. 8. As the materials are removed, the maximum surface Mises linearly decreased, and the maximum deflection nonlinearly increased. Moreover, the finite element simulation and experiment have the same deformation degree: III>I>IV>II. The order of max Mises stress is III>I>IV>II, which is the same as the deflection order.

The maximum deformation of the FEM simulation, as well as analytical and experiments results are shown in Fig. 9. As can be seen, the theoretical calculation result has good agreement with the FEM. The maximum margin of error between FEM and analytical value was 7.9%. The experimental values are less than the FEM results. There are some error factors producing the difference between FEM and experimental results: machining-induced residual

stress has uniform distribution because of the milling tool-path; measurement precision; calculation error, etc. The maximal error is 29.8%, which is in the acceptable range.

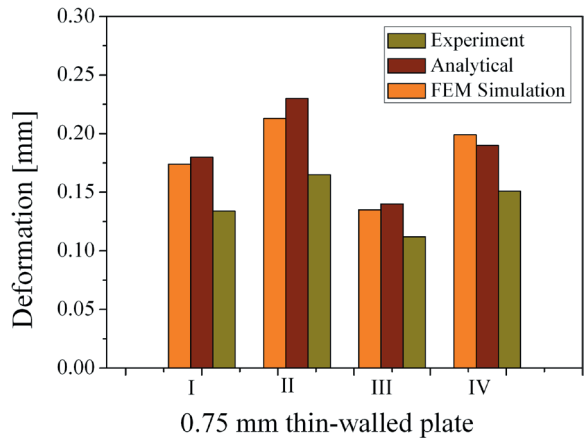


Fig. 9. The max deformation of FEM analytical and experiments results

5 CONCLUSIONS

The effects of material initial residual stresses and machining-induced residual stresses on the deformation of aluminium alloy plate are studied. The thin-walled specimens appeared convex and bending distortion, and machining induced residual stress result in the machined side facing up. The machining-induced residual stress is the primary cause of plate deformation.

The location of the plate has some effect on the magnitude of the deformation. Compared with the near center plate, the deformation is greater when the plate is in the tensile residual stress zone of the blank, and the deformation is lesser when the plates are in the compressive residual stress zone of the blank. The relationships of the maximum deflection and the thickness of the specimens are studied, and the results

show that the machining-induced residual stress has a greater effect on the plate deformation when the thickness is below than 1.25 mm.

The tendency of FEM deformation is consistent with the experiment results, and the values are greater than the measurement values. As the materials are removed, the max Mises stress decreased almost linearly.

6 ACKNOWLEDGEMENTS

The authors want to thank for the support from the National Natural Science Foundation of China (No. 51275277).

7 REFERENCES

- [1] Megson, T.H.G. (2012). *Aircraft Structures for Engineering Students*. Leeds University, Leeds.
- [2] Li, P.Y., Xiong B.Q., Zhang, Y.A., Li, Z.H. (2012). Temperature variation and solution treatment of high strength AA7050. *Transactions of Nonferrous Metals Society of China*, vol. 22, no. 3, p. 546-554, DOI:10.1016/S1003-6326(11)61212-0.
- [3] Burtchen, M., Hunkel, M., Lübber, Th., Hoffmann, F., Zoch, H.-W. (2009). Simulation of Quenching Treatments on Bearing Components. *Strojniški vestnik - Journal of Mechanical Engineering*, vol. 55, no. 3, p. 155-159.
- [4] Rai, J.K., Xirouchakis, P. (2008). Finite element method based machining simulation environment for analyzing part errors induced during milling of thin-walled components. *International Journal of Machine Tools and Manufacture*, vol. 48, no. 6, p. 629-643, DOI:10.1016/j.ijmachtools.2007.11.004.
- [5] Guo, H., Zuo, D.W., Wu, H.B. Xu, F. Tong, G.Q. (2009). Prediction on milling distortion for aero-multi-frame parts. *Materials Science and Engineering A*, vol. 499, no. 1, p. 230-233, DOI:10.1016/j.msea.2007.11.137.
- [6] Sun, J., Ke, Y.L. (2005). Study on machining distortion of unitization airframe due to residual stress. *Chinese Journal of Mechanical Engineering*, vol. 41, no. 2, p. 117-122, DOI:10.3901/JME.2005.02.117. (in Chinese)
- [7] Huang, Z.G., Ke, Y.L., Dong, H.Y. (2005). Finite element model of milling process sequence for frame monolithic components. *Journal of Zhejiang University (Engineering Science)*, vol. 39, no. 3, p. 368-372. (in Chinese)
- [8] Ratchev, S., Huang, W., Liu. S., Becker, A.A. (2004). Modelling and simulation environment for machining of low-rigidity components. *Journal of Materials Processing Technology*, vol. 153-154, p. 67-73, DOI:10.1016/j.jmatprotec.2004.04.301.
- [9] Abdullah, R. (2011). *Hybrid Deflection Prediction for Machining Thin-Wall Titanium Alloy Aerospace Component*, Ph.D. Thesis, RMIT University, Melbourne.
- [10] Shang, H.S. (1995). *Prediction of the Dimensional Instability Resulting from Machining of Residually Stressed Components*, Ph.D. thesis, Texas Tech University, Lubbock.
- [11] Prime, M.B., Hill, M.R. (2002). Residual stress, stress relief and inhomogeneity in aluminum plate. *Scripta Materialia*, vol. 46, no. 1, p. 77-82, DOI:10.1016/S1359-6462(01)01201-5.
- [12] Izquierdo, B., Plaza, S., Sánchez, J.A., Pombo, I., Ortega, N. (2012). Numerical prediction of heat affected layer in the EDM of aeronautical alloys. *Applied Surface Science*, vol. 259, p. 780-790, DOI:10.1016/j.apsusc.2012.07.124.
- [13] Banerjee, S., Prasad, B.V.S.S., Mishra, P.K. (1997) Analysis of three-dimensional transient heat conduction for predicting wire erosion in the wire electrical discharge machining process. *Journal of Materials Processing Technology*, vol. 65, no. 1-3, p. 134-142, DOI:10.1016/0924-0136(95)02253-8.
- [14] Huang, X.M., Sun, J., Li, J.F., Han, X., Xiong, Q.C. (2013). An experimental investigation of residual stresses in high-speed end milling 7050-T7451 Aluminum alloy. *Advances Mechanical Engineering*, vol. 2013, Article ID 592659, DOI:10.1155/2013/592659.

The Mechanical Properties of Moulded and Thermoformed Denture Resins

Sebastian Baloš¹ – Mladimir Milutinović¹ – Michal Potran² – Jelena Vuletić² – Tatjana Puškar² – Tomaž Pepelnjak^{3,*}

¹ University of Novi Sad, Faculty of Technical Sciences, Serbia

² University of Novi Sad, Medical Faculty, Serbia

³ University of Ljubljana, Faculty of Mechanical Engineering, Slovenia

This study describes in detail the mechanical properties of polymethylmethacrylate (PMMA) denture base resins with regard to fabrication procedures, moulding and thermoforming. The investigation included eight specimens of each group of the materials, made separately for each experimental protocol (moulding and thermoforming). Analysis of the mechanical properties of the tested resins was comprised of tensile and 3-point bending strengths, elongation, fracture toughness and micro-hardness tests. Data obtained from the mechanical tests were statistically processed by using one-way analysis of variance (ANOVA) with Tukey's post-hoc test and with the significance level $\alpha=0.05$.

Triplex cold specimens showed the lowest bending strength, fracture toughness and micro-hardness as well the highest standard deviations. Biocryl C in a thermoformed condition exhibited higher tensile and bending strength in comparison to the same material but in the as-received condition (before thermoforming), while the results are opposite for fracture toughness and micro-hardness. Compared to Triplex hot, thermoformed Biocryl C had statistically non-significantly higher values for bending strength and micro-hardness, but significantly lower ones for fracture toughness and tensile strength. In contrast, the lowest dissipation of testing results in all mechanical tests was recorded for Biocryl C fabricated by a thermoforming process, meaning that this material has the highest predictability of the materials tested.

The mechanical properties of thermoformed PMMA materials are comparable to cold and hot polymerized PMMA materials. Standard deviations obtained for thermoformed PMMA material are lower than those obtained with cold and hot polymerized PMMA materials.

Keywords: polymethylmethacrylate denture resin, thermoforming, mechanical properties, denture base

Highlights

- Risk analysis of denture fracture occurrence.
- Proposed a new methodology for fabrication of removable dentures.
- Four different testing procedures of mechanical properties of four different PMMA materials.
- Processed one-way analysis of variance (ANOVA) with Tukey's post-hoc test.
- Review of the materials' (PMMA) characteristics and benefits of a novel PMMA material.

0 INTRODUCTION

Removable dentures are mobile dental (prostheses) that are used for replacing missing teeth in patients with partial or complete edentulism. Since 1940, the primary material for the fabrication of removable dentures has been polymethylmethacrylate [1] to [3]. Since then, much effort has been made in the improvement of characteristics of construction materials, affecting the composition of the materials and the addition of external supplements to increase their resilience [4]. The most commonly used method of strengthening polymethyl-methacrylate (PMMA) is impregnation with rubber (butadiene styrene) and the addition of various types of fibres [5]. Further improvement of mechanical properties of PMMA can also be conducted via microwave irradiation, as well as the addition of nanoparticles [6] to [8]. Better utilization of the materials' potential requires additional examination by the scientific community, because manufacturers are not required to state the full specification of the product, unless the ingredients

of the material that have proven to be potentially harmful. Knowledge about each material and of its characteristics is necessary in order to choose the most suitable material for a given clinical situation.

According to the Hergravesa [9], the fact that 63% of dentures fracture occurs in the first three years of their use remains a problem in current denture applications [10]. Denture fracture usually appears in the midline of the palate (Fig. 1), due to the cyclic shifting between flexion and extension forces that occur during mastication. This was confirmed by the study of Khasawneh and Arab [11], which reported that 61% of fractures occur in the middle of the palate, which was further verified by in vitro studies by Prombonas and Vlissidis [12].

It has been stated that in the case of a mandibular complete denture, the midline stress field is planar, consisting of low intensity compressive forces and low shear stress. At the same time, the corresponding stress field of the maxillary complete denture is characterized by high tensile stresses and high shear stress. This is of particular importance when

fabricating denture bases (Fig. 2) from brittle materials, such as PMMA, which exhibit significantly higher strength in compression than in tension [12].



Fig. 1. The midline fracture of complete denture base

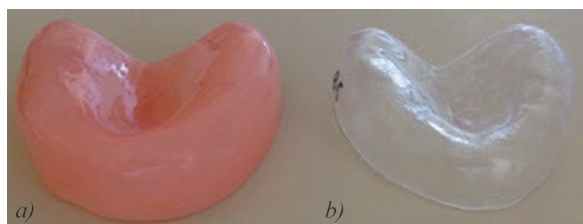


Fig. 2. Models of the denture base fabricated by a) moulding (PMMA - Triplex hot), and b) thermoforming (PMMA - Biocryl C)

This acknowledgement is often discarded in clinical practice, and the selection of a resin material is usually based on its bending strength. Because fracture lines are formed at the sites of internal or external micro-cracks, the tendency to form and propagate initial cracks i.e. fracture toughness, provides additional information for the proper selection of the denture base material. Micro-cracks within the material occur because of residual stresses that are induced during material processing, as well as a result of improper material handling, poor process control and thermal shrinkage [13]. High fracture toughness and crack resistance are prerequisites for minimizing the risk of denture failure due to a fracture. This is why clinical behaviour and the service life of dentures base might significantly differ from its mechanical potential and data given in the literature.

Conventional procedures for the construction of removable dentures include hot- and cold-curing acrylic resins. Because the conversion of monomers into long chains of polymers does not completely occur during the polymerization process, uneven polymerization can result in poor mechanical properties and reduced biocompatibility. Via the process of diffusion, residual monomers can be gradually released into the oral cavity, which can

reduce the material's properties and possibly have a negative impact on health of the oral mucosa. The most common adverse effects are irritation of the oral mucosa and allergic reactions [14] and [15]. Consequently, the development of new materials is mainly focused on reducing the residual monomer content, while improving the ease of handling of the material. In addition, depending on the polymerization process, it is necessary to further standardize the procedures for making removable dentures, so that discrepancies in the material itself are reduced to minimum, which can lead to dentures of high quality.

Due to a complex interaction of various biological and mechanical influences in the oral cavity, predicting the behaviour of the material can be enhanced by correlation of its mechanical properties [16]. Correlation data can be used for detailed examination of resin capabilities as well as to reduce the testing time and cost for each particular resin. In relation to this, the aim of this study was to compare the mechanical properties of acrylic resins depending on the polymerization process, using five different mechanical properties (bending and ultimate tensile strength, elongation, fracture toughness and micro-hardness). A thermoforming material currently not yet used for dentures was selected for comparison with the conventional systems (hot- and cold-curing PMMA). According to the manufacturer, it does not contain residual monomers, and the polymerization process is conducted under strictly controlled conditions [17]. An additional objective was to compare the characteristics of the analysed material before and after the processing by the thermoforming. The obtained results were statistically processed, compared and analysed from different perspectives.

1 MATERIALS AND METHODS

The materials investigated in this study are shown in Table 1. The investigation included eight specimens of each group of the materials, made separately for each experimental protocol.

Materials were treated according to the manufacturers' instructions; a total of 128 specimens were used in this study. All the specimens were kept in distilled water for 7 days before testing, at a constant temperature of 37 °C.

Fabrication of the specimens included the production of wax patterns of an adequate shape that were further invested in gypsum mould. Polymerization of the cold-curing specimens was conducted in a pressure device (Ivomat, Ivoclar Vivadent, Lichtenstain) at 40 °C for 15 minutes under

0.4 MPa pressure. Hot curing specimens were pressed at 7 MPa (Reco Hydromatic press, Germany) after which polymerization was conducted at 100 °C for 45 minutes. Specimens of thermoplastic foil were made by cutting the specimens from the foil with a laboratory handpiece (K5plus, Kavo, Germany) before and after pressure moulding. The foil was pressure moulded on previously constructed gypsum pedestal, at 0.3 MPa in a pressure-moulding device (Ministar S, Scheu Dental, Germany). Specimens were further pre-polished (Abraso-soft acrylic, Bredent, Germany) and additionally polished (High lustre buff acrylic, Bredent, Germany) at 3000 rpm.

Testing procedures for measuring tensile and flexural strength were performed in accordance with ASTM D638 [18] and ISO 20795-1:2013 standards [19]. The tensile strength was determined on a universal testing machine (Model 1122, Instron, USA) with a crosshead speed of 10 mm/min and the following equation:

$$R_m = F_m / S_o, \quad (1)$$

where R_m is the tensile strength [MPa], F_m is the maximum force [N] and S_o is a cross section (mm²). The specimens for the tension test were designed following the ASTM D638 standard (type IV specimen). During loading of the specimen, a force vs. elongation diagram was automatically recorded by the machine plotter. The elongation was calculated as:

$$A = \frac{(L - L_o)}{L_o} \cdot 100 [\%], \quad (2)$$

where L is the fracture length and L_o is the gauge length (25 mm).

Determination of three-point bending strength was done by testing of eight specimens per sample group. Specimen dimensions were: $L \times B \times H =$

$(50 \pm 0.2) \times (6 \pm 0.1) \times (3 \pm 0.1)$ mm. This was done on a universal testing machine (AT-L-118B, Toyoseiki, Japan) with a crosshead speed of 1 mm/min and the distance between the supports of 40 mm. Bending strength was calculated using Eq. (3):

$$\sigma = \frac{3F_{\max} \cdot L}{2B \cdot H^2}, \quad (3)$$

where σ is the bending strength [MPa], F_{\max} is the maximum load [N], L is the distance between supports [mm], B is the width of the specimen [mm] and H is the height of the specimen ($L = 50 \pm 0.2$ mm, $B = 6 \pm 0.1$ mm $H = 3 \pm 0.1$ mm). Fracture toughness was tested using a conventional tensile testing machine (AT-L-118B), equipped with a 4-point bending device with distance between the supports of 20/40 mm. Crosshead speed was kept constant at 1 mm/min. The single edge V-notch beam (SEVNB) method was used according to ASTM D5045, [20] with specimen dimensions of $(45 \pm 0.2) \times (4 \pm 0.1) \times (3 \pm 0.1)$ mm and a notch cut at the longitudinal centre. The preliminary U-notch was machined manually using a precision drill/grinder (FBS12; Proxxon, Germany) with a stroke of 3000 to 15000 min⁻¹ fitted with a $\varnothing 20 \times 0.8$ mm SiC disk. The final V-notch was cut manually into the centre of the U-notch, acting as an initial crack. In order to achieve this, a commercial razor was used (Platinum; Gillette, Boston, Mass). This method has been described previously for ceramic and brittle polymer materials, [21] to [23]. The V-notch depth was measured with a light microscope (Orthoplan; Leitz/Leica, Germany). Fracture toughness was calculated in accordance with Eq. (4):

$$K_{IC} = \frac{F}{B\sqrt{W}} \frac{S_1 - S_2}{W} \frac{3\sqrt{\alpha}}{2(1-\alpha)^{1.5}} Y^*, \quad (4)$$

where F is the maximum force [N], S_1 and S_2 are the distances between the supports [mm], α is the

Table 1. Materials used in the study

Group	Index	Manufacturer	Composition*	Curing method
Triplex Cold	C	Ivoclar Vivadent, Schaan, Liechtenstein	Powder: PMMA, dibenzoyl peroxide, pigments Liquid: MMA, ethylene dimethacrylate, stabilizer	13g: 10 mlM; Chemical polymerization on 40 °C, pressure 0.4 MPa - 15 min
Triplex Hot	H	Ivoclar Vivadent, Schaan, Liechtenstein	Powder: PMMA, dibenzoyl peroxide, pigments Liquid: MMA, ethylene dimethacrylate	23g: 10 ml Heat polymerization on 100 °C - 45 min
Biocryl C (before**)	AR	Scheu Dental, Iserlohn, Germany	polymethylmethacrylat	Prepolymerized by the manufacturer
Biocryl C (after**)	TF	Scheu Dental, Iserlohn, Germany	polymethylmethacrylat	Prepolymerized by the manufacturer, heating 90 s moulding pressure 0.3 MPa

* composition according to the data sheet supplied by the manufacturer

** before and after thermoforming

geometrical factor having the value of a/W , a is the overall notch depth [mm], B is the sample thickness [mm], W is sample width [mm] and Y^* is the specimen geometric function or a geometric factor, which is dimensionless and given as follows:

$$Y^* = 1.9887 - 1.32\alpha - \left(3.49 - 0.68\alpha + 1.35\alpha^2\right)^{\alpha(1-\alpha)(1+\alpha)-2} \quad (5)$$

Micro-hardness was measured using a Vickers micro-hardness tester (HVS-1000; Huayin, China) and the following parameters: 300 g load and 15 s dwell time, according to Balos et al. [24]. Ten indentations were made per each specimen with the following dimensions: diameter 20 mm, thickness 3 mm. Micro-hardness was calculated using Eq. (6):

$$HV = 1.8544 \frac{F}{d^2}, \quad (6)$$

where HV is the Vickers hardness number, F is the load [kg] and d is the average between indentation diagonals [mm].

The mechanical properties were analysed using a one-way analysis of variance (ANOVA) with Tukey's post-hoc test, with the significance level $\alpha = 0.05$. Statistical analysis was performed with Minitab 16 (Minitab Inc., State College, USA) software.

2 RESULTS

The results of mechanical tests performed on selected materials are shown in Figs. 3 to 9, as well as Tables 2 to 6. The typical stress vs. elongation curves are shown in Fig. 3. The highest tensile strength was obtained in specimen group H, followed by C, TH, and AR (Fig. 4 and Table 2). It can be noted that there is a statistical difference between specimen group C and H on one side and AR and TF on the other side. Standard deviations are smaller in sample groups AR and TF.

In Fig. 5, fractured tensile specimens of groups TF and C are shown. It can be seen that fractures occur randomly in the TF group, while in the C specimen group, fractures occur predominantly near the specimens' shoulder. The results of ultimate elongation are shown in Table 3 and Fig. 6. The specimens belonging to the H and TF groups showed similar stretching behaviour (average value of this parameter is almost identical), while a significantly lower value was obtained with specimens from group C.

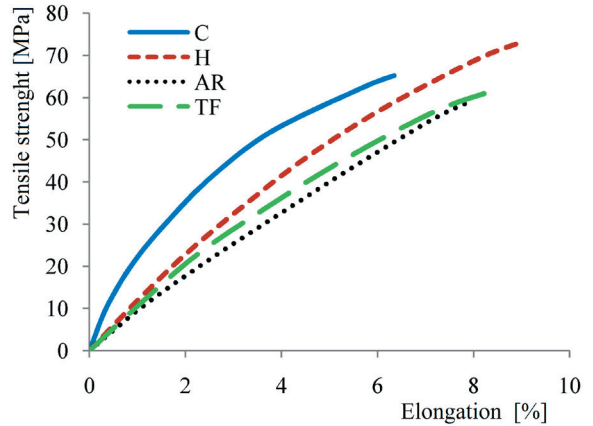


Fig. 3. Typical tensile stress-elongation curves obtained in the tensile test

Table 2. Mean tensile strengths, standard deviations and corresponding statistical parameters

Group	Mean R_m [MPa]	Standard deviation	Grouping*
C	67.94	6.06	A
H	73.46	4.53	A
AR	59.46	3.90	B
TF	60.58	3.69	B

Source	DF	SS	MS	F	P
Factor	3	1299.8	433.3	20.12	0.000
Error	36	775.2	21.5		
Total	39	2075.1			

* different letters indicate statistically significant difference between the results

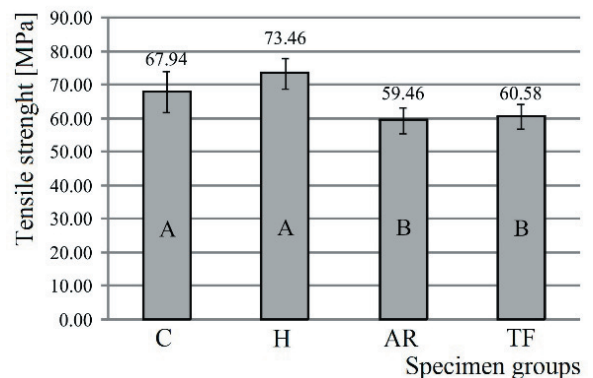


Fig. 4. Graphic of tensile strength of tested materials with standard deviations

Table 4 and Fig. 7 show the results of a 3-point bending test, i.e. flexural strength of tested materials. It can be seen that the highest 3-point bending strength is obtained with TF specimen group, while the lowest for C group. Standard deviation of TF group is the

smallest of all tested groups. However, the statistical analysis proved that the differences between tested groups are not significant.

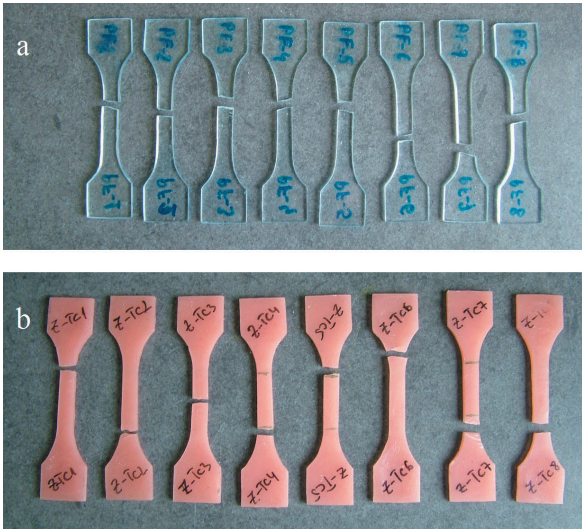


Fig. 5. The location of fractures in tensile testing; a) Biocryl C (after thermoforming), b) Triplex cold

Table 3. Mean elongations, standard deviations and corresponding statistical parameters

Group	Mean A [%]	Standard Deviation	Grouping*
C	6.44	0.74	A
H	8.47	0.80	B
AR	7.88	0.30	B
TF	8.43	0.57	B

Source	DF	SS	MS	F	P
Factor	3	21.668	7.223	17.86	0.000
Error	36	11.326	0.404		
Total	39	32.994			

*different letters indicate statistically significant difference between the results.

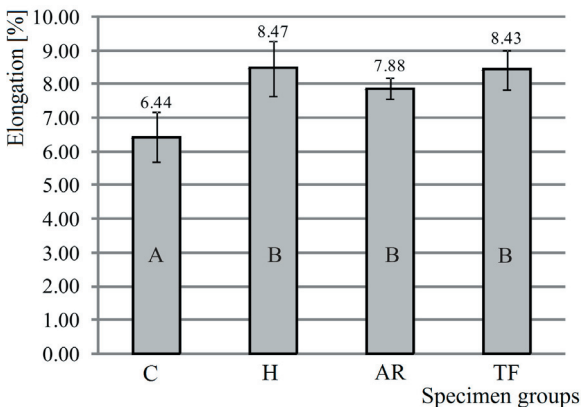


Fig. 6. Elongation of tested materials with standard deviations

Table 4. Mean 3-point bending strengths, standard deviations and corresponding statistical parameters

Group	Mean σ [MPa]	Standard Deviation	Grouping*
C	100.23	10.05	A
H	103.27	9.00	A
AR	102.23	8.33	A
TF	104.88	4.69	A

Source	DF	SS	MS	F	P
Factor	3	113.8	37.9	0.56	0.648
Error	36	2460.0	68.3		
Total	39	2573.9			

*different letters indicate statistically significant difference between the results.

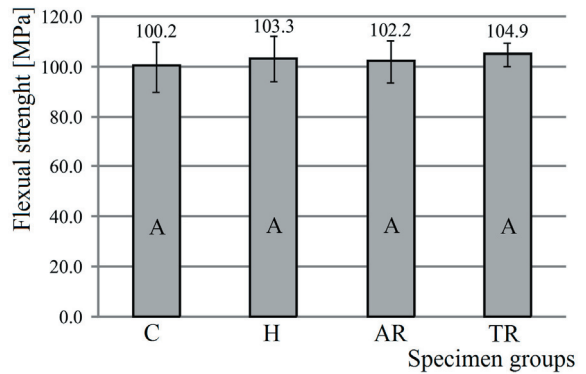


Fig. 7. Graphic of 3-point bending strengths of tested materials with standard deviations

The fracture toughness results are shown in Table 5 and Fig. 8. The difference between the specimen group with the highest and the lowest fracture toughness (C and H group) is significant. Such results are obtained in spite of the lowest standard deviations. Furthermore, it can be noted that the TF specimen group has lower fracture toughness than the AR specimen group.

Table 5. Mean fracture toughnesses, standard deviations and corresponding statistical parameters

Group	Mean K_{IC} [MPam ^{1/2}]	Standard Deviation	Grouping*
C	1.230	0.06	A
H	1.803	0.10	B
AR	1.403	0.09	C
TF	1.236	0.08	A

Source	DF	SS	MS	F	P
Factor	3	2.17068	0.72356	0.72356	0.000
Error	36	0.25506	0.00709	0.00709	
Total	39	2.43574			

*different letters indicate statistically significant difference between the results.

3 DISCUSSION

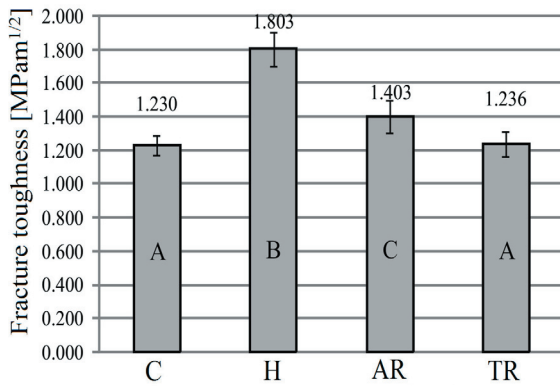


Fig. 8. Fracture toughness of tested materials with standard deviations

In terms of micro-hardness, the highest results were obtained for AR specimen group (Table 6 and Fig. 9). The results demonstrate that the H, AR, and TF specimen groups have a significantly higher micro-hardness compared to the C group. Furthermore, it can be noted that the standard deviation in the C specimen group is higher than in AR and TF group.

Table 6. Mean micro-hardnesses HV0.3, standard deviations and corresponding statistical parameters

Group	Mean HV0.3	Standard Deviation	Grouping*
C	19.66	1.22	A
H	21.65	0.63	B
AR	22.43	0.35	B
TF	21.96	0.31	B

Source	DF	SS	MS	F	P
Factor	3	44.62	14.87	28.22	0.000
Error	36	18.97	0.527		
Total	39	63.59			

*different letters indicate statistically significant difference between the results.

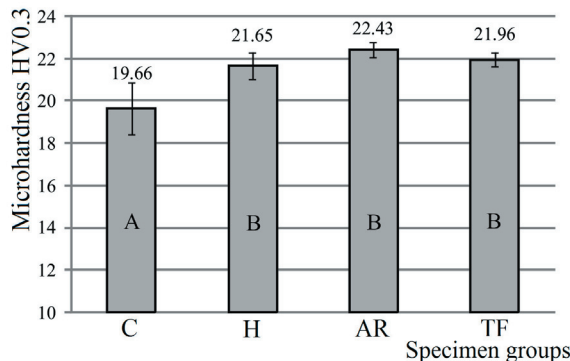


Fig. 9. Micro-hardness of tested materials with standard deviations

The aim of this paper was to compare conventional hot- and cold-curing (H and C) denture base materials and a novel PMMA material in as-received factory polymerized and thermoformed states (AR and TF). A full mechanical testing characterization was performed in order to evaluate material performance from different aspects.

The C specimen group, obtained in cold conditions (auto-polymerized PMMA), had the lowest elongation, bending strength, fracture toughness and micro-hardness. Such results are expected, due to a limited preparation time before the polymer becomes sufficiently viscous to prevent any further mixing [6] and [7]. Furthermore, standard deviations in the C specimen group are the highest of all the tested materials, the only exception being fracture toughness. Compared to C, the mechanical properties of the H specimen group are higher, which was expected due to a prolonged mixing and preparation, as well as additional compression and water heat after treatment aimed at decreasing monomer content [25]. Fracture location that occurs predominantly in one specific area (near specimen shoulder) indicates that the C specimen group may suffer from structural inconsistencies.

The tensile and bending strengths of the TF specimen group are slightly higher compared to the AR specimen group, with lower standard deviations. In contrast, the AR group has a higher micro-hardness compared to the TF group, but this advantage is also statistically insignificant. Only the fracture toughness of the AR is significantly higher than that of the TF group. Nevertheless, the TF specimen group's fracture toughness is significantly lower than that of both the H and AR groups and statistically equal to the C group. That means that the TF specimen group is more sensitive to load when a crack is present on the specimen surface. Although dentures theoretically initially do not have surface cracks, an array of defects may be present in the materials structure: porosity, inhomogeneous structure, surface flaws, etc. [13]. Furthermore, standard deviations in fracture toughness test may not be considered to be as the most representative, because the initial crack was made manually, i.e. manual initial crack preparation might induce a certain level of inaccuracy. However, based on obtained results, it can be said that the TF specimen group requires a more careful polishing compared to the H tested group.

The standard deviations in TF specimen group have relatively low standard deviations, which

might be achieved due to the factory synthesis and polymerization process. Such material preparation might be more accurate than the preparation in dental laboratory, where several operations are dependent on the technicians' skill.

The moderate increase in tensile and bending strengths, as well as the elongation of the TF versus AR specimen groups, although statistically non-significant, may be the result of a partial orientation of polymer chains during thermoforming. However, in specimens in which a strictly local deformation is induced (micro-hardness and fracture toughness testing) partially oriented polymer chains may offer a lower resistance due to relatively weak secondary bonds between them. The crack may propagate between the partially oriented chains more efficiently (TF group) than through the material with a more random polymer chain orientation (AR group). Testing results were also confirmed the fact that for brittle polymer materials bending strength is greater than tensile strength. In the literature, there are a few explanations for this phenomenon [26] to [28]. Another possible interpretation for this difference might be found in the structure of polymer material, i.e. in the bonds between the individual monomer components of the long chains such as carbon-carbon sigma bonds. In addition, monomer components have some dipoles perpendicular to the axis of the polymeric chain [29]. Because of this dipole, the parallel chains have some repulsion between them, which contributes to the bending strength of the polymer on the macro level. The bending interaction must overcome the repulsion as well as break the inter-monomer bonds in order to break the polymer material, whereas a tensile interaction must only break the inter-monomer bonds in enough places in each chain so as to cause macroscale failure.

When addressing its use in dental practice, it can be concluded that the novel PMMA material used in this study (AR, TH) showed satisfactory results compared to the conventional systems (H, C). The key benefits of the material, i.e. structural consistency and ease of handling, offer benefits for clinicians when constructing dental appliances. Further research will be focused on the clinical assessment of material properties, regarding their resilience, durability and comfort of wear for the patients.

4 CONCLUSIONS

In accordance with the obtained results, some conclusions can be drawn:

- Thermoformed PMMA materials mechanical properties are comparable to cold and hot polymerized PMMA materials. The tensile strength of thermoformed PMMA material is significantly lower than those of cold and hot PMMA materials. Furthermore, fracture toughness is lower for thermoformed than that of hot polymerized PMMA.
- Standard deviations obtained for thermoformed PMMA material are lower than those obtained with cold and hot polymerized PMMA materials. That means that the repeatability of the results and the consistency of mechanical properties is higher for the thermoformed PMMA.
- The main reason for the relatively high consistency of the obtained mechanical properties in thermoformed specimens may be attributed to industrial polymerization process, which might be more accurate than the preparation in the dental laboratory.

5 ACKNOWLEDGEMENT

The results of the investigation presented in this paper are part of the research realized in the framework of the project "Research and development of modeling methods and approaches in manufacturing of dental recoveries with the application of modern technologies and computer aided systems"-TR 035020, financed by the Ministry of Science and Technological Development of the Republic of Serbia.

The authors also thank the CEEPUS program for making them possible to be mobile within the network CII-HR-0108.

6 REFERENCES

- [1] Jagger, D.C., Harrison, A., Jandt, K.D. (1999). The reinforcements of dentures-review. *Journal of Oral Rehabilitation*, vol. 26, no. 3, p. 185-194, DOI:10.1046/j.1365-2842.1999.00375.x.
- [2] Bettencourt, A.F., Neves, C.B., de Almeida, M.S., Pinheiro, L.M., Oliveira, S.A., Lopes, L.P., Castro, M.F. (2010). Biodegradation of acrylic based resins: A review. *Dental Materials*, vol. 26, no. 5, p. 171-180, DOI:10.1016/j.dental.2010.01.006.
- [3] Krunić, N., Kostić, M., Anđelković, M. (2007). Acrylic resins-still irreplaceable material in prosthetic dentistry. *Acta Stomatologica Naissii*, vol. 23, no. 56, p. 747-752. (in Serbian)
- [4] Asar, N.V., Albayrak, H., Korkmaz, T., Turkyilmaz, I. (2013). Influence of various metal oxides on mechanical and physical properties of heat-cured polymethyl methacrylate denture base resins. *Journal of Advanced Prosthodontics*, vol. 5, no. 3, p. 241-247, DOI:10.4047/jap.2013.5.3.241.

- [5] Vallittu, P.K. (1996). A review of fiber reinforced denture base resins. *Journal of Prosthodontics*, vol. 5, no. 4, p. 270-276, DOI:10.1111/j.1532-849X.1996.tb00511.x.
- [6] Balos, S., Balos, T., Sidjanin, L., Markovic, D., Pilic, B., Pavlicevic, J. (2011). Study of PMMA Biopolymer Properties Treated by Microwave Energy. *Materiale Plastice*, vol. 48, no. 2, p. 127-131.
- [7] Balos, S., Balos, T., Sidjanin, L., Markovic, D., Pilic, B., Pavlicevic, J. (2009). Flexural and impact Strength of Microwave Treated Autopolymerized Poly (Methyl-Methacrylate). *Materiale Plastice*, vol 46, no. 3, p. 261-265.
- [8] Balos, S., Pilic, B., Markovic, D., Pavlicevic, J., Luzanin, O. (2014). Poly(methyl-methacrylate) nanocomposites with low silica addition. *Journal of Prosthetic Dentistry*, vol. 111, no. 4, p. 327-334, DOI:10.1016/j.prosdent.2013.06.021.
- [9] Hargreaves, A.S. (1969). The prevalence of fractured dentures. A survey. *British Dental Journal*, vol. 126, no. 10, p. 451-455.
- [10] Curtis R.V., Watson, T.F. (eds.) (2009). *Dental biomaterials Imaging, Testing and Modeling*, Wookhead Publishing, Cambridge.
- [11] Khasawneh, S.F., Arab, J.M. (2003). A clinical study of complete denture fractures at four military hospitals in Jordan. *Jordanian Royal Medical Services*, vol. 10, no. 2, p. 27-31.
- [12] Prombonas, A.E., Vlissidis, D.S. (2006). Comparison of the midline stress fields in maxillary and mandibular complete dentures: A pilot study. *Journal of Prosthetic Dentistry*, vol. 95, no. 1, p. 63-70, DOI:10.1016/j.prosdent.2005.11.009.
- [13] Anusavice, K. J., Shen, C., Rawls, H. R. (2013). *Phillips' Science of Dental Materials*, 12th ed., Elsevier/Saunders, St. Louis.
- [14] Austin, A.T, Basker, R.M. (1982). Residual monomer levels in denture bases. The effect of varying short curing cycles. *British Dental Journal*, vol. 53, no. 12, p. 424-426, DOI:10.1038/sj.bdj.4804962.
- [15] Autian, J. (1975). Structure-toxicity relationship of acrylic monomers. *Environmental Health Perspectives*, vol. 11, p. 141-152, DOI:10.1289/ehp.7511141.
- [16] Lee, H.H, Lee, C.J, Asaoka, K. (2012). Correlation in the mechanical properties of acrylic denture base resins. *Dental Materials Journal*, vol. 31, no. 1, p. 157-164, DOI:10.4012/dmj.2011-205.
- [17] Scheu-dental (2014). Scheu-dental.com, Iserlohn, from <http://www.scheu-dental.com>, accessed on 2014-02-12.
- [18] ASTM D638 (2010). Standard Test Method for Tensile Properties of Plastics, ASTM International, West Conshohocken, DOI:10.1520/D0638-10.
- [19] ISO 20795-1:2013. *Dentistry— Base Polymers— Part 1: Denture Base Polymers*. International Organization for Standardization, Geneva.
- [20] ASTM D5045 (2014). *Standard Test Methods for Plane-Strain Fracture Toughness and Strain Energy Release Rate of Plastic Materials*. ASTM International, West Conshohocken, DOI:10.1520/D5045-14.
- [21] Sulym, I.Y., Borysenko, M.V., Goncharuk, O.V., Terpilowski, K., Sternik, D., Chibowski, K., Gun'ko, V.M. (2011). Structural and hydrophobic-hydrophilic properties of nanosilica/zirconia alone and with adsorbed PDMS. *Applied Surface Science*, vol. 258, no. 1, p. 270-277, DOI:10.1016/j.apsusc.2011.08.045.
- [22] Lazzara, G., Milioto, S. (2010). Dispersions of nanosilica in biocompatible copolymers. *Polymer Degradation and Stability*, vol. 95, no. 4, p. 610-617, DOI:10.1016/j.polymdegradstab.2009.12.007.
- [23] Zhu, A., Cai, A., Zhou, W., Shi, Z. (2008). Effect of flexibility of grafted polymer on the morphology and property of nanosilica/PVC composites. *Applied Surface Science*, vol. 254, no. 13, p. 3745-3752, DOI:10.1016/j.apsusc.2007.11.042.
- [24] Balos, S., Sidjanin, L., Pilic, B. (2014). Indentation size effect in autopolymerized and microwave post treated Polymethyl methacrylate denture relin resin. *Acta Polytechnical Hungarica*, vol. 11, no. 7, p. 239-249.
- [25] Lamb, D.J, Ellis, B, Priestley, D. (1983) The effects of process variables on levels of residual monomer in autopolymerizing dental acrylic resin. *Journal of Dentistry*, vol. 11, no. 1, p. 80-88, DOI:10.1016/0300-5712(83)90051-9.
- [26] Odian, G. (1991). *Principles of Polymerization*, 3rd ed., Wiley, New York, p. 24-39.
- [27] Van Krevelen D.W., Nijenhuis K.T. (2009). *Properties of Polymers: Their Correlation with Chemical Structure; Their Numerical Estimation and Prediction from Additive Group Contributions*. 4th ed., Elsevier, Amsterdam, p. 383-500, DOI:10.1016/B978-0-08-054819-7.00013-3.
- [28] Landel, R.F, Nielsen, L.E. (1994). *Mechanical Properties of Polymers and Composites*, 2nd ed., revised and expanded, Marcel Dekker, New York, p. 233-299.
- [29] Rosen, C.Z, Hiremath, B.V, Newnham, R.E. (1991). *Piezoelectricity: Key Papers in Physics*. American Institute of Physics, p. 159-181.

Vsebina

Strojniški vestnik - Journal of Mechanical Engineering

letnik 61, (2015), številka 2

Ljubljana, februar 2015

ISSN 0039-2480

Izhaja mesečno

Razširjeni povzetki

- Karol Franciszek Abramek, Tomasz Stoeck, Tomasz Osipowicz: Statistična analiza korozivne obrabe elementov šob za vbrizgavanje goriva v sistemih skupnega voda SI 19
- Liao Yunfei, Zhou Yi, Liu Youhai, Zuo Dong, Tan Bo: Študija stabilnosti natančne deljene mrežice SI 20
- Diego E. Lozano, Gabriela Martinez-Cazares, Rafael D. Mercado-Solis, Rafael Colás, George E. Totten: Ocenjevanje prehodne temperaturne porazdelitve med kaljenjem s paraboličnim modelom SI 21
- Yi Jiangang: Modeliranje in analiza odziva sistema samodejnega hidravličnega krmiljenja debeline na stopnico SI 22
- Serkan Balli, Faruk Sen: Uporaba mehkega ekspertnega sistema za napovedovanje odpovedi navzkrižno laminiranih mehansko povezanih kompozitov SI 23
- Xiaoming Huang, Jie Sun, Jianfeng Li: Vpliv začetnih in z obdelavo povzročenih preostalih napetosti na deformacije plošč iz aluminijeve zlitine SI 24
- Sebastian Baloš, Mladomir Milutinović, Michal Potran, Jelena Vuletić, Tatjana Puškar, Tomaž Pepelnjak: Mehanske lastnosti litih in termoformiranih polimernih zobnih vložkov SI 25

Osebnosti

- Doktorska disertacija, diplomske naloge SI 26

Statistična analiza korozivne obrabe elementov šob za vbrizgavanje goriva v sistemih skupnega voda

Karol Franciszek Abramek – Tomasz Stoeck* – Tomasz Osipowicz

Tehnična univerza v Zahodnem Pomorjanskem, Oddelek za avtomobilsko tehniko, Poljska

Glavni namen predstavljene študije je statistično ovrednotenje korozivne obrabe elementov šob za vbrizgavanje goriva različnih tipov in različnih proizvajalcev ob upoštevanju dejavnikov, ki negativno vplivajo na zanesljivost delovanja. V analizi je bila obravnavana tudi praktična izvedba popravil ter možnost odprave ugotovljenih pomanjkljivosti z ozirom na stopnjo obrabe posameznih delov in možnosti njihove zamenjave.

V analizo so bile vključene izbrane komponente, razkrila pa je elemente in sestave, ki so najpogosteje podvrženi uničevalnim procesom. Statistična analiza je bila opravljena na podlagi eksperimentalnih podatkov, pridobljenih pri preverjanju zasnov šob za vbrizgavanje goriva različnih generacij. V ta namen je bil uporabljen koncept gostote korozije, povezan z avtorsko razvrstitvijo stopnje obrabe elementov. Določen je bil odstotni delež učinkovitosti popravil ob upoštevanju števila prevoženih kilometrov. Predstavljene so tipične težave s šobami za vbrizgavanje goriva vodilnih proizvajalcev ter podrobnejša razčlenitev izbranih primerov.

Članek se sklicuje na statistične študije korozije šob za vbrizgavanje goriva v sistemu skupnega voda, ki so bile predstavljene v članku Taflan R. A., Karamangil M. I. (2012). Statistical corrosion evaluation of nozzles used in diesel CRI systems. *Fuel*, št. 102, str. 41-48 [13] Ob analogni teoretični podlagi so bila uvedena tudi lastna merila avtorjev za razvrščanje, kakor tudi razširitev spektra eksperimentov z dejavniki, ki do sedaj še niso bili upoštevani: npr. delovni proces, delovni tlak, kazalniki učinkovitosti popravil itd.

Razen šob, ki so izpostavljene vplivu visokih temperatur in reakcijam v zgorevalnem prostoru, so žrtev uničevalnih procesov v podobni meri tudi sestavi krmilnih ventilov in armatur, ki so v neposrednem stiku z dovajanim gorivom pod visokim tlakom. Obraba električnih elementov je manj pogosta, ker do takšnih stikov ne prihaja, toda šoba za vbrizgavanje goriva ob ugotovljeni neustreznosti ni več primerna za nadaljnjo uporabo, saj je ni mogoče očistiti ali zamenjati. Razpoložljivost nadomestnih delov je ključnega pomena za učinkovitost popravila šob za vbrizgavanje goriva, saj nedobavljivih (ali omejeno razpoložljivih) elementov oz. sestavov pod močnim vplivom korozije ni mogoče zamenjati. Z nabiranjem števila prevoženih kilometrov se povečuje tudi gostota korozije, saj so bili sledovi višje in visoke stopnje korozije ugotovljeni pri večjem številu delov.

Inovativnost študije se kaže v tem, da niso bili preučeni le natančni deli (šoba z iglo), ki jih obravnava večina razpoložljivih objav, temveč tudi drugi elementi in sestavi sistema dovoda goriva. Ob upoštevanju preučevanih vrst obrabe so tokrat prvič podrobno opisani tipični načini odpovedi za konstrukcije vodilnih proizvajalcev sistemov vbrizgavanja, vključno z različnimi tipi in generacijami.

Ključne besede: šobe za vbrizgavanje goriva s skupnim vodom, korozija komponent, statistična analiza

Študija stabilnosti natančne deljene mrežice

Liao Yunfei – Zhou Yi* – Liu Youhai – Zuo Dong – Tan Bo

Kolidž za strojništvo, Univerza v Chongqingu, Kitajska

Za izboljšanje stabilnosti deljenih mrežic, ki so se uveljavile pri gradnji metrskih večslojnih dielektričnih (MLD) uklonskih mrežic kot ključna komponenta kompresorja v laserskem sistemu CPA, smo razvili natančno deljeno mrežico in analizirali njeno stabilnost. Stabilnost deljene mrežice je namreč eden najpomembnejših dejavnikov uspeha laserskega eksperimenta.

Za izboljšanje konstrukcijske stabilnosti smo zasnovali deljeno mrežico v obliki tetraedra, ki izboljšuje vibracijsko stabilnost naprave. Za zmanjšanje vpliva naraščajočega faktorja prenosa napak smo dodali navidezno stojalo v oporo mrežici. Deljena naprava se tako izogne območju s hitro naraščajočimi faktorji prenosa napak ter zagotavlja dobro natančnost nastavitve in stabilnost. Za povečanje stabilnosti krmiljenja smo izboljšali krmilne algoritme PID po dvotočkovni shemi: 1) metoda zaklenjene kompenzacije preprečuje nasičene izgube zaradi integriranega nasičenja, in 2) metoda štiritočkovne osrednje razlike omogoča pridobitev parametrov razlik pri odpravljanju motenj.

Za preizkus in verifikacijo stabilnosti prototipa deljene mrežice smo zasnovali testno konfiguracijo. Laserski žarek pri valovni dolžini 532 nm je bil z delilnikom razdeljen na dva žarka z enako energijo. Prvi žarek je bil projiciran na tarčo po odboju na delilniku, drugi pa je bil projiciran na tarčo po odboju na zrcalu deljene mrežice. S kamero smo posneli točke na tarči in po slikovni obdelavi določili relativni položaj označene točke za uporabo v izračunih. Ostrina točke je v našem eksperimentu ostala nespremenjena. Merilna napaka vseh podatkov, ki jih je ustvaril program za prepoznavo slik, je bila zato pri vseh slikah enaka. V izračunih lahko to napako odstranimo in dosežemo večjo natančnost testa.

Predmet članka je izboljšanje stabilnosti optične opreme s konstrukcijsko zasnovano, prenosno verigo in krmilnim algoritmom. Stabilnost je preizkušena in potrjena z optičnim eksperimentom.

Numerična analiza in eksperiment sta privedla do naslednjih rezultatov:

1. S spremembo zasnove deljene mrežice iz konstrukcije z vzporednimi ploščami v tetraedrično konstrukcijo se izboljša lastna frekvenca v prvi fazi, maksimalni pomik naprave pa se prenese s površine mrežice na oporo, s čimer se občutno izboljša vibracijska stabilnost deljene mrežice.
2. Z analizo napak prenosa naprave in dodajanjem navideznega stojala v izogib območju, kjer se faktor prenosa napake hitro poveča, smo upočasnili rast faktorja prenosa napak in zmanjšali vpliv na napako krmiljenja.
3. Z izboljšanjem krmilnih algoritmov PID smo se izognili nasičeni izgubi, zmanjšali vpliv motenj iz okolja in povečali odzivnost.
4. Eksperimenti so dokazali stabilnost vzorčne naprave. Kot mrežice je po 380 sekundah v smereh X in Y zlezal za 0,243 μ rad oz. $1,46 \times 10^{-3}$ μ rad.

Za izboljšanje stabilnosti deljenih mrežic smo razvili natančno mrežico in analizirali njeno stabilnost.

Ključne besede: kompresor z deljeno mrežico, stabilnost, dinamični odziv, tetraeder, prenosna veriga, krmilni algoritmi

Ocenjevanje prehodne temperaturne porazdelitve med kaljenjem s paraboličnim modelom

Diego E. Lozano^{1,*} – Gabriela Martinez-Cazares² – Rafael D. Mercado-Solis² – Rafael Colás² – George E. Totten³

¹ FRISA, Mehika

² Avtonomna univerza v Nuevo Leónu, Mehika

³ Državna univerza v Portlandu, ZDA

Gasilna sredstva z izboljšanim prenosom toplote in učinkovitostjo kaljenja so predmet stalnih raziskav na področju tehnologije toplotne obravnave. Za preizkušanje teh lastnosti se običajno uporabljajo preizkušanci z enim ali več termopari za beleženje časovnega poteka temperature med kalilnim ciklom. Hitrost odvajanja toplote iz preizkušanca (t. j. hitrost ohlajevanja) se lahko izračuna z analizo ohlajevalne krivulje. Ohlajevalne krivulje, pridobljene s pomočjo takih preizkušancev, se lahko uporabijo za ocenjevanje površinske temperature med kaljenjem, kakor tudi za izračun toplotne prehodnosti (HTC) in gostote toplotnega toka (HFD). Ta dva parametra zadostujeta za popis celotnega prenosa toplote v kalilnem sistemu. Najbolj priljubljena tehnika za izvedbo teh izračunov je t. i. problem inverznega prevajanja toplote (IHCP). IHCP je zasnovan na numeričnem reševanju dobro znane Fourierjeve parcialne diferencialne enačbe. Čeprav je učinkovitost IHCP dodobra preverjena, pa je pravilna rešitev problema v vsakem primeru odvisna predvsem od vnosa pravih termofizikalnih lastnosti, ki jih ni vedno enostavno izmeriti. To je verjetno tudi glavna slabost IHCP.

V študiji je predstavljen od materiala neodvisen model za ocenjevanje prehodne porazdelitve temperature v preizkušancu, kaljenem s potapljanjem. Model sloni na predpostavki, da je radialno porazdelitev temperature ob koncu intervala pri enorazsežnostnem nestacionarnem prevajanju toplote mogoče popisati s parabolično enačbo. Model je bil validiran s preizkušanci ($\phi 8 \times 40$ mm in $\phi 12 \times 60$ mm) iz nerjavnega jekla AISI 304 na temperaturi 850 do 900 °C, ki so bili kaljeni v vodi in v vodni raztopini NaNO_2 na temperaturi 25 °C, ter v olju oljne ogrščice na temperaturi 50 °C. Za primerjavo so bili v vodi gašeni kvadratni preizkušanci ($20 \times 20 \times 100$ mm) na temperaturi 550 °C. Preizkušanci so bili opremljeni z vdelanimi termopari za beleženje časovne odvisnosti temperature v jedru, na $\frac{1}{4}$ debeline in 1 mm pod površino. Podatki, zabeleženi s termopari v jedru in blizu površine, so bili pri vsakem eksperimentu uporabljeni za izračun temperature, podatki termopara na $\frac{1}{4}$ debeline pa so pomagali pri validaciji modela. Izračunana temperaturna porazdelitev se je v vseh primerih dobro ujemala z eksperimentalno pridobljenimi vrednostmi.

Parabolični model, ki je predstavljen v tem članku, lahko pravilno popiše radialni temperaturni profil preizkušancev različnih velikosti in z različnimi gasilnimi mediji. Za analizo je potrebna samo zgodovina temperature v dveh točkah v radialni smeri. Prednost je v tem, da ni potrebno poznavanje nobenih termofizikalnih lastnosti, neposredna uporaba preprostih algebrskih enačb pa skrajša čas izračuna na minimum ob sprejemljivi točnosti. Iz tega sledi, da je takšen pristop enostavno, hitro in učinkovito orodje za ocenjevanje prehodne porazdelitve površinske in radialne temperature ter je uporabno sredstvo za izračunavanje hitrosti ohlajevanja v gasilnem sredstvu in za karakterizacijo prenosa toplote. Izkazalo se je, da je ta metoda primernejša za gašenje v olju, kjer ni prevelikih temperaturnih gradientov, sprejemljive rezultate pa daje tudi pri vodi in vodnih raztopinah. Ko je izračunana površinska temperatura, se postopek ugotavljanja toplotne prehodnosti in gostote toplotnega toka močno poenostavi z neposredno rešitvijo enačbe toplotnega toka.

Ključne besede: temperaturna porazdelitev, kaljenje, parabola, toplotna prehodnost, hitrost ohlajevanja, analiza ohlajevalne krivulje

Modeliranje in analiza odziva sistema samodejnega hidravličnega krmiljenja debeline na stopnico

Yi Jiangang*

¹ Univerza Jianghan, Državni laboratorij v Hubeiju
za nadzor nad industrijskimi izpusti in onesnaževanjem s prahom, Kitajska

Debelina pločevine je eden glavnih kazalnikov kakovosti pločevine v procesu valjanja. Uveljavljena rešitev za izboljšanje natančnosti krmiljenja debeline pločevine je samodejno hidravlično krmiljenje (HAGC). V delovanju HAGC ima najpomembnejšo vlogo odziv na stopnico, saj določa hitrost valjanja in debelino jeklene pločevine, obenem pa vpliva na kakovost njene površine. Preizkus z odzivom na stopnico je metoda v časovni domeni za ugotavljanje dinamičnih lastnosti sistema. Uporablja se za opis dinamičnega odziva krmilnega sistema na vhodni signal v obliki stopnice. Za enakomerno debelino jeklene pločevine se morajo parametri odziva HAGC na stopnico sprti prilagajati dejanski debelini jeklene pločevine. Odziv HAGC na stopnico je odvisen od medsebojnih interakcij hidravličnih cilindrov, servoventilov in različnih senzorjev v sistemu, delovni čas pa je izjemno kratek (največ ena sekunda). Modeliranje, preizkušanje in analiziranje odziva HAGC na stopnico je zato ključnega pomena.

V članku je najprej analiziran postopek preizkušanja odziva HAGC na stopnico in opisani so glavni delovni parametri. Nato je s pomočjo prenosnih funkcij postavljen testni model odziva na stopnico. Predlagani model z izbranimi delovnimi parametri je bil simuliran s paketom MATLAB. Za skrajšanje časa uestalitve in največjega prenihaja HAGC je bil v shemo za test odziva na stopnico dodan člen PID. Sledi primerjava in analiza rezultatov simulacij modela za preizkušanje odziva na stopnico s konvencionalnim členom PID in brez njega. Na podlagi tega je za kompenzacijo vhodnega signala predlagan adaptivni proporcionalno-integrirno-diferencirni (APID) člen z uporabo nevronske mreže z vzvratnim postopkom učenja (BPNN). Končno so bile opravljene še simulacije in eksperimenti za verifikacijo učinkovitosti izboljšane modela preskušanja odziva na stopnico.

Test odziva HAGC na stopnico je pokazal, da je težko uravnovežiti stabilnost in fleksibilnost sistema. Dodajanje ustreznega člena za kompenzacijo vhodnega signala se je izkazalo kot primerna rešitev za izboljšanje učinkovitosti krmiljenja s sistemom HAGC. Dodani člen PID sicer omogoča skrajšanje časa uestalitve in zmanjšanje prenihaja, toda konvencionalni PID-algoritem pri HAGC v začetni fazi povzroča trepetanje. Vzrok tiči v konstantnih parametrih PID konvencionalnega PID-algoritma med preizkusom odziva na stopnico. Ta je v realni proizvodnji jeklene pločevine nelinearen in časovno spremenljiv zaradi interakcij med servoventili, cilindri in senzorji sistema HAGC, parametre PID sistema HAGC pa je zato treba prilagajati vhodnim in izhodnim signalom.

V izboljšanem modelu za preizkušanje odziva na stopnico s členom APID je uporabljena mreža BPNN za adaptivno izračunavanje ustreznih parametrov PID na podlagi učenja s pridobljenimi vzorci. Mreža je sestavljena iz vhodne plasti z dvema nevronoma, skrite plasti s štirimi nevroni in izhodne plasti s tremi nevroni. Rezultati simulacij kažejo, da zasnovani model odziva na stopnico s členom APID učinkovito odpravlja trepetanje, zmanjša prenihaj, skrajša čas uestalitve ter pospeši dinamični odziv sistema HAGC. Pri uporabi algoritma APID in konvencionalnega algoritma PID je bila izmerjena sprememba debeline jeklene pločevine v času 100 ms. Eksperimenti so pokazali, da sprememba debeline v preizkusu odziva HAGC z APID na stopnico ni večja od 0,06 mm, površinske nepravilnosti pa se sčasoma zmanjšajo. Sprememba debeline pri konvencionalnem PID-algoritmu je 0,30 mm, torej bistveno večja kot z APID. Eksperimentalni rezultati se ujemajo z rezultati simulacij, izboljšani model odziva na stopnico pa omogoča stabilnejše in hitrejše valjanje jeklene pločevine. Izboljšani model preizkušanja odziva na stopnico s členom APID lahko skrajša čas uestalitve in zmanjša prenihaj, odpravi pa tudi trepetanje sistema HAGC v začetni fazi za večjo kakovost površine jeklene pločevine. V nadaljnjih raziskavah bo analiziran vpliv na odziv na stopnico tudi za druge komponente sistema HAGC, kot so hidravlične cevi in hidravlične črpalke.

Ključne besede: odziv na stopnico, HAGC, PID, umetne nevronske mreže, simulacija, eksperiment

Uporaba mehkega ekspertnega sistema za napovedovanje odpovedi navzkrižno laminiranih mehansko povezanih kompozitov

Serkan Ballı^{1,*} – Faruk Sen²

¹ Muğla Sıtkı Koçman University, Fakulteta za tehnične vede, Oddelek za informacijske sisteme, Turčija

² Muğla Sıtkı Koçman University, Fakulteta za tehnične vede, Oddelek za energetske sisteme, Turčija

Cilj predstavljene študije je ustvarjanje modela za napovedovanje obremenitve, pri kateri pride do odpovedi mehansko povezanih kompozitnih plošč, z mehkim ekspertnim sistemom. Mehki ekspertni sistemi omogočajo odločanje na podlagi numeričnih operacij namesto na podlagi simboličnih pravil, v čemer se razlikujejo od tradicionalnih ekspertnih sistemov. Mehki podatki omogočajo fleksibilnejšo predstavitev in občutljivejše rezultate.

V študiji so bili uporabljeni kompozitni materiali, ojačeni s steklenimi vlakni. Za modeliranje in napovedovanje obremenitev, pri katerih pride do odpovedi, so bili uporabljeni rezultati predhodne eksperimentalne študije kompozitnih plošč z navzkrižno laminiranimi plastmi, ki so bile spojene z dvema zatičema ali vijakoma v vrsti. Eksperimentalni podatki predhodne študije so bili pridobljeni za različne geometrijske parametre pri različnih predobremenitvenih momentih (zatičnega/vijačnega spoja) 2, 3, 4 oz. 5 Nm. Pravokotni preizkušanci so bili pripravljene iz laminiranega kompozita epoksi smole in steklenih vlaken, in sicer z dvema krožnima luknjama v vrsti. Pri eksperimentih sta bila uporabljena dva toga zatiča/vijaka. Premer obeh lukenj (D) je bil 5 mm. Zunanja luknja je bila pozicionirana na središčnici plošče, na razdalji E od roba preizkušanca. Notranja luknja je bila pozicionirana na razdalji K od središča zunanje luknje. Razmerje med razdaljo od roba in premerom luknje (E/D) je bilo torej 1, 2, 3, 4 oz. 5. Razmerje med širino plošče in premerom luknje (W/D) je bilo 2, 3, 4 oz. 5. Razmerje med razmikom in premerom lukenj (K/D) je bilo 3, 4 oz. 5. Celotna dolžina ($L + K + E$) preizkušancev je bila 135 mm. Laminirani kompozitni preizkušanci so bili narejeni iz osmih enosmernih plasti, zloženih po formuli $[0 / 0 / 90 / 90^{\circ}]_s$. Preizkušanci so bili med eksperimentom obremenjeni z enakomerno natezno obremenitvijo P prek togih zatičev/vijakov.

Analiza z mehkim ekspertnim sistemom in z regresijsko analizo je upoštevala te geometrijske parametre ter konfiguracijo spojev z zatičema/vijakoma. Uporabljenih je bilo torej 5 geometrijskih parametrov in 300 kompletov testnih podatkov. Mehčanje podatkov za mehki ekspertni sistem je bilo opravljeno skladno s članskimi funkcijami. Uporabljene so bile tri mehke množice – nizka, srednja in visoka. Mehki inferenčni stroj je obsegal 4 kriterije in po 3 mehke množice za vsak kriterij. Skupno je bil torej sestavljen iz 34 pravil, oblikovanih skladno z ekspertnim znanjem in izkušnjami. Za vrednotenje učinkovitosti metod so bili uporabljeni determinacijski koeficient (R^2), absolutna srednja napaka (MAD) in absolutna odstotna srednja napaka (MAPD). Ugotovljeno je bilo, da sta vrednosti MAD in MAPD mehkega ekspertnega sistema manjši kot pri regresijski analizi. To pomeni, da lahko mehki ekspertni sistem dobro modelira problem ter da je napaka napovedi majhna. Determinacijski koeficient mehkega ekspertnega sistema je večji kot pri regresijski analizi in dokazuje, da je napoved blizu pričakovanim vrednostim.

V študiji je bil uporabljen nov pristop k napovedovanju vedenja mehansko spojenih navzkrižno laminiranih kompozitov s pomočjo mehkega ekspertnega sistema. Očitno je, da je mehki ekspertni sistem pri napovedovanju obremenitve, kjer pride do odpovedi kompozitnih materialov, učinkovitejši od metode regresijske analize, ki potrebuje več dodatnih parametrov za boljše napovedi v negotovem okolju. Mehki ekspertni sistem je primernejši od metode regresijske analize za modeliranje nelinearnih problemov ter za izražanje negotovosti. Prednost numerične študije je v tem, da v primerjavi s predhodnimi eksperimentalnimi študijami ne ustvarja odpadkov. Znano je tudi, da so eksperimentalne metode dražje in zamudnejše od računskih študij.

Ključne besede: mehki ekspertni sistem, vijačna zveza, zveza z zatičem, mehanska zveza, laminirani kompoziti, mehka logika

Vpliv začetnih in z obdelavo povzročenih preostalih napetosti na deformacije plošč iz aluminijeve zlitine

Xiaoming Huang¹ – Jie Sun^{1,2,*} – Jianfeng Li^{1,2}

¹ Univerza Shandong, Fakulteta za strojništvo, Kitajska

² Ministrstvo za šolstvo, Državni laboratorij za visokoučinkovito in čisto proizvodnjo, Kitajska

Za določitev vzrokov in glavnih dejavnikov nastanka deformacij po obdelavi tankostenskih komponent so bile preučene deformacije letalskih komponent s pomočjo teoretičnega analitičnega modela, numeričnih izračunov po metodi končnih elementov in eksperimentalno. Članek raziskuje vpliv začetnih preostalih napetosti v surovcu ter preostalih napetosti po obdelavi na deformacije plošč iz letalske aluminijeve zlitine.

Porazdelitev začetnih preostalih napetosti v surovcu ter preostalih napetosti po obdelavi monolitne letalske komponente povzroča pojav deformacij. To je eden najresnejših problemov, s katerim se soočajo proizvajalci letal, vpliv preostalih napetosti na deformacije tankostenskih komponent pa še ni bil v celoti preučen. Članek poroča o meritvah in analizi značilnosti deformacij, preučeno pa je tudi razmerje med maksimalnim odklonom in debelino preskušancev.

Analiziran je bil teoretični model deformacije plošč in opravljena je bila analiza po metodi končnih elementov (MKE) za ugotavljanje razmerja med deformacijami po obdelavi in preostalimi napetostmi. Nato so bili postavljeni eksperimenti z visokohitrotnim rezkanjem in jedkanjem za validacijo teoretičnega modela in modela po MKE. Deformacije plošče iz aluminijeve zlitine so bile analizirane z ozirom na delovanje začetnih preostalih napetosti, preostalih napetosti po obdelavi in skupno delovanje teh dveh dejavnikov.

Na tankostenskih preskušancih so se pojavile konveksne in upogibne deformacije, preostale napetosti po obdelavi pa povzročajo privzdigovanje obdelane strani. Preostale napetosti po obdelavi so glavni vzrok deformacije plošč.

Položaj plošče ima določen vpliv na velikost deformacij: deformacije so večje, ko je plošča v območju natezних preostalih napetosti surovca, oz. manjše, ko je plošča v območju tlačnih preostalih napetosti surovca. Analizirana so bila razmerja med maksimalnim odklonom in debelino preskušancev, rezultati pa kažejo, da imajo preostale napetosti po obdelavi večji vpliv na deformacije plošče, ko je debelina manjša od 1,25 mm.

Trend rezultatov analize deformacij po MKE se ujema z eksperimentalnimi rezultati, vrednosti pa so večje kot pri meritvah. Maksimalna von Misesova napetost se zmanjšuje praktično linearno z odstranjevanjem materiala.

Omejitve raziskave, implikacije: Predmet te raziskave je plošča iz aluminijeve zlitine enostavne geometrije. V nadaljnjih študijah bo treba podrobneje raziskati deformacije kompleksnih monolitnih komponent. Iz članka lahko izidejo tudi smernice za dodatne študije deformacij po obdelavi in tehnologij za odpravo deformacij pri monolitnih aeronavtičnih komponentah.

Prispevek, novosti, vrednost: Študija preučuje vpliv začetnih in z obdelavo povzročenih preostalih napetosti v materialu na deformacije plošč iz aluminijeve zlitine. Najprej je bil analiziran teoretični model plošče in nato so bili opravljeni eksperimenti za določitev deformacij po rezkanju pri različnih pogojih začetnih preostalih napetosti. Rezultati kažejo, da so glavni krivec za deformacije preostale napetosti po obdelavi. Skupno delovanje tlačnih začetnih preostalih napetosti in preostalih napetosti po obdelavi povečuje deformacije plošče, skupno delovanje natezних začetnih preostalih napetosti in preostalih napetosti po obdelavi pa deformacije plošče zmanjšuje. Rezultati simulacije po metodi končnih elementov se dobro ujemajo z eksperimentalnimi rezultati in iz članka lahko izidejo smernice za nadzor in odpravljanje deformacij pri monolitnih letalskih komponentah.

Ključne besede: tanke stene, deformacije po obdelavi, preostale napetosti po obdelavi, začetne preostale napetosti v obdelovancu, jedkanje, MKE

Mehanske lastnosti litih in termoformiranih polimernih zobnih vložkov

Sebastian Baloš¹ – Mladimir Milutinović¹ – Michal Potran² – Jelena Vuletić² – Tatjana Puškar² – Tomaž Pepelnjak^{3,*}

¹ Univerza v Novem Sadu, Fakulteta za tehnične vede, Srbija

² Univerza v Novem Sadu, Medicinska fakulteta, Srbija

³ Univerza v Ljubljani, Fakulteta za strojništvo, Slovenija

V članku je predstavljena študija mehanskih lastnosti in dosežene trdnosti polimera polimetilmethakrilata (PMMA), ki se uporablja za zobne proteze. Pri uporabi polimera za zobne proteze je v prvi vrsti pomembna njegova biološka kompatibilnost in netoksičnost. V tem pogledu se pokaže PMMA kot ustrezen material za tovrstne proizvode. Nadalje je pri izbiri materiala ključnega pomena čim višja trdnost polimera, ki se jo v primeru uporabe PMMA danes dosega z impregnacijo z butadien-stirenom, mikrovalovi, potekale so tudi raziskave utrjevanja PMMA z dodajanjem nanodelcev.

Zagotavljanje zadostne tlačne trdnosti pri materialih za proteze običajno ni problematično. Večji izziv predstavlja implementacija materialov, ki ob uporabi v zobnih protezah zdržijo zadostne natezne obremenitve ter kombinacije natezno-tlačnih obremenitev po različnih segmentih proteze. Slednje se kot primer pojavljajo v sredini nebnege loka celotne zobne proteze, kjer se tudi najpogosteje pojavijo lomi po nekaj letih uporabe.

Lastnosti izdelka – osnove za proteze – so v veliki meri odvisne od izbranega materiala, njegove predhodne obdelave in izdelave proteze. Ta se najpogosteje izvaja z oblikovanjem (litjem) baznih smol - termoplastov. Alternativo litju predstavlja tudi termoformiranje, ki trenutno še ni ustaljen postopek pri izdelavi zobnih protez in predstavlja noviteto na področju zobne protetike.

S ciljem ugotavljanja trdnostnih lastnosti termoformiranih osnov zobnih protez iz PMMA se je izvedlo analizo mehanskih lastnosti in trdot. V analizo so bili zajeti različno pripravljene vzorci materiala Triplex Cold, Triplex Hot in Biocryl C; vsi namenjeni za komercialno izdelavo zobnih protez. Materiali so bili bodisi hladno ali topopolimerizirani, liti in strjevani (Triplex) ali izdelani iz toplotno obdelane in neobdelane PMMA folije (Biocryl C).

Analiza mehanskih lastnosti testiranih smol je sestavljena iz nateznih preizkusov, tritočkovnega preizkusa za določevanje upogibne trdnosti, merjenja raztezka, žilavosti in mikrotrdote. Dobljene podatke meritev smo statistično obdelali s pomočjo enosmerne analize variance (ANOVA), s »Tukey post-hoc« testom in α -nivojem pomembnosti 0,05.

Triplex hladno strjevani vzorci so pokazali najnižjo upogibno trdnost, žilavost in mikrotrdoto, kot tudi najvišje standardne odklone med vzorci in posledično nestabilno proizvodnjo. Termoformiran Biocryl C izkazuje v primerjavi s toplotno neobdelanim materialom višjo natezno in upogibno trdnost ter nižjo žilavost. Na drugi strani v primerjavi z vroče strjevanim materialom (Triplex Hot) termično obdelan (termoformiranje) Biocryl C izkazuje višje vrednosti upogibne trdnosti in mikrotrdote ob sočasno nižjih vrednostih žilavosti in natezne trdnosti. Po drugi strani so bili pri vseh meritvah termoformiranega materiala Biocryl C zabeležene najnižje vrednosti statističnih raztrosov merjenih podatkov.

Rezultati opravljenih analiz kažejo, da je tehnologija termoformiranja termično obdelanih materialov po mehanskih lastnostih popolnoma primerljiva s hladno in toplo polimeriziranim PMMA materialom iz konvencionalnega postopka litja osnov zobnih protez. Bistveno izboljšanje pa kažejo rezultati termoformiranih preizkušancev napram klasični tehnologiji izdelave zobnih protez pri raztrosu izmerjenih podatkov (standardni odkloni), kar lahko zagotavlja višjo stabilnost proizvodnje dentalnih izdelkov iz PMMA s postopki termoformiranja. **Ključne besede:** polymethylmethacrylate zobna smola, termoformiranje, mehanske lastnosti, dentalne proteze, natezna trdnost, mikrotrdota, stabilnost proizvodnje

Doktorska disertacija, diplomske naloge

DOKTORSKE DISERTACIJE

Na Fakulteti za strojništvo Univerze v Mariboru je obranil svojo doktorsko disertacijo:

• dne 22. januarja 2015 **Marko HRELJA** z naslovom: »Modeliranje in optimizacija CNC obdelav s skupinsko inteligenco« (mentor: prof. dr. Miran Brežočnik);

Izboljševanje obstoječe proizvodnje in obdelovalnih sistemov zahteva nenehno posodabljanje in integracijo najnovejših tehnologij v proizvodne sisteme. Proizvodnih spremenljivk je čedalje več, s tem pa se povečuje množica podatkov, ki jo moramo obdelati, tu pa velikokrat klasične analitične metode optimizacije odpovedo. Zaradi tega smo prisiljeni bolje izkoristiti razpoložljive proizvodne vire, zato pa moramo poseči po naprednejših pristopih reševanja problemov. Za reševanje zahtevnih problemov čedalje pogosteje uporabljajo različna področja umetne inteligence, še zlasti strojnega učenja. Pregled do sedaj opravljenih raziskav je pokazal, da so obstoječi razviti sistemi precej ozko usmerjeni.

V disertaciji predlagamo popolnoma nov pristop k modeliranju CNC-obdelav s pomočjo novega gravitacijskega iskalnega algoritma (GSA), ki spada med metode skupinske inteligence. Razviti inteligentni sistem deluje na osnovi osnovnih Newtonovih fizikalnih zakonov oziroma na osnovi interakcij med masnimi telesi v prostoru. Za primerjavo in potrditev ustreznosti rezultatov doktorske disertacije smo uporabili tudi metodo modeliranja z rojem delcev (PSO). Primerjava je pokazala, da je GSA algoritem primeren za modeliranje obdelav z odrezovanjem, saj so odstopanja od eksperimentalnih podatkov v sprejemljivih mejah. Dobljeni modeli so dobro opisali postopek odrezovanja materiala s struženjem, ki smo ga uporabili kot postopek odrezovanja. Posebej velja omeniti, da je GSA algoritem v najslabšem primeru vsaj dvakrat hitrejši od enakovrednega PSO algoritma. Dobljen model CNC-obdelave smo nato uporabili za večkriterijsko optimiranje obdelovalnih parametrov: optimalne hrapavosti obdelane površine, rezalnih sil in časovne obstojnosti orodja. Vsaka izmed omenjenih odvisnih spremenljivk prispeva k optimalnemu delovanju CNC-obdelovalnega stroja, kar znižuje stroške proizvodnje. Večkriterijsko optimiranje smo izvedli s pomočjo NSGA-II algoritma. Za optimiranje smo morali določiti tudi omejitve. Te smo določili s pomočjo teoretičnih izračunov in jih preverili s pomočjo eksperimentalnih podatkov. Zaradi obsega dela smo se omejili na struženje, hkrati pa so v delu

predstavljene osnove prilagoditev za uporabo metod na ostalih obdelovalnih strojih, saj je predlagan pristop univerzalen.

DIPLOMSKE NALOGE

Na Fakulteti za strojništvo Univerze v Ljubljani sta pridobila naziv univerzitetni diplomirani inženir strojništva:

dne 30. januarja 2015:

Martin NAPOTNIK z naslovom: »Energetska sanacija proizvodnje stiroporne embalaže« (mentor: prof. dr. Alojz Poredoš);

Danijel POLJŠAK z naslovom: »Razvoj naprave za strojno vezanje armaturnih palic« (mentor: izr. prof. dr. Jernej Klemenc).

*

Na Fakulteti za strojništvo Univerze v Mariboru je pridobil naziv univerzitetni diplomirani inženir strojništva:

dne 29. januarja 2015:

Slavko PANDŽA z naslovom: »Analiza merilne negotovosti pri nateznem preskusu kovin« (mentor: prof. dr. Bojan Ačko).

*

Na Fakulteti za strojništvo Univerze v Ljubljani so pridobili naziv magister inženir strojništva:

dne 29. januarja 2015:

Tine LAZAR z naslovom: »Razvoj preizkuševališča za tlačno testiranje spojke iz kompozitnih materialov« (mentor: izr. prof. dr. Jože Tavčar, somentor: prof. dr. Jožef Duhovnik);

Davor RAŠIĆ z naslovom: »Razvoj metodologije za obdelavo izmerjenega poteka tlaka v valju dizelskega motorja z notranjim zgorevanjem« (mentor: izr. prof. dr. Tomaž Katrašnik);

Simon FINK z naslovom: »Laserska poslikava nakita« (mentor: doc. dr. Matija Jezeršek);

Nejc KORAČIN z naslovom: »Analiza parametrov razprševanja pri procesu oblaganja tablet« (mentor: prof. dr. Iztok Golobič, somentor: prof. dr. Franc Vrečer);

David MARKOVIČ z naslovom: »Modeliranje in simulacija hitro preklopnih elektromagnetnih ventilov v adaptivnih avtomobilskih blažilnikih« (mentor: prof. dr. Peter Butala, somentor: prof. dr. Jörg Wallaschek);

Gregor PISK z naslovom: »Načrtovanje in optimizacija montažne linije in u-celice« (mentor: izr. prof. dr. Janez Kušar, somentor: prof. dr. Marko Starbek);

dne 30. januarja 2015:

Rebeka SREBOTNIK z naslovom: »Uporaba neporušnih metod preizkušanja (metod NDT) za odkrivanje napak v lasersko izdelanih varih« (mentor: prof. dr. Janez Tušek, somentor: doc. dr. Andrej Lešnjak).

*

Na Fakulteti za strojništvo Univerze v Mariboru je pridobil naziv magister inženir mehatronike:

dne 28. januarja 2015:

Rok KOVŠE z naslovom: »Teleoperiranje kvadrokopterja Parrot AR. Drone s pomočjo haptične naprave Phantom Omni« (mentor: izr. prof. dr. Karl Gotlih, somentor: izr. prof. dr. Aleš Hace).

*

Na Fakulteti za strojništvo Univerze v Mariboru je pridobil naziv diplomirani inženir strojništva (UN):

dne 29. januarja 2015:

Miha PLEVEL z naslovom: »Načrtovanje proizvodnega procesa izdelave pralnega aparata za javno uporabo« (mentor: doc. dr. Marjan Leber, somentor: doc. dr. Iztok Palčič).

*

Na Fakulteti za strojništvo Univerze v Ljubljani so pridobila naziv diplomirani inženir strojništva:

dne 16. januarja 2015:

Martin HAUPTMAN z naslovom: »Koncept šolskega jadralnega letala« (mentor: izr. prof. dr. Tadej Kosel);

Matjaž LAGOJA z naslovom: »Analiza prečnega odmikanja in vpliva dinamične komponente na dobo

trajanja zobatega jermena« (mentor: prof. dr. Marko Nagode);

dne 19. januarja 2015:

Robert ČOPI z naslovom: »Postavitev tehnologije brizganja izdelka iz duroplasta« (mentor: izr. prof. dr. Joško Valentinčič, somentor: doc. dr. Andrej Lebar);

Norbert ŠABANI z naslovom: »Obzidava kotlov in industrijskih peči« (mentor: izr. prof. dr. Andrej Senegačnik).

*

Na Fakulteti za strojništvo Univerze v Mariboru sta pridobila naziv diplomirani inženir strojništva:

dne 29. januarja 2015:

Iztok ORAČ z naslovom: »Konstruiranje kovične priprave ročaja pri montaži« (mentor: prof. dr. Iztok Potrč);

Mitja ŽAGAR z naslovom: »Konstruiranje teleskopskega tračnega transporterja« (mentor: izr. prof. dr. Tone Lerher, somentor: prof. dr. Iztok Potrč).

*

Na Fakulteti za strojništvo Univerze v Ljubljani so pridobili naziv diplomirani inženir strojništva (VS):

dne 16. januarja 2015:

Alan JEREB z naslovom: »Motorizirano vodilo za kamere in fotoaparate« (mentor: doc. dr. Boris Jerman);

dne 19. januarja 2015:

Nejc DRAKSLER z naslovom: »Analiza tehnologij solarnega hlajenja« (mentor: izr. prof. dr. Andrej Kitanovski, somentor: prof. dr. Alojz Poredoš);

Leon NARAD z naslovom: »Optimizacija toka izdelave komponente pomivalnega stroja« (mentor: izr. prof. dr. Janez Kušar, somentor: prof. dr. Marko Starbek);

Andraž ŠTANTE z naslovom: »Poenotenje nacionalnih standardov licenciranja letalskega osebja v univerzalno mednarodne standarde« (mentor: doc. dr. Patrick Vlačič, somentor: izr. prof. dr. Tadej Kosel).

Information for Authors

All manuscripts must be in English. Pages should be numbered sequentially. The manuscript should be composed in accordance with the Article Template given above. The maximum length of contributions is 10 pages. Longer contributions will only be accepted if authors provide justification in a cover letter. For full instructions see the Information for Authors section on the journal's website: <http://cn.sv-jme.eu>.

SUBMISSION:

Submission to SV-JME is made with the implicit understanding that neither the manuscript nor the essence of its content has been published previously either in whole or in part and that it is not being considered for publication elsewhere. All the listed authors should have agreed on the content and the corresponding (submitting) author is responsible for having ensured that this agreement has been reached. The acceptance of an article is based entirely on its scientific merit, as judged by peer review. Scientific articles comprising simulations only will not be accepted for publication; simulations must be accompanied by experimental results carried out to confirm or deny the accuracy of the simulation. Every manuscript submitted to the SV-JME undergoes a peer-review process.

The authors are kindly invited to submit the paper through our web site: <http://ojs.sv-jme.eu>. The Author is able to track the submission through the editorial process - as well as participate in the copyediting and proofreading of submissions accepted for publication - by logging in, and using the username and password provided.

SUBMISSION CONTENT:

The typical submission material consists of:

- A **manuscript** (A PDF file, with title, all authors with affiliations, abstract, keywords, highlights, inserted figures and tables and references),
- Supplementary files:
 - a **manuscript** in a WORD file format
 - a **cover letter** (please see instructions for composing the cover letter)
 - a ZIP file containing **figures** in high resolution in one of the graphical formats (please see instructions for preparing the figure files)
 - possible **appendices** (optional), cover materials, video materials, etc.

Incomplete or improperly prepared submissions will be rejected with explanatory comments provided. In this case we will kindly ask the authors to carefully read the Information for Authors and to resubmit their manuscripts taking into consideration our comments.

COVER LETTER INSTRUCTIONS:

Please add a **cover letter** stating the following information about the submitted paper:

1. **Paper title**, list of **authors** and their **affiliations**.
2. **Type of paper**: original scientific paper (1.01), review scientific paper (1.02) or short scientific paper (1.03).
3. A **declaration** that neither the manuscript nor the essence of its content has been published in whole or in part previously and that it is not being considered for publication elsewhere.
4. State the **value of the paper** or its practical, theoretical and scientific implications. What is new in the paper with respect to the state-of-the-art in the published papers? Do not repeat the content of your abstract for this purpose.
5. We kindly ask you to suggest at least two **reviewers** for your paper and give us their names, their full affiliation and contact information, and their scientific research interest. The suggested reviewers should have at least two relevant references (with an impact factor) to the scientific field concerned; they should not be from the same country as the authors and should have no close connection with the authors.

FORMAT OF THE MANUSCRIPT:

The manuscript should be composed in accordance with the Article Template. The manuscript should be written in the following format:

- A **Title** that adequately describes the content of the manuscript.
- A list of **Authors** and their **affiliations**.
- An **Abstract** that should not exceed 250 words. The Abstract should state the principal objectives and the scope of the investigation, as well as the methodology employed. It should summarize the results and state the principal conclusions.
- 4 to 6 significant **key words** should follow the abstract to aid indexing.
- 4 to 6 **highlights**: a short collection of bullet points that convey the core findings and provide readers with a quick textual overview of the article. These four to six bullet points should describe the essence of the research (e.g. results or conclusions) and highlight what is distinctive about it.
- An **Introduction** that should provide a review of recent literature and sufficient background information to allow the results of the article to be understood and evaluated.
- A **Methods** section detailing the theoretical or experimental methods used.
- An **Experimental section** that should provide details of the experimental set-up and the methods used to obtain the results.
- A **Results** section that should clearly and concisely present the data, using figures and tables where appropriate.
- A **Discussion** section that should describe the relationships and generalizations shown by the results and discuss the significance of the results, making comparisons with previously published work. (It may be appropriate to combine the Results and Discussion sections into a single section to improve clarity.)
- A **Conclusions** section that should present one or more conclusions drawn from the results and subsequent discussion and should not duplicate the Abstract.
- **Acknowledgement** (optional) of collaboration or preparation assistance may be included. Please note the source of funding for the research.
- **Nomenclature** (optional). Papers with many symbols should have a nomenclature that defines all symbols with units, inserted above the references. If one is used, it must contain all the symbols used in the manuscript and the definitions should not be repeated in the text. In all cases, identify the symbols used if they are not widely recognized in the profession. Define acronyms in the text, not in the nomenclature.
- **References** must be cited consecutively in the text using square brackets [1] and collected together in a reference list at the end of the manuscript.
- **Appendix(-ices)** if any.

SPECIAL NOTES

Units: The SI system of units for nomenclature, symbols and abbreviations should be followed closely. Symbols for physical quantities in the text should be written in italics (e.g. v , T , n , etc.). Symbols for units that consist of letters should be in plain text (e.g. ms^{-1} , K , min , mm , etc.). Please also see: <http://physics.nist.gov/cuu/pdf/sp811.pdf>.

Abbreviations should be spelt out in full on first appearance followed by the abbreviation in parentheses, e.g. variable time geometry (VTG). The meaning of symbols and units belonging to symbols should be explained in each case or cited in a **nomenclature** section at the end of the manuscript before the References.

Figures (figures, graphs, illustrations digital images, photographs) must be cited in consecutive numerical order in the text and referred to in both the text and the captions as Fig. 1, Fig. 2, etc. Figures should be prepared without borders and on white grounding and should be sent separately in their original formats. If a figure is composed of several parts, please mark each part with a), b), c), etc. and provide an explanation for each part in Figure caption. The caption should be self-explanatory. Letters and numbers should be readable (Arial or Times New Roman, min 6 pt with equal sizes and fonts in all figures). Graphics (submitted as supplementary files) may be exported in resolution good enough for printing (min. 300 dpi) in any common format, e.g. TIFF, BMP or JPG, PDF and should be named Fig1.jpg, Fig2.tif, etc. However, graphs and line drawings should be prepared as vector images, e.g. CDR, AI. Multi-curve graphs should have individual curves marked with a symbol or otherwise provide distinguishing differences using, for example, different thicknesses or dashing.

Tables should carry separate titles and must be numbered in consecutive numerical order in the text and referred to in both the text and the captions as Table 1, Table 2, etc. In addition to the physical quantities, such as t (in italics), the units [s] (normal text) should be added in square brackets. Tables should not duplicate data found elsewhere in the manuscript. Tables should be prepared using a table editor and not inserted as a graphic.

REFERENCES:

A reference list must be included using the following information as a guide. Only cited text references are to be included. Each reference is to be referred to in the text by a number enclosed in a square bracket (i.e. [3] or [2] to [4] for more references; do not combine more than 3 references, explain each). No reference to the author is necessary.

References must be numbered and ordered according to where they are first mentioned in the paper, not alphabetically. All references must be complete and accurate. Please add DOI code when available. Examples follow.

Journal Papers:

Surname 1, Initials, Surname 2, Initials (year). Title. Journal, volume, number, pages, DOI code.

- [1] Hackenschmidt, R., Alber-Laukant, B., Rieg, F. (2010). Simulating nonlinear materials under centrifugal forces by using intelligent cross-linked simulations. *Strojniški vestnik - Journal of Mechanical Engineering*, vol. 57, no. 7-8, p. 531-538, DOI:10.5545/sv-jme.2011.013.

Journal titles should not be abbreviated. Note that journal title is set in italics.

Books:

Surname 1, Initials, Surname 2, Initials (year). Title. Publisher, place of publication.

- [2] Groover, M.P. (2007). *Fundamentals of Modern Manufacturing*. John Wiley & Sons, Hoboken.

Note that the title of the book is italicized.

Chapters in Books:

Surname 1, Initials, Surname 2, Initials (year). Chapter title. Editor(s) of book, book title. Publisher, place of publication, pages.

- [3] Carbone, G., Ceccarelli, M. (2005). Legged robotic systems. Kordić, V., Lazinica, A., Merdan, M. (Eds.), *Cutting Edge Robotics*. Pro literatur Verlag, Mammendorf, p. 553-576.

Proceedings Papers:

Surname 1, Initials, Surname 2, Initials (year). Paper title. Proceedings title, pages.

- [4] Štefanič, N., Martinčević-Mikić, S., Tošanović, N. (2009). Applied lean system in process industry. *MOTSP Conference Proceedings*, p. 422-427.

Standards:

Standard-Code (year). Title. Organisation. Place.

- [5] ISO/DIS 16000-6.2:2002. *Indoor Air – Part 6: Determination of Volatile Organic Compounds in Indoor and Chamber Air by Active Sampling on TENAX TA Sorbent, Thermal Desorption and Gas Chromatography using MSD/FID*. International Organization for Standardization. Geneva.

WWW pages:

Surname, Initials or Company name. Title, from <http://address>, date of access.

- [6] Rockwell Automation. Arena, from <http://www.arenasimulation.com>, accessed on 2009-09-07.

EXTENDED ABSTRACT:

When the paper is accepted for publishing, the authors will be requested to send an **extended abstract** (approx. one A4 page or 3500 to 4000 characters). The instruction for composing the extended abstract are published on-line: <http://www.sv-jme.eu/information-for-authors/>.

COPYRIGHT:

Authors submitting a manuscript do so on the understanding that the work has not been published before, is not being considered for publication elsewhere and has been read and approved by all authors. The submission of the manuscript by the authors means that the authors automatically agree to transfer copyright to SV-JME when the manuscript is accepted for publication. All accepted manuscripts must be accompanied by a Copyright Transfer Agreement, which should be sent to the editor. The work should be original work by the authors and not be published elsewhere in any language without the written consent of the publisher. The proof will be sent to the author showing the final layout of the article. Proof correction must be minimal and executed quickly. Thus it is essential that manuscripts are accurate when submitted. Authors can track the status of their accepted articles on <http://cn.sv-jme.eu>.

PUBLICATION FEE:

Authors will be asked to pay a publication fee for each article prior to the article appearing in the journal. However, this fee only needs to be paid after the article has been accepted for publishing. The fee is 240.00 EUR (for articles with maximum of 6 pages), 300.00 EUR (for articles with maximum of 10 pages), plus 30.00 EUR for each additional page. The additional cost for a color page is 90.00 EUR. These fees do not include tax.

Strojniški vestnik - Journal of Mechanical Engineering
Aškerčeva 6, 1000 Ljubljana, Slovenia,
e-mail: info@sv-jme.eu



<http://www.sv-jme.eu>

Contents

Papers

- 91 Karol Franciszek Abramek – Tomasz Stoeck – Tomasz Osipowicz:
Statistical Evaluation of the Corrosive Wear of Fuel Injector Elements Used in Common Rail Systems
- 99 Liao Yunfei, Zhou Yi, Liu Youhai, Zuo Dong, Tan Bo:
Study of Stability of Precise Tiled-grating Device
- 107 Diego E. Lozano, Gabriela Martinez-Cazares, Rafael D. Mercado-Solis, Rafael Colás, George E. Totten:
Estimation of Transient Temperature Distribution during Quenching, via a Parabolic Model
- 115 Yi Jiangang:
Modelling and Analysis of Step Response Test for Hydraulic Automatic Gauge Control
- 123 Serkan Balli, Faruk Sen:
Failure Prediction of Cross-Ply Laminated Double-Serial Mechanically Fastened Composites using Fuzzy Expert System
- 131 Xiaoming Huang, Jie Sun, Jianfeng Li:
Effect of Initial Residual Stress and Machining-Induced Residual Stress on the Deformation of Aluminium Alloy Plate
- 138 Sebastian Baloš, Mladomir Milutinović, Michal Potran, Jelena Vuletić, Tatjana Puškar, Tomaž Pepelnjak:
The Mechanical Properties of Moulded and Thermoformed Denture Resins